



# Inner-Scaled Helmholtz-Resonators for Turbulent Boundary Layer Flow Control

**MSc Thesis**

Renko Siebols



# Inner-Scaled Helmholtz-Resonators for Turbulent Boundary Layer Flow Control

by

Renko Siebols

to obtain the degree of Master of Science  
at the Delft University of Technology,  
to be defended publicly on June 10, 2022.

Student Number: 4464389  
Project Duration: October 2021 - June 2022

## **Thesis committee**

Chair: Dr. ir. B. W. van Oudheusden

Committee Members: Dr. ir. W. J. Baars (Supervisor)  
Ir. M. Pini (examiner)

An electronic version of this thesis is available at <http://repository.tudelft.nl>



# Abstract

An experimental study is presented towards inner-scaled Helmholtz-Resonators (HRs) as a passive turbulent boundary layer (TBL) flow control method. Using acoustic pressure-velocity coupling at the orifice of the HR, it is aimed to attenuate the kinetic energy of the grazing turbulence to reduce the mean skin friction. The HRs are tuned towards the spatial and temporal scales of the near-wall cycle turbulence events that play a major role in the production of turbulence. The adopted HR design strategy has a spatial tuning towards the most efficient attenuation of sweep events, based on recent studies on micro-cavity arrays (Silvestri et al., 2017a). The temporal tuning is based on the streamwise wavelength of the most energetic wall-normal velocity fluctuations. These interact with the wall to create pressure fluctuations which form the primary excitation source of the HRs.

A parameter study on HRs under a fully developed grazing TBL at  $Re_\tau \approx 2200$  was performed. A strong pressure-velocity coupling was found between the HR cavity pressure and the streamwise velocity fluctuations of the grazing TBL when the HR design frequency either matched the frequency of the most energetic wall-normal velocity fluctuations or when the HR design frequency was below this frequency. The pressure-velocity coupling extends to  $y^+ \approx 25$ , in which phase-interlocking of the grazing TBL occurs. Clear inflow and outflow regions were identified with a streamwise width related to the HR resonance frequency. The inflow and outflow regions cause an increase and decrease in streamwise velocity respectively. These velocity fluctuations appear as an increase in spectral energy around the wavelengths of the HR resonance and are accompanied by a reduction in spectral energy at higher wavelengths. While quadrant analysis indicates an increase in turbulence production from an increased relative strength of Q2 and Q4 events, variable-interval time averaging indicates no significant changes to the intensity and duration of the near-wall cycle turbulence events as a result of the HR resonance. To date, no significant changes to the mean boundary layer statistics were found that could directly be attributed to the achieved pressure-velocity coupling. Note that only a single HR has been the focus of the current study, with valuable information about HR scaling, resonance and domain-of influence on the TBL flow. Future arrays of HRs may be able to show a more pronounced global effect on the mean flow.



# Preface

This thesis marks the end of seven years of studying at the Faculty of Aerospace Engineering at TU Delft. I have got my Bachelor's degree here and this thesis is the last step towards getting my Master's degree. Besides studying, I have had plenty of opportunities to develop myself further and get to know the industry.

I would like to thank dr. ir. Woutijn Baars for the chance to take up this project, and for the continuous guidance and feedback over the past few months. I would also like to thank ir. Giulio Dacome for his feedback and for the help with setting up the experiments. All the help and feedback definitely contributed to improving the end result of this thesis.

Finally, I would like to thank everyone who supported me along the way. I know I can sometimes make things harder for myself than they need to be, and it is good to be reminded of that every once in a while. At least, with this thesis coming to an end, there is one thing less to worry about.

*Renko Siebols  
Delft, May 2022*



# Contents

<b>Abstract</b>	<b>i</b>
<b>Preface</b>	<b>iii</b>
<b>List of Figures</b>	<b>viii</b>
<b>List of Tables</b>	<b>xii</b>
<b>Nomenclature</b>	<b>xiii</b>
<b>1 Introduction</b>	<b>1</b>
<b>2 Fundamentals of Turbulent Boundary Layers</b>	<b>3</b>
2.1 Boundary Layer on a Full-Size Aircraft . . . . .	3
2.2 Turbulent Boundary Layer Parameters . . . . .	3
2.3 Scaling in a Turbulent Boundary Layer . . . . .	5
2.4 Turbulence Intensity and Turbulence Kinetic Energy . . . . .	6
2.5 Instantaneous Flow Structures within a Turbulent Boundary Layer . . . . .	7
2.5.1 Flow Structures and Events in the Inner Regions . . . . .	7
2.5.2 Flow Structures and Events in the Outer Regions . . . . .	9
2.6 Statistical Analysis of the Turbulent Boundary Layer . . . . .	9
2.6.1 Quadrant Analysis . . . . .	10
2.6.2 Spectral Analysis . . . . .	10
2.7 Reynolds Number Effects . . . . .	12
2.8 Concluding Remarks on Skin Friction . . . . .	13
<b>3 Passive Flow Control for Skin Friction Reduction</b>	<b>15</b>
3.1 Control Strategies for Skin Friction Reduction . . . . .	15
3.2 Large-Scale Boundary Layer Flow Control . . . . .	15
3.3 Small-Scale Boundary Layer Flow Control . . . . .	16
3.4 Micro-Cavity Array for Small Scale Boundary Layer Flow Control . . . . .	16
3.5 Potential for Aero-Acoustic Coupling for Boundary Layer Control . . . . .	18
<b>4 Helmholtz-Resonators</b>	<b>19</b>
4.1 Introduction of a Single Helmholtz-Resonator . . . . .	19
4.1.1 Acoustic Resonance Frequency . . . . .	19
4.1.2 Phase and Gain Modulation . . . . .	21
4.1.3 Overtones . . . . .	22
4.2 System of Two Adjacent Helmholtz-Resonators . . . . .	23
4.3 Excitation of a Helmholtz-Resonator . . . . .	24
4.3.1 Shear Layer Separation . . . . .	25
4.3.2 Turbulent Boundary Layer Wall-Pressure Fluctuations . . . . .	27
4.4 Spatial and Temporal Tuning of Helmholtz-Resonators . . . . .	27
4.4.1 Strategy 1: Spatial and Temporal Tuning towards Most Energetic $u$ -Fluctuations . . . . .	27
4.4.2 Strategy 2: Spatial Tuning towards Attenuating Sweep Events, Temporal Tuning towards Most Energetic $u$ -Fluctuations . . . . .	28
4.4.3 Strategy 3: Spatial Tuning towards Attenuating Sweep Events, Temporal Tuning towards Most Energetic $v$ -/Pressure Fluctuations . . . . .	28
4.4.4 Design Considerations for Arrays of Helmholtz-Resonators . . . . .	29
4.5 Assessment and Characterisation of Existing Studies towards Helmholtz-Resonators under a Grazing Turbulent Boundary Layer . . . . .	29
4.6 Knowledge Gap in Research towards Helmholtz-Resonators under Turbulent Boundary Layer . . . . .	31

4.7	Full-Scale Applicability of Proposed Tuning Strategies . . . . .	32
<b>5</b>	<b>Experimental Setup and Methodology</b>	<b>33</b>
5.1	Wind Tunnel Setup . . . . .	33
5.2	Experimental Design . . . . .	34
5.2.1	Chosen Design Strategy . . . . .	35
5.2.2	Design Parameters for Helmholtz-Resonators . . . . .	35
5.3	Measurement Techniques . . . . .	38
5.3.1	Microphones for Acoustic and Wall-Pressure Analysis . . . . .	39
5.3.2	PIV Measurements . . . . .	40
5.3.3	Hot-Wire Anemometry . . . . .	41
<b>6</b>	<b>Data Processing</b>	<b>44</b>
6.1	Microphone Measurements . . . . .	44
6.1.1	Spectral Analysis . . . . .	44
6.1.2	Noise Correction using Linear Spectral Stochastic Estimation . . . . .	45
6.1.3	Use of Transfer Function to Determine HR Resonance Frequency . . . . .	48
6.2	PIV Measurements . . . . .	50
6.2.1	Image Pre-Processing . . . . .	50
6.2.2	Image Processing . . . . .	51
6.2.3	PIV Wall-Finding Procedure . . . . .	52
6.2.4	Phase-Averaging . . . . .	53
6.2.5	Mean Boundary Layer Profiles . . . . .	55
6.2.6	Quadrant Analysis . . . . .	55
6.3	Hot-Wire Measurements . . . . .	55
6.3.1	Correction of Wall-Position . . . . .	55
6.3.2	Spectral Analysis . . . . .	57
6.3.3	VITA Analysis . . . . .	57
6.3.4	Phase-Averaging . . . . .	58
<b>7</b>	<b>Results: Microphone Measurements</b>	<b>60</b>
7.1	Acoustic Characterisation of Helmholtz-Resonators . . . . .	60
7.2	Turbulent Boundary Layer Excitation . . . . .	62
7.2.1	Measured Wall-Pressure Spectrum with Pinhole Microphones . . . . .	62
7.2.2	Excitation of Single Helmholtz-Resonators . . . . .	63
7.2.3	Remarks on Downstream Wall-Pressure Measurements . . . . .	64
7.2.4	Remarks on the HR Array Measurements . . . . .	65
<b>8</b>	<b>Results: Flow Measurements</b>	<b>67</b>
8.1	Linear Coherence Spectra . . . . .	67
8.2	Spectral Analysis . . . . .	68
8.3	Phase-Averaged Measurements . . . . .	70
8.3.1	Phase-Averaged Hot-Wire Measurements . . . . .	70
8.3.2	Phase-Averaged PIV Measurements . . . . .	71
8.4	Quadrant Analysis . . . . .	74
8.5	VITA Analysis . . . . .	75
8.6	Mean Boundary Layer Statistics . . . . .	77
<b>9</b>	<b>Discussion</b>	<b>79</b>
9.1	Excitation of Helmholtz-Resonators . . . . .	79
9.2	Pressure-Velocity Coupling with Helmholtz-Resonators . . . . .	80
9.3	Mean and Instantaneous Effects . . . . .	81
9.4	Effect on Near Wall-Cycle Events . . . . .	81
9.5	Potential Uses for Helmholtz-Resonators as Flow Control Method . . . . .	81
9.6	Remarks on Research Questions . . . . .	82
<b>10</b>	<b>Conclusions</b>	<b>83</b>
<b>11</b>	<b>Recommendations for Future Research</b>	<b>85</b>
11.1	More Isolated Parameter Study . . . . .	85

---

11.2 Helmholtz-Resonator Array Design . . . . .	85
11.3 Improvements for Noise Measurements . . . . .	86
11.4 Improvements for Flow Measurements . . . . .	86
11.5 Further Research towards Other Design Strategies . . . . .	86
<b>A Assembly Overview</b>	<b>92</b>

# List of Figures

1.1	Breakdown of a) direct operating costs and b) drag for a typical long-range aircraft. After Marec (2001) . . . . .	1
2.1	Visualisation of a boundary layer with a typical coordinate system. Illustration after Seyyedi et al. (2019) . . . . .	4
2.2	Inner-scaled mean velocity profile of a TBL at various $Re_\tau$ . From Perlin et al. (2016) . .	5
2.3	Outer-scaled mean velocity profile of a TBL at various $Re_\tau$ . From Perlin et al. (2016) . .	6
2.4	Turbulence kinetic energy budget in the inner region of the turbulent boundary layer. From Pope (2000) based on DNS data from Spalart (1988) . . . . .	8
2.5	Visualisation of the near-wall cycle. From Hinze (1975) . . . . .	8
2.6	Quadrant $uv$ -decomposition. After Pope (2000) . . . . .	10
2.7	Measurements of inner-scaled convection velocity $U_c^+$ in a turbulent boundary layer. Dotted line denotes mean boundary layer velocity $\bar{u}^+$ . From Liu and Gayme (2020) . . . . .	11
2.8	Iso-contour plot of a streamwise velocity fluctuation pre-multiplied energy spectrum. Both inner and outer scaling are shown. From Mathis et al. (2009) . . . . .	12
2.9	Pre-multiplied energy spectra at various $Re_\tau$ from 2800 to 650,000. Modified from Mathis et al. (2009) . . . . .	13
3.1	Micro-cavity array with different types of backing cavities. Modified from Silvestri et al. (2018) . . . . .	17
4.1	Schematic of a cylindrical Helmholtz-Resonator with typical design parameters . . . . .	19
4.2	Helmholtz-Resonator represented as a mass-spring-damper system . . . . .	20
4.3	Typical pinhole microphone arrangement, relating measured pressure $p_p(t)$ to input pressure $p_i(t)$ through impulse response $g(t)$ . . . . .	21
4.4	Amplitude and phase response of a pin-hole Helmholtz-Resonator with design frequency $f_0 = 2340Hz$ . From Gibeau and Ghaemi (2021) . . . . .	22
4.5	Helmholtz-Resonator with two plane waves for determining acoustic impedance . . . . .	23
4.6	A system of two Helmholtz-Resonators. After Urzyncok (2003) . . . . .	23
4.7	Excitation methods of a Helmholtz-Resonator with potential effects. Modified from Stein (2018) . . . . .	25
4.8	Shear layer separation over a Helmholtz-Resonator. After Ghanadi (2014) . . . . .	25
4.9	Effect of a single Helmholtz-Resonator on the mean boundary layer profile, obtained from LDA measurements $18.65\text{ mm}$ ( $\approx 1.35\delta$ ) downstream of the HR leading edge. From Urzyncok (2003) . . . . .	26
4.10	Effect of a single Helmholtz-Resonator on turbulence intensities, obtained from LDA measurements $18.65\text{ mm}$ ( $\approx 1.35\delta$ ) downstream of the HR leading edge. From Urzyncok (2003) . . . . .	26
4.11	Pre-multiplied 1D energy spectra of (a) $u$ -fluctuations, (b) $v$ -fluctuations and (c) pressure fluctuations. Increased colour intensity contours indicate increasing Reynolds number. After Lee and Moser (2015) and Panton et al. (2017) . . . . .	27
4.12	Tuning Strategy 1, with $d_0^+ = 500$ and $\lambda_x^+ = 1000$ . . . . .	28
4.13	Tuning Strategy 2, with $d_0^+ = 60$ and $\lambda_x^+ = 1000$ . . . . .	28
4.14	Tuning Strategy 3, with $d_0^+ = 600$ and $\lambda_x^+ = 250$ . . . . .	29
5.1	Test sections of the wind tunnel setup. From Baars (2021) . . . . .	33
5.2	Schematic top view of the test setup . . . . .	34
5.3	Schematic side view of the test setup. Dimensions not to scale for illustrative purposes	34
5.4	Top views of a) single HR setup and b) HR array setup . . . . .	35

5.5	Side view of a row of 7 HRs for $d^+ = 72$ at nominal resonance . . . . .	37
5.6	HR array assembly . . . . .	38
5.7	Schematic of microphone anemometry arrangement for measuring acoustic pressure response of HR with pin-hole microphone setup. Dimensions not to scale for illustrative purposes. . . . .	39
5.8	Pinhole microphone design . . . . .	39
5.9	Freestream microphone and pitot tube setup . . . . .	40
5.10	PIV field of view arrangements . . . . .	41
5.11	Hot-wire arrangement for boundary layer measurements. Not to scale . . . . .	42
5.12	Schematics of the applied wall-positioning procedures for the hot-wire probe . . . . .	42
6.1	Schematic of microphone anemometry arrangement for the single HR setup with indication of measured time signals of pressure fluctuations $p(t)$ . . . . .	44
6.2	Non-corrected energy spectra calculated from the microphone measurements with $N = 2^{12}$ for the single HR setup with $d^+ = 108$ , subresonance . . . . .	45
6.3	Non-corrected energy spectra with 5% BMF calculated from the microphone measurements with $N = 2^{12}$ for the single HR setup with $d^+ = 108$ , subresonance . . . . .	46
6.4	LCS between the HR microphone signal and the noise microphone signal with $N = 2^{12}$ for the single HR setup with $d^+ = 108$ , subresonance. On the right the acoustic pressure spectra of both signals are plotted for reference . . . . .	46
6.5	Noise-corrected energy spectra calculated from the microphone measurements with $N = 2^{12}$ for the single HR setup with $d^+ = 108$ , subresonance . . . . .	47
6.6	Experimentally obtained transfer function $H$ from direct reference measurement, with the second-order model fitted transfer function $G$ . Measurements from acoustic characterisation for the single HR setup with $d^+ = 3 \text{ mm}$ , subresonance . . . . .	48
6.7	Experimentally obtained transfer function $H$ from direct reference measurement, with the second-order model fitted transfer function $G$ . Measurements from acoustic characterisation for the pinhole microphone. . . . .	49
6.8	Experimentally obtained transfer function $H$ via pinhole measurement, with the second-order model fitted transfer function $G$ . Measurements from wind tunnel test for the single HR setup with $d^+ = 3 \text{ mm}$ , subresonance. Phase modulation implied from model as no experimental data is obtained with the used method . . . . .	50
6.9	Workflow for processing of PIV images . . . . .	50
6.10	Comparison between raw PIV images and the pre-processed PIV images . . . . .	51
6.11	Mean velocity from the cross-correlation processing for the single HR with $d_0^+ = 108$ , nominal resonance. Black line indicates the location of the HR orifice . . . . .	52
6.12	Mean velocity field as obtained from the sum-of-correlations processing for the single HR with $d_0^+ = 108$ , nominal resonance. Black line indicates the location of the HR orifice . . . . .	52
6.13	PIV wall-finding procedure . . . . .	53
6.14	Results from the PIV wall-finding procedure with a polynomial fit for the single HR with $d_0^+ = 108$ , nominal resonance . . . . .	53
6.15	Visualisation of the signals used for the phase averaging of PIV images. . . . .	54
6.16	Results of the binning procedure for the phase-averaging of the PIV measurements for the single HR with $d_0^+ = 108$ , subresonance . . . . .	54
6.17	Schematic for the quadrant analysis as applied to the PIV instantaneous velocity fields . . . . .	55
6.18	Schematic of the hot-wire anemometry arrangement indicating the measured signals and measurement region . . . . .	56
6.19	Non-corrected hot-wire measurements for the single HR setup with $d^+ = 108$ , subresonance . . . . .	56
6.20	Two variations of the wall-correction procedure for the hot-wire measurements through least-squares fit with a reference DNS profile. . . . .	57
6.21	Visualisation of the detection procedure of VITA-events using detection function $D$ . . . . .	58
6.22	VITA analysis for sweep events for the single HR setup with $d_0^+ = 108$ , subresonance. Grey lines indicate individual detected events, with the average of all events indicated in green. . . . .	59

6.23	Visualisation of the used time signals for the phase-averaging of the hot-wire measurements . . . . .	59
7.1	Phase and gain of the measured transfer function $H_{HR}$ for the acoustic characterisation measurements of the tested HRs . . . . .	61
7.2	Transfer function gain as function of frequency. Dotted lines indicate the calculated frequencies of the overtones. Wind tunnel measurements for single HR setup for $d_0 = 3$ mm, subresonance . . . . .	62
7.3	Estimation of the wall-pressure spectrum from the pinhole microphone measurement. Reference wall-pressure spectrum from a DNS at $Re_\tau = 2000$ . . . . .	63
7.4	Phase and gain of the measured transfer function $H_{HR}$ for the wind tunnel measurements of the tested HRs . . . . .	64
7.5	Transfer function gain as function of frequency for. Dotted lines indicate the calculated frequencies of the overtones. Wind tunnel measurements for single HR setup for $d_0^+ = 108$ , subresonance . . . . .	64
7.6	Non-corrected energy spectra calculated from the microphone measurements with $N = 2^{12}$ for a streamwise line of 5 HRs of the HR array setup with $d^+ = 72$ , nominal resonance	65
7.7	Noise-corrected energy spectra calculated from the microphone measurements with $N = 2^{12}$ for a streamwise line of 5 HRs of the HR array setup with $d^+ = 72$ , nominal resonance . . . . .	65
7.8	Experimentally obtained transfer function $H$ via pinhole measurement, with the second-order model fitted transfer function $G$ . Measurements from wind tunnel test for the first HR in a streamwise line of 5 HRs of the HR array setup with $d^+ = 72$ , nominal resonance. Phase modulation implied from model as no experimental data is obtained with the used method . . . . .	66
8.1	Contour plots of the LCS between the HR cavity microphone signal and the hot-wire measurements. Note the different colour scales for each row of plots that are used because of the large difference in coherence for the different resonance cases. Dotted lines indicate respective HR resonance frequencies . . . . .	68
8.2	Energy spectra of streamwise velocity fluctuations from hot-wire measurements for the HRs with $d_0^+ = 108$ . . . . .	69
8.3	Energy spectra of streamwise velocity fluctuations from hot-wire measurements shown as difference with respect to the reference energy spectrum for HRs with $d_0^+ = 108$ . . . . .	69
8.4	Energy spectra of streamwise velocity fluctuations from hot-wire measurements shown as difference with respect to the reference energy spectrum for HRs with $d_0^+ = 72$ . . . . .	70
8.5	Phase-averaged streamwise velocity fluctuations for the HRs with $d_0^+ = 108$ . Black contour lines indicate zero streamwise velocity fluctuations . . . . .	71
8.6	Placement of the phase-averaging bins over one cycle of HR resonance . . . . .	71
8.7	Bin-average contour plots of velocity fluctuations for bin 4 out of 6 for the single HR setup at $d_0^+ = 108$ , subresonance. Black line indicates the location of the HR orifice . . . . .	72
8.8	Bin-average contour plots of velocity fluctuations for bin 5 out of 6 for the single HR setup at $d_0^+ = 108$ , subresonance. Black line indicates the location of the HR orifice . . . . .	72
8.9	Bin-average contour plots of velocity fluctuations for bin 6 out of 6 for the single HR setup at $d_0^+ = 108$ , subresonance. Black line indicates the location of the HR orifice . . . . .	72
8.10	Bin-average contour plots of velocity fluctuations for bin 4 out of 6 for the single HR setup at $d_0^+ = 108$ , subresonance. Black line indicates the location of the HR orifice. Dotted lines indicate streamwise length scale of resonance . . . . .	73
8.11	Bin-average contour plots of velocity fluctuations for bin 5 out of 6 for the single HR setup at $d_0^+ = 108$ , nominal resonance. Black line indicates the location of the HR orifice. Dotted lines indicate streamwise length scale of resonance . . . . .	73
8.12	Bin-average contour plots of velocity fluctuations for bin 5 out of 6 for the single HR setup at $d_0^+ = 108$ , superresonance. Black line indicates the location of the HR orifice. Dotted lines indicate streamwise length scale of resonance . . . . .	74
8.13	JPDF of velocity fluctuations from quadrant $uv$ -decomposition between $15 < y^+ < 35$ for the single HR setup with $d_0^+ = 108$ . . . . .	74

---

8.14 WJPDF of velocity fluctuations from quadrant $uv$ -decomposition between $15 < y^+ < 35$ for the single HR setup with $d_0^+ = 108$ . . . . .	75
8.15 VITA analysis for sweep events for the single HR setup with $d_0^+ = 72$ at $y^+ = 15$ . . . . .	76
8.16 VITA analysis for sweep events for the single HR setup with $d_0^+ = 108$ at $y^+ = 15$ . . . . .	76
8.17 Averaged VITA events for the single HR setup with $d_0^+ = 72$ and $d_0^+ = 108$ at $y^+ = 15$ . . . . .	77
8.18 Mean boundary layer statistics from the hot-wire measurements for the HRs with $d_0^+ = 72$ . . . . .	77
8.19 Mean boundary layer statistics from the hot-wire measurements for the HRs with $d_0^+ = 108$ . . . . .	78
8.20 Mean boundary layer statistics from the PIV measurements for the HRs with $d_0^+ = 108$ . . . . .	78
A.1 Schematic overview of the single HR setup assembly . . . . .	93
A.2 Schematic overview of the HR array setup assembly . . . . .	94

# List of Tables

4.1	Overview of past studies towards flow-excited Helmholtz-Resonators. Where possible, diameter and frequency are converted to inner-scaled variables. <sup>a</sup> As mentioned in study paper. <sup>b</sup> Calculated using parameters mentioned in study paper . . . . .	30
4.2	Rough design parameter estimates for proposed Helmholtz-Resonators in wind tunnel conditions and for a fuselage in typical cruise conditions. Cruise conditions adopted from Modesti et al. (2021) . . . . .	32
5.1	Overview of experimental conditions used for the design of the experimental setup . . .	34
5.2	Summary of various proposed design strategies . . . . .	35
5.3	Summary of chosen design resonance frequencies at the experimental conditions . . .	36
5.4	Summary of chosen orifice diameters and neck lengths at the experimental conditions .	37
5.5	Overview of possible HRs available to test during the experimental campaign at the experimental conditions. All listed HRs can be tested with both the single HR setup and the 7x7 HR array setup . . . . .	38
5.6	Main parameters for microphone measurements . . . . .	40
5.7	Main parameters of the PIV measurements . . . . .	41
5.8	Main parameters for hot-wire measurements . . . . .	43
6.1	Image processing settings for the cross-correlation method and the sum-of-correlation methods respectively . . . . .	51
7.1	Summary of acoustic characterisation results. The measured resonance frequencies and damping result from the second-order model approximation fit of the measured transfer functions. . . . .	62
7.2	Summary of results from the microphone measurements during the wind tunnel tests. The measured resonance frequencies and damping result from the second-order model approximation fit of the measured transfer functions . . . . .	64
9.1	Length and time scales of resonance for the tested HRs . . . . .	80

# Nomenclature

## Greek Symbols

$\alpha$	Amplification factor
$\delta$	Boundary layer thickness
$\gamma$	Coherence
$\kappa$	Von-Kármán constant
$\lambda$	Wavelength
$\nu$	Kinematic viscosity
$\omega$	Vorticity, frequency
$\phi$	Energy spectrum
$\Pi$	Wake strength parameter
$\rho$	Density
$\tau_w$	Wall shear stress
$\theta$	Momentum thickness
$\xi$	Numerical constant related to resonator damping

## Latin Symbols

$A$	Cavity Area
$a_0$	Speed of sound
$c_f$	Skin friction coefficient
$D$	Cavity diameter
$D(t)$	Detection function
$d_0$	Orifice diameter
$f$	Frequency
$f_0$	Resonance frequency
$F_{ext}$	Driving force
$G(f)$	Frequency transfer function (model)
$g(t)$	Impulse transfer function (model)
$H(f)$	Frequency transfer function (experiment)
$i$	$\sqrt{-1}$ , imaginary unit
$K$	Spring constant

$k$	Turbulent kinetic energy, wavenumber
$L$	Cavity length
$l^*$	Viscous length scale
$m$	Mass
$N$	Ensemble size
$p$	Pressure
$R$	Cavity radius, damping constant
$r_0$	Orifice radius
$Re_\tau$	Friction Reynolds number
$Re_\theta$	Momentum thickness Reynolds number
$Re_x$	Free stream Reynolds number
$S$	Orifice area, non-normalised energy spectrum
$s$	Microphone sensitivity
$T$	Measurement time, period
$t$	Time, neck length
$t^*$	Viscous time scale, end correction to neck length
$T_w$	Time interval length
$u$	Streamwise velocity
$u_\tau$	Friction velocity
$U_c$	Convection velocity
$U_e$ or $U_\infty$	Free stream velocity
$V$	Cavity volume
$v$	Wall-normal velocity
$w$	Spanwise velocity
$w(y/\delta)$	Wake function
$x$	Streamwise direction
$y$	Wall-Normal direction
$Z$	Acoustic impedance
$z$	Spanwise direction

**Superscripts**

- $\cdot'$  Fluctuating component  
 $\cdot^+$  Inner-scaled parameter

**Subscripts**

- $\cdot_{rms}$  Root mean square

**Math Symbols and Operations**

- $\angle$  Phase  
 $\hat{\cdot}$  Local average  
 $\langle \cdot \rangle$  Trace, ensemble averaging  
 $|\cdot|$  Amplitude  
 $\mathcal{F}\{\cdot\}$  Fourier transform  
 $\mathcal{P}$  Turbulence production  
 $\bar{\cdot}$  Time average  
 $\tilde{\cdot}$  Noise-corrected

**Abbreviations**

- BMF Bandwidth-moving filter

- DNS Direct numerical simulation  
FOV Field of view  
HR Helmholtz-Resonator  
JPDF Joint probability density function  
LCS Linear coherence spectrum  
LDA Laser Doppler anemometry  
LEBU Large-eddy break-up  
PH Pinhole  
PIV Particle image velocimetry  
PTU Programmable timing unit  
SPL Sound pressure level  
TBL Turbulent boundary layer  
TI Turbulence intensity  
VITA Variable-interval time averaging  
WJPDF Weighted JPDF

# Introduction

On a typical long-range airliner, fuel costs account for approximately 20 % of the direct operating costs, as visualised in Figure 1.1. The required fuel burn is a direct consequence of the amount of drag generated by the aircraft. Of the total drag of a typical long-range airliner, almost 50 % is skin friction drag. A reduction in the mean skin friction will directly result in a reduced overall drag and reduced fuel burn; this is beneficial in both an environmental and economical aspect.

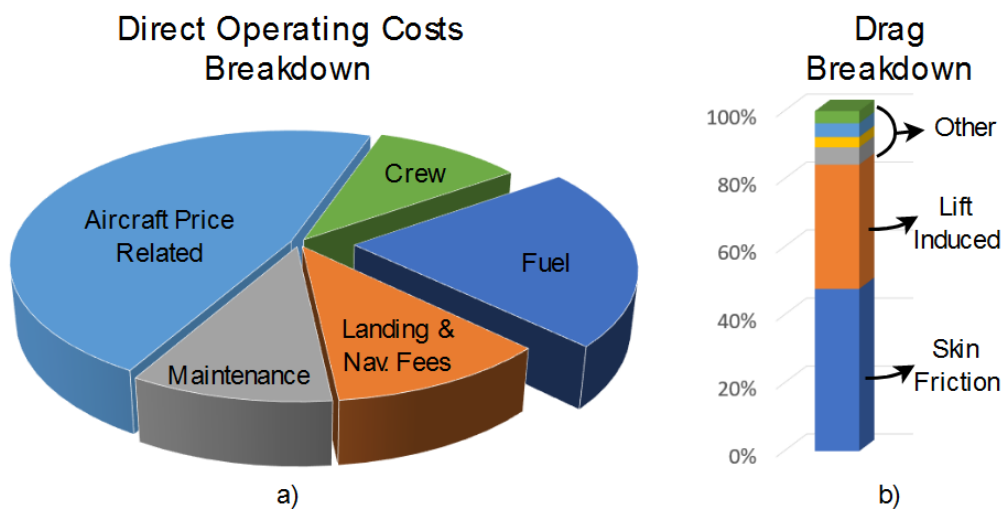


**Figure 1.1:** Breakdown of a) direct operating costs and b) drag for a typical long-range aircraft. After Marec (2001)

With the boundary layer on an aircraft being primarily turbulent, reducing the mean turbulent skin friction has been an active topic of research for decades. Several nature-inspired passive means of flow control have shown potential both from numerical simulations and wind tunnel experiments – with riblets even showing potential for reducing fuel burn in flight tests. However, widespread practical implementation has not yet been achieved. Current flow control methods have limitations such as susceptibility to surface degradation and complex manufacturing, making them not economically viable.

Recent studies towards micro-cavity arrays have shown potential for the attenuation of turbulence intensity in turbulent boundary layer (TBL) flow and a consequent reduction in the mean skin friction. There are indications that Helmholtz-Resonators (HRs) could amplify this effect. HRs are commonly used in acoustic liners to attenuate fan noise when tuned to the blade-passing frequency. HRs can also be tuned to certain spatial and temporal scales of the grazing TBL flow. It is hypothesised that tuning HRs to the near-wall cycle turbulence events could result in a reduction in turbulence intensity – and eventually, a reduction in skin friction – that is greater than what was achieved with the micro-cavity array. This leads to the following research objective:

**To experimentally investigate if there is potential for the use of surface-embedded Helmholtz-Resonators, tuned to the near-wall-cycle events in turbulent boundary layer flow, as a realisable passive flow control method for reducing the mean turbulent skin friction.**

---

This report presents the findings of the literature review and the experimental campaign to answer the following research questions:

1. What flow features within a TBL are linked to the generation of skin friction?
  - (a) What are the dominant flow structures and events in the different regions of a TBL?
  - (b) How do these flow features influence the mean skin friction?
  - (c) How do these flow features change with increasing Reynolds number?
2. What are existing passive flow control methods for reducing turbulent skin friction?
  - (a) How do these methods influence the flow structures within the TBL to achieve the reduction in skin friction?
  - (b) What are the limitations of these methods for full-size aircraft implementation?
3. How can surface-embedded HRs be tuned to the turbulence structures and events that form the near-wall cycle of TBL flows?
  - (a) How can a single HR be tuned to the different flow features within a TBL?
  - (b) How is the tuning of HRs under a grazing TBL different to the acoustic tuning of HRs?
  - (c) How does the excitation of a system of HRs differ from that of a single HR?
  - (d) How do the different methods for tuning HRs translate to full-size aircraft implementation?
4. How pronounced is the pressure-velocity coupling at the exit of a HR and to what degree can this influence the TBL flow?
  - (a) How does a HR change the first and second-order statistics of TBL flow?
  - (b) To what extent are the effects of a HR on the TBL flow different for various tuning methods?
  - (c) What is the streamwise extent of the effects of a HR on the TBL flow?
  - (d) To what extent are the effects on the TBL flow different for a system of HRs compared to a single HR?
  - (e) Can a drag reduction potential be identified from the measured effects of a HR on the TBL flow?

This report is structured as follows. In Chapter 2, the fundamentals of TBLs are reviewed. Subsequently, Chapter 3 presents and assesses several existing passive means of boundary layer flow control. Chapter 4 is dedicated to the working principle of HRs, analysing past research and proposing potential sizing and tuning methods. In Chapter 5, the experimental setup is introduced, as well as the used measurement techniques. Chapter 6 elaborates on how the measurement data is processed. The results for the excitation of HRs are presented in Chapter 7, after which the flow measurements are presented in Chapter 8. The results are discussed in Chapter 9 before conclusions and recommendations are presented in Chapter 10 and Chapter 11 respectively.

# Fundamentals of Turbulent Boundary Layers

This chapter reviews the fundamentals of boundary layers. Whereas extensive reviews can be found in the textbooks from Pope (2000) and White (2006), and the paper by Jiménez (2018), this section focuses on those elements from boundary layers of importance for reducing full-size aircraft skin friction drag. §2.1 briefly touches upon the type of boundary layer on an airliner, after which §2.2, §2.3 and §2.4 explain the main parameters and scales within a TBL. Subsequently, §2.5 introduces the instantaneous flow structures within the different scales of the TBL. Quadrant analysis and spectral analysis, commonly used methods for statistical analysis of TBL flow, are described in §2.6. The effect of increasing Reynolds number is briefly touched upon in §2.7, before concluding remarks on skin friction are made in §2.8.

## 2.1. Boundary Layer on a Full-Size Aircraft

A boundary layer is formed due to the viscous effects of a fluid flowing over a surface. At the wall, the flow has zero velocity, referred to as the *non-slip condition*. With distance from the wall, the boundary layer flow velocity gradually increases from zero to the freestream velocity.

Two types of boundary layers can be distinguished: laminar and turbulent boundary layers. At low Reynolds numbers over smooth surfaces, the boundary layer flow will be laminar. When the Reynolds number exceeds a certain critical value (or surface roughness is induced), the boundary layer transitions to turbulent. As turbulent boundary layers generate more skin friction drag than laminar boundary layers (White, 2006), maintaining laminar flow has been an active topic of research for reducing the overall drag (Bushnell, 2003).

For typical aeronautical purposes, it is often impossible to maintain laminar flow for several reasons, as described by Bushnell (2003). To maintain laminar flow at high Reynolds numbers, levels of surface smoothness would be required that are practically unachievable. Furthermore, there are various elements on an aircraft fuselage that inherently induce effective roughness, such as doors and windows; these will trigger a bypass transition of laminar-to-turbulent flow. As such, the boundary layer on aircraft is primarily turbulent and reducing turbulent skin friction has become an active topic of research.

For this review, the focus lies on reducing the mean skin friction in TBL flows at zero pressure gradient. Surfaces with a low-to-zero pressure gradient on an aircraft include the fuselage, which is a large contributor to the total skin friction due to its large wetted area. In TBL flows with large adverse pressure gradients (e.g. the aft-body of an aircraft), reducing skin friction – and simultaneously the turbulence level – could promote earlier flow separation (Schlichting and Gersten, 2017). This could lead to a large increase in pressure drag.

## 2.2. Turbulent Boundary Layer Parameters

Figure 2.1 shows a visualisation of a typical boundary layer, in which the mean velocity  $\bar{u}$  gradually grows from zero (from the non-slip condition at the wall) to the freestream velocity, denoted by  $U_\infty$  or  $U_e$ . The boundary layer thickness  $\delta$  is then defined as the wall distance where the mean velocity is 99% of the freestream velocity.

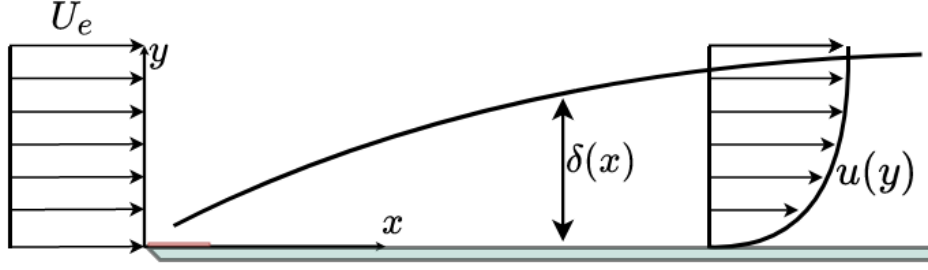


Figure 2.1: Visualisation of a boundary layer with a typical coordinate system. Illustration after Seyyedi et al. (2019)

Figure 2.1 also indicates the typical coordinate used system for boundary layer analysis. The  $x$ -axis is the streamwise direction and the  $y$ -axis denotes the wall-normal direction, with outward from the wall being the positive  $y$ -direction. When considering three-dimensional flow, the  $z$ -direction denotes the spanwise direction. The velocity components are denoted by  $u$ ,  $v$  and  $w$  for the  $x$ -direction,  $y$ -direction and  $z$ -direction respectively.

Starting from a trip or bypass transition, the boundary layer gradually grows downstream, making the boundary layer thickness  $\delta$  a function of streamwise location  $x$ , such that  $\delta(x)$ . For a flat plate TBL, the boundary layer thickness  $\delta(x)$  can be approximated as a function of the freestream Reynolds number  $Re_x$  (Schlichting and Gersten, 2017):

$$\delta(x) \approx \frac{0.37x}{Re_x^{1/5}} \quad (2.1)$$

To describe the state of the boundary layer, typically the friction Reynolds number  $Re_\tau$  is used, which is defined as

$$Re_\tau \equiv \frac{\delta u_\tau}{\nu}. \quad (2.2)$$

Here,  $\nu$  denotes the kinematic viscosity and  $u_\tau$  represents the friction velocity. The friction velocity can be considered the characteristic velocity for both the inner region and the full boundary layer, with one of the main functions of the boundary layer being to convert freestream momentum into wall shear stress (Klewicki, 2010). The friction velocity  $u_\tau$  can be calculated using the wall shear stress  $\tau_w$  and air density  $\rho$ :

$$u_\tau \equiv \sqrt{\frac{\tau_w}{\rho}}. \quad (2.3)$$

The wall shear stress  $\tau_w$  directly follows from the velocity gradient at the wall using

$$\tau_w = \nu \rho \left. \frac{\partial u}{\partial y} \right|_{y=0}. \quad (2.4)$$

The friction Reynolds number from Equation 2.2 gives the ratio of inertial to viscous forces in the boundary layer. Therefore, its value gives a measure of the scale separation between the large scales and small scales within the boundary layer (Klewicki, 2010). The large scales are in the order of the boundary layer thickness  $\delta$  and for the small scales a characteristic viscous length scale  $l^*$  can be defined as

$$l^* = \frac{\nu}{u_\tau}. \quad (2.5)$$

Therefore, the friction Reynolds number  $Re_\tau$  can be rewritten as the ratio of the boundary layer thickness  $\delta$  and the viscous length scale  $l^*$  as

$$Re_\tau = \frac{\delta}{l^*}. \quad (2.6)$$

Similar to the viscous length scale  $l^*$ , a characteristic viscous time scale  $t^*$  can be defined using

$$t^* = \frac{\nu}{u_\tau^2}. \quad (2.7)$$

The inverse of the characteristic time scale  $1/t^*$  is a measure for mean wall vorticity  $\overline{\omega_z}$ . Therefore, it represents the smallest wavelength or highest frequency of the structures and events that are present in the boundary layer (Klewicki, 2010).

### 2.3. Scaling in a Turbulent Boundary Layer

Within a TBL, two types of scaling are used: inner scaling and outer scaling. Typically, the small scales in the boundary layer – as well as the boundary layer statistics in the near-wall regions – follow an inner scaling, whereas the larger scales in the outer regions follow an outer scaling.

With inner scaling, parameters are normalised using the viscous length scale  $l^*$  and velocity scale  $u_\tau$ . The inner-scaled wall-normal distance in the boundary layer then becomes

$$y^+ \equiv \frac{y}{l^*} = \frac{u_\tau y}{\nu}. \quad (2.8)$$

Here the superscript '+' denotes the use of inner-scaled parameters. Similarly, the velocity within a boundary layer is inner scaled as

$$\overline{u}^+ \equiv \frac{\overline{u}}{u_\tau}. \quad (2.9)$$

With outer scaling, the distance to the wall is measured as the ratio to the overall boundary layer thickness  $y/\delta$ . The velocity within the boundary layer is then typically represented as a velocity defect relative to the freestream velocity, following  $U_e - \overline{u}$ .

A mean velocity profile of a TBL flow is plotted using inner-scaled variables and outer-scaled variables in Figure 2.2 and Figure 2.3 respectively. Three main regions can be defined within a TBL:

1. The inner region, in which the TBL parameters are a function of the inner-scaled variables  $y^+$  and  $\overline{u}^+$  only. In the inner region, viscosity has a direct effect on the wall shear stress (Pope, 2000).
2. The outer region, in which the TBL parameters are a function of the outer-scaled variables  $y/\delta$  and  $U_e - \overline{u}$ . In the outer layer, there is a negligible effect of viscosity on the mean velocity (Pope, 2000). Turbulence effects are dominant over viscous effects.
3. The overlap region, in which the TBL parameters can be described using both inner-scaled variables and outer-scaled variables. Commonly, the overlap region is referred to as (part of) the logarithmic region.

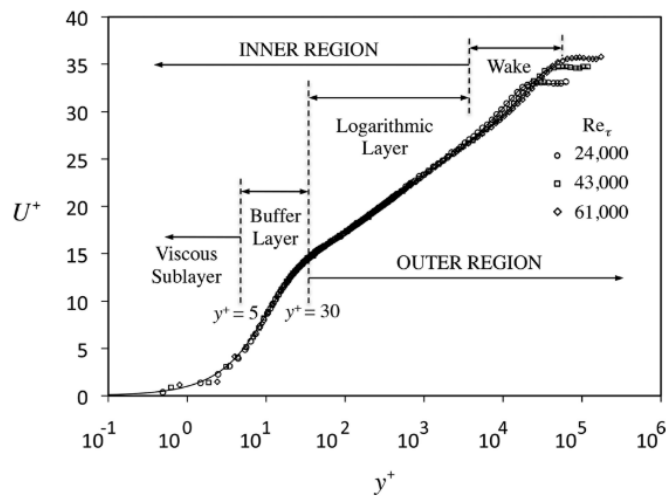


**Figure 2.2:** Inner-scaled mean velocity profile of a TBL at various  $Re_\tau$ . From Perlin et al. (2016)

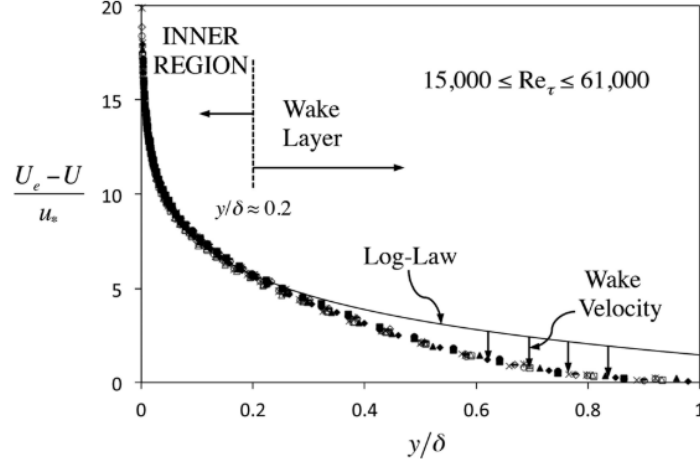


**Figure 2.3:** Outer-scaled mean velocity profile of a TBL at various  $Re_\tau$ . From Perlin et al. (2016)

Pope (2000) compares the inner-scaled wall distance  $y^+$  to a local Reynolds number within the TBL. Following this comparison, the value of  $y^+$  describes the relative importance of viscous and turbulence events. In the inner region, for  $y^+ < 50$  a viscous wall region can be defined which consists of the viscous sublayer ( $y^+ < 5$ ) and the buffer layer. In the viscous sublayer  $\bar{u}^+$  is solely a function of  $y^+$  and a linear relation between the two can be established.

In the buffer region the velocity profile transitions from a linear profile to a logarithmic profile. This logarithmic profile can be described by the logarithmic law of the wall using either inner-scaled variables as

$$\bar{u}^+ = \frac{1}{\kappa} \ln y^+ + B \quad (2.10)$$

or outer-scaled variables in a velocity-defect law as

$$\frac{U_e - \bar{u}}{u_\tau} = -\frac{1}{\kappa} \ln \frac{y}{\delta} + B_1. \quad (2.11)$$

Here,  $\kappa$  is the von-Kármán constant and  $B$  and  $B_1$  are offsets (typical values are  $\kappa = 0.384$  and  $B = 4.17$ , see Chauhan et al. (2009), and  $B_1$  is relatively small, see Pope (2000)).

The logarithmic law of the wall is valid between approximately  $y^+ > 50$  and  $y/\delta < 0.2$ . Beyond  $y/\delta > 0.2$ , the wake region starts. In the wake region, the mean velocity gradually deviates from the logarithmic law. To account for this deviation, the law of the wake is introduced using outer-scaled variables in a velocity-defect law as

$$\frac{U_e - \bar{u}}{u_\tau} = \frac{1}{\kappa} \left( -\ln \left( \frac{y}{\delta} \right) + \Pi \left[ 2 - w \left( \frac{y}{\delta} \right) \right] \right). \quad (2.12)$$

Here,  $w \left( \frac{y}{\delta} \right)$  is defined as the wake function which satisfies the boundary conditions  $w(0) = 0$  and  $w(1) = 1$ .  $\Pi$  is defined as the wake-strength parameter, with an approximate value of  $\Pi = 0.44$  for zero-pressure-gradient TBL flows (Chauhan et al., 2009).

## 2.4. Turbulence Intensity and Turbulence Kinetic Energy

The regions within the TBL are defined using the mean velocity  $\bar{u}$ . However, a typical characteristic of TBL flow is that turbulence structures and events induce velocity fluctuations. The instantaneous velocity  $u$  at any point in the TBL can be described as the sum of the time-averaged mean velocity  $\bar{u}$  and a velocity fluctuation  $u'$ , such that

$$u = \bar{u} + u'. \quad (2.13)$$

By definition, the time average of the velocity fluctuations is zero. However, the ratio of the root-mean square of the velocity fluctuations to the mean velocity can be used as a measure for turbulence intensity  $TI$ :

$$TI = \frac{u'_{rms}}{\bar{u}}. \quad (2.14)$$

Here,  $u'$  describes the velocity fluctuations in the  $x$ -direction. Similarly,  $v'$  and  $w'$  denote the velocity fluctuations in the  $y$ -direction and  $z$ -direction respectively.

The Navier-Stokes equations can be rewritten by substituting the velocity with the sum of the mean velocity and the velocity fluctuations. This is referred to as Reynolds decomposition. From this decomposition, an additional unknown arises in the Navier-Stokes equations: the Reynolds stress  $\langle u'_i u'_j \rangle$ . This is a second-order tensor with  $i$  and  $j$  indices for the flow directions. The diagonal components of the tensor indicate normal stresses, whereas the off-diagonal components denote the shear stresses of the flow (Pope, 2000).

The Reynolds stress tensor is a measure of the turbulence kinetic energy (TKE)  $k$ . Its value is defined as half of the trace of the Reynolds stress tensor (Pope, 2000):

$$k = \frac{1}{2} \langle \mathbf{u}' \cdot \mathbf{u}' \rangle = \frac{1}{2} \langle u'_i u'_i \rangle. \quad (2.15)$$

Using boundary-layer approximations, an equation for the TKE can be established. While the equation itself is omitted from this review, it is noted that the equation is a balance between mean-flow convection, production, pseudo-dissipation, viscous diffusion, turbulent convection and pressure transport (Pope, 2000). Based on DNS data – see for instance Spalart (1988) – the relative contribution of each component can be analysed at the different  $y^+$ -stations within the boundary layer.

## 2.5. Instantaneous Flow Structures within a Turbulent Boundary Layer

This section aims to describe the different instantaneous flow structures in a TBL, how they induce the various velocity fluctuations and how they then contribute to the generation of turbulence. The structures can be categorised as those within the inner region of the TBL and those within the outer region. Whereas extensive reviews are presented in the works of Kline and Robinson (1990), Robinson (1991) and Pope (2000), this section emphasises those structures and events most important to the production of turbulence. In §2.5.1, the inner-region structures are introduced, after which in §2.5.2 the outer-region structures are described.

### 2.5.1. Flow Structures and Events in the Inner Regions

In Figure 2.4 the contribution of each component of the TKE balance is shown in the inner region ( $y^+ < 50$ ), for a TBL at  $Re_\theta = 1410$ . The peak turbulence production is within the buffer region around  $10 < y^+ < 15$  – although at large  $Re_\tau$  the bulk turbulence production originates from the outer regions. This region coincides with flow structures and events that form what is commonly referred to as the near-wall cycle.

In Figure 2.5 a conceptual visualisation of the near-wall cycle is presented, which extends to  $y^+ \approx 100$ . Robinson (1991) categorises the various structures and events near the wall as follows:

1. Low-speed streaks in the viscous sublayer
2. Ejections of low-speed fluid outward from the wall
3. Sweeps of high-speed fluid towards the wall
4. Vortical structures of various forms (e.g. horseshoe and hairpin vortices)
5. Internal shear layers around  $y^+ \approx 80$
6. Near-wall "pockets", visible as regions swept clean of flow-visualisation fluid

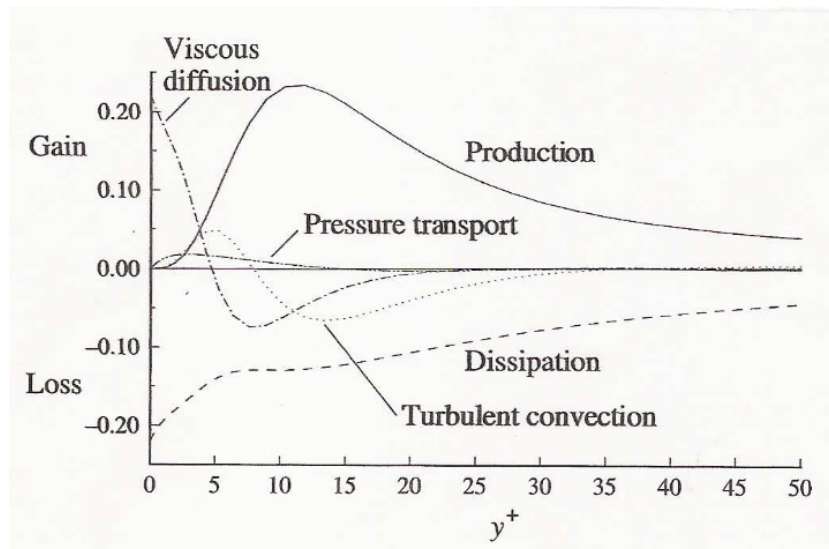


**Figure 2.4:** Turbulence kinetic energy budget in the inner region of the turbulent boundary layer. From Pope (2000) based on DNS data from Spalart (1988)

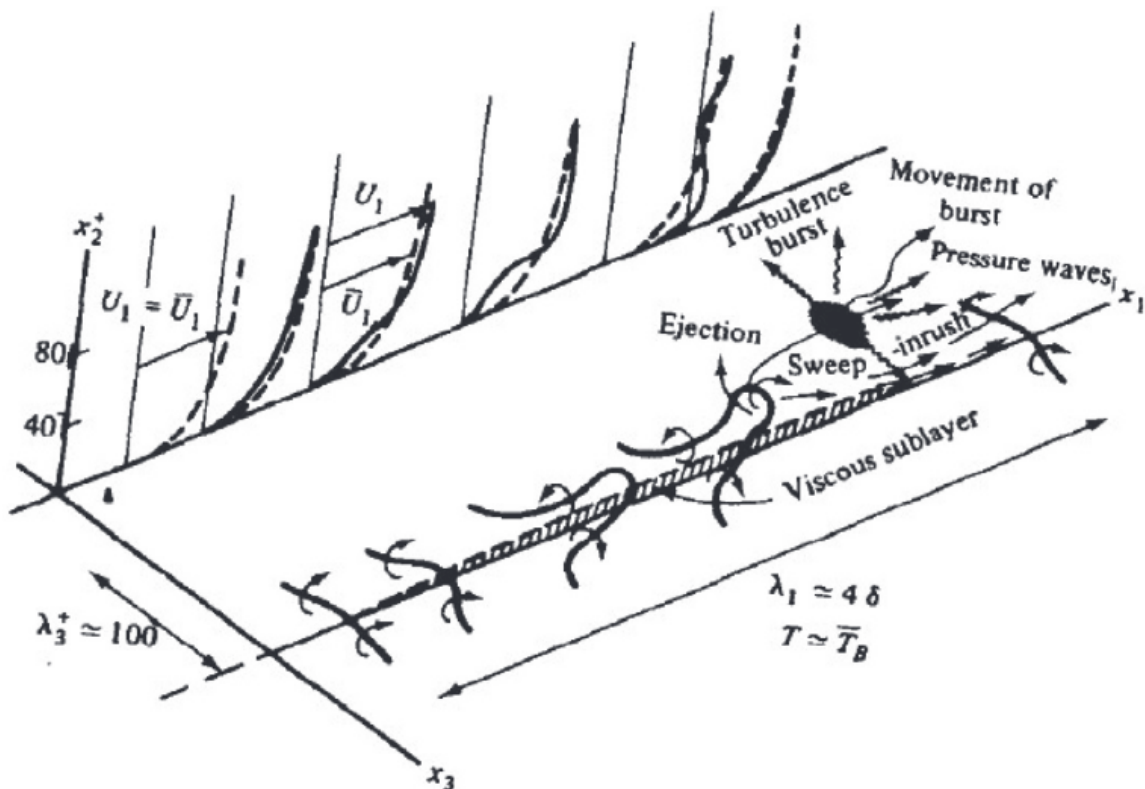


**Figure 2.5:** Visualisation of the near-wall cycle. From Hinze (1975)

The low-speed streaks appear in the region from  $0 < y^+ < 10$  and have been visualised in experiments by Kline et al. (1967). Further experiments by Smith and Metzler (1983) have characterised the low-speed streaks with a typical spanwise spacing of  $100l^*$  and a streamwise length that can extend up to  $1000l^*$ . With increasing downstream distance, the streaks start to lift and roll up in counter-rotating quasi-streamwise vortices, as is visualised in Figure 2.5. These counter-rotating vortices roll

up as hairpin vortices as they travel downstream and lift away from the wall. This is referred to as ejection. Subsequently, the structures burst and break down into smaller scales. As ejection moves low-speed fluid from the wall, simultaneously high-speed fluid is moved towards the wall in adjacent regions, known as sweeps (Pope, 2000).

Smith et al. (1991) propose a model that describes the near-wall cycle as a self-regenerative cycle with the hairpin vortices as key elements. In the roll-up and lifting of the hairpin vortices their tails are then responsible for regenerating or maintaining the low-speed streaks. This is explained as being the cause for the relatively long streamwise length of the low-speed streaks. Using the model, the different near-wall structure and event categories from Robinson (1991) can be combined. Robinson (1991) also presents alternative models for explaining the near-wall cycle, as historically there was no consensus about the near-wall cycle being of autonomous or self-regenerative nature.

For the consideration of turbulence production, sweep and ejection events are of major importance. In the TKE balance equation, production is calculated as (Pope, 2000):

$$\mathcal{P} = -\langle u'v' \rangle \frac{\partial \bar{u}}{\partial y}. \quad (2.16)$$

An event that combines a negative streamwise velocity fluctuation  $u'$  with a positive wall-normal fluctuation  $v'$  (such as ejections) or a positive streamwise velocity fluctuation  $u'$  with a negative wall-normal velocity fluctuation  $v'$  (such as sweeps) will result in positive turbulence production. It was estimated by Corino and Brodkey (1969) that sweep and ejection events account for 70% of the  $uv$ -component of the Reynolds stress.

### 2.5.2. Flow Structures and Events in the Outer Regions

Robinson (1991) presents two categories of large-scale flow structures that scale with the boundary layer thickness  $\delta$  and appear in the outer regions of the boundary layer:

1. Large scale motions in the outer regions of the boundary layer
2. Shear layer "backs"

It has been shown that the near-wall cycle has a nearly fixed region in terms of wall distance of around  $70 < y^+ < 100$  (Klewicki, 2010). Therefore, to achieve a clear scale separation between the near-wall cycle and the large-scale motions, relatively large values for  $Re_\tau$  are needed. This also means that with increasing  $Re_\tau$  the outer region and the larger-scale structures relatively become more important (Mathis et al., 2009).

As experiments and DNS in early research considered relatively low Reynolds numbers  $Re_\tau$ , the large-scale motions in the outer layers of TBL flow have not been studied as extensively as those in the near-wall cycle. Recent experiments and DNS simulations at higher Reynolds numbers have given insight in the structures of the large-scale outer region motions, an overview of which is presented in Mathis et al. (2009). Predominantly, the finding of elongated regions of low momentum fluid in the outer part of the log-region by Hutchins and Marusic (2007a) is described. These structures were denoted 'superstructures' and were found to have a spanwise width of around  $0.3\delta - 0.5\delta$  with a streamwise length of up to  $20\delta$ . In follow-up research, Hutchins and Marusic (2007b) hypothesise that the large-scale structures amplify the energy of the near-wall cycle. While the regenerative nature of the near-wall cycle is not modified fundamentally, an increase in energy in the outer part of the log-region will increase the velocity fluctuations near the wall. This hypothesis was further supported by experiments by Mathis et al. (2009) and is commonly referred to as scale modulation (Baars et al., 2016).

## 2.6. Statistical Analysis of the Turbulent Boundary Layer

Up to now, the discussion on TBL flow has primarily considered instantaneous flow structures. To characterise these structures, a variety of statistical methods can be used. Two of those methods are introduced in this subsection: quadrant analysis in §2.6.1 and spectral analysis in §2.6.2.

### 2.6.1. Quadrant Analysis

Sweep and ejection events within the near-wall cycle have been attributed to be responsible for most of the near-wall production of the Reynolds shear stress (Corino and Brodkey, 1969). Therefore, insight into the occurrence and intensity of these events is valuable when assessing flow control methods. This is done through the  $uv$ -quadrant decomposition of the velocity fluctuations, as visualised in Figure 2.6. Events in Q2 have been shown to correspond to ejection events, whereas events in Q4 correspond to sweep events. A thorough review of the quadrant analysis technique is presented by Wallace (2016).

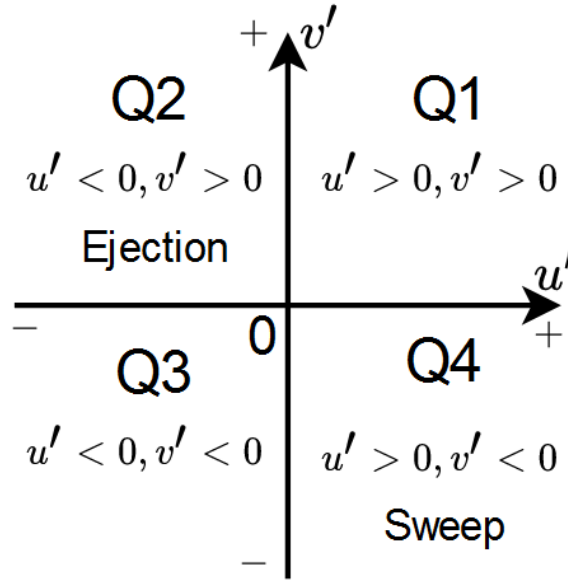


Figure 2.6: Quadrant  $uv$ -decomposition. After Pope (2000)

Using quadrant analysis, both the occurrence and relative strength of the turbulence events can be analysed. From a time series of  $u$ - and  $v$ -measurements, each individual data point can be plotted in either of the four quadrants. This leads to a scatter plot showing the relative occurrence of each quadrant. This scatter plot is commonly referred to as the joint probability density function (JPDF) (Wallace, 2016).

Subsequently, when each data point is weighted according to the corresponding magnitude of the velocity fluctuations  $u'$  and  $v'$ , this shows the relative strength of the events within each quadrant. This version of the quadrant plot is then referred to as the weighted joint probability density function (WJPDF). The magnitude of each entry in the WJPDF is indicative of the fractional contribution of each event to the Reynolds shear stress (Wallace, 2016).

### 2.6.2. Spectral Analysis

The energy spectrum gives a measure of how the TKE is distributed amongst the different scales in the TBL. In e.g. the streamwise direction, the energy spectrum  $\phi_{uu}(k_x)$  can be constructed from a time series of velocity fluctuations  $u'(t)$ . Here,  $k_x$  is the streamwise wavenumber, which relates to the wavelength  $\lambda_x$  as

$$k_x = \frac{2\pi}{\lambda_x}. \quad (2.17)$$

The process of generating an energy spectrum is explained and outlined by e.g. Pope (2000), Mathis et al. (2009) and Baars and Marusic (2020). Recall that turbulence intensity relates to the root-mean-square of the velocity fluctuations  $u'_{rms}$ . The variance of the velocity fluctuations  $\overline{u'^2}$  directly relates to the spectral energy integrated over the wavenumbers using

$$\overline{u'^2} = \int \phi_{uu} dk_x. \quad (2.18)$$

Therefore, analysing the energy spectrum gives an insight into the contribution of events with a certain wavenumber to the overall turbulence intensity. Typically, for analysis purposes, the pre-multiplied energy spectrum  $k_x \phi_{uu}(k_x)$  is used, plotted against either the wavenumber  $k_x$  or the wavelength  $\lambda_x$ .

The energy spectrum can be obtained from either DNS data or an experimental time series, from e.g. hot-wire anemometry. From DNS data, directly the wavenumber energy spectrum can be generated. From a hot-wire time series, the frequency energy spectrum is obtained, requiring frequency-to-wavenumber conversions (Baars and Marusic, 2020). From a known frequency  $f$  the corresponding wavenumber can be computed as

$$k_x = \frac{2\pi f}{U_c}. \quad (2.19)$$

Here,  $U_c$  is the convection velocity, the velocity with which the structures in the different regions of the TBL appear to travel downstream. In the outer region and log region of the TBL the convection velocity is approximately equal to the mean boundary layer velocity, but then remains equal to an inner-scaled value of  $U_c^+ \approx 10$  (Liu and Gayme, 2020; Drózdź and Elsner, 2017) in the buffer layer and viscous sublayer. This is plotted in Figure 2.7. Sometimes, for the generation of an energy spectrum, the convection velocity is taken as the mean boundary layer velocity for all  $y^+$ . This can lead to magnitude discrepancies around the near-wall region.

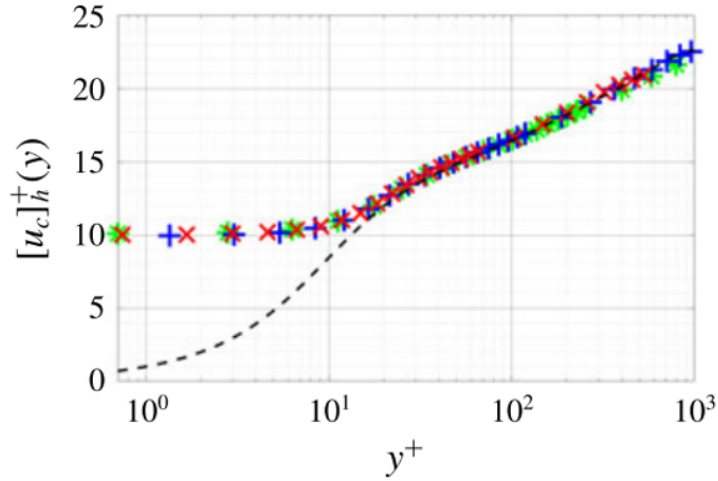


**Figure 2.7:** Measurements of inner-scaled convection velocity  $U_c^+$  in a turbulent boundary layer. Dotted line denotes mean boundary layer velocity  $\bar{u}^+$ . From Liu and Gayme (2020)

When the energy spectra are calculated at various  $y^+$ -stations in the TBL, an iso-contour plot of the energy spectrum can be made. An example of such an energy spectrum at  $Re_\tau = 7300$  is shown in Figure 2.8. The two plus signs denote the locations of what is referred to as the inner spectral-peak (at  $y^+ = 10$  and  $\lambda_x^+ = 1000$ ) and the outer spectral-peak (at  $y/\delta = 0.06$  and  $\lambda_x = 6\delta$ ), a naming convention introduced by Hutchins and Marusic (2007a).

The inner spectral-peak is fixed in terms of inner-scaled variables at  $y^+ = 15$  and  $\lambda_x^+ = 1000$ . The inner peak corresponds to the location of the near-wall low-speed streaks found by Kline et al. (1967) and the initiation of the bursting process of these streaks (Pope, 2000). It also coincides with the  $y^+$ -station of peak turbulence production as found from the DNS data from Spalart (1988). The wavelength  $\lambda_x^+ = 1000$  gives an indication of the streamwise length and frequency of these events.

The outer spectral-peak was found by Hutchins and Marusic (2007a) to follow an outer scaling and is typically located around  $z/\delta = 0.06$  and  $\lambda_x = 6\delta$  (although this depends on the Reynolds number, see §2.7). The magnitude of this peak gives an indication of the energy of the 'superstructures' within the outer log-region. Therefore, it can also be used as a measure of how much the outer scales modify the intensity and physical scales of the universal inner-peak. That is, there is a nonlinear interaction between the larger scales and inner scales. While the peak turbulence production remains at the inner-peak, at higher  $Re_\tau$  actually the bulk production of turbulence is stemming from the log-region.

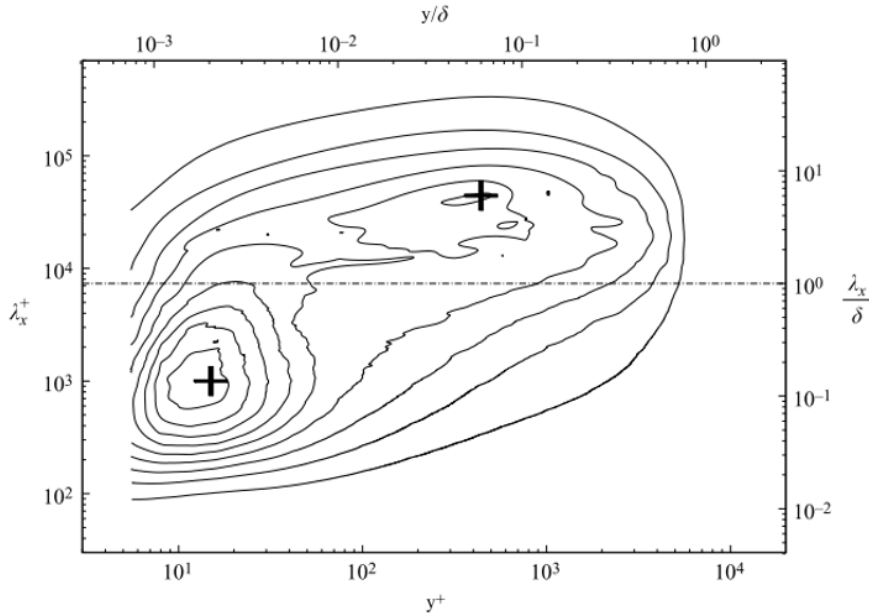


**Figure 2.8:** Iso-contour plot of a streamwise velocity fluctuation pre-multiplied energy spectrum. Both inner and outer scaling are shown. From Mathis et al. (2009)

## 2.7. Reynolds Number Effects

The notion of the outer spectral-peak in the energy spectrum of a TBL gives a good starting point for discussing the effect of increasing Reynolds number on the structures in the outer regions and the effect this has on the amplification of the near-wall cycle. Recall that the friction Reynolds number  $Re_\tau$  gives a direct measure of the boundary layer thickness  $\delta$  with respect to the viscous length scale  $l^*$ . With the inner region having a fixed size in terms of the viscous length scale of around  $y^+ \approx 100$ , increasing  $Re_\tau$  directly indicates an increase in the relative size of the outer region with respect to the inner region.

With the superstructures as found by Hutchins and Marusic (2007a) following an outer scaling, increasing Reynolds number will also increase the relative size of and thus energy within these structures with respect to those in the near-wall region. Therefore, an increase in the amplification effect of the superstructures on the near-wall-cycle events can be expected. Figure 2.9 shows the effect of increasing  $Re_\tau$  from 2800 to 650,000 on the pre-multiplied energy spectra. The plus in each plot represents the location of the inner spectral-peak, which shows to be at  $y^+ \approx 15$  for all Reynolds numbers. The dotted line represents the middle of the log-region, which shows to coincide with the location of the outer spectral-peak. With increasing Reynolds number, it moves away further from the wall in terms of  $y^+$ , but closer to the wall relative to the boundary layer thickness  $\delta$ .

With increasing Reynolds number, the outer peak becomes more apparent in the energy spectra in Figure 2.9. Additionally, Hutchins and Marusic (2007a) have suggested that with increasing Reynolds number the magnitude of the outer peak in terms of the energy spectrum increases, indicating increased activity of the superstructures associated with the outer part of the log-region. This then leads to an increase in the magnitude of the inner peak according to the inner-outer interaction models. The proportional contribution of the large-scale outer structures to the total energy spectrum is then increased.

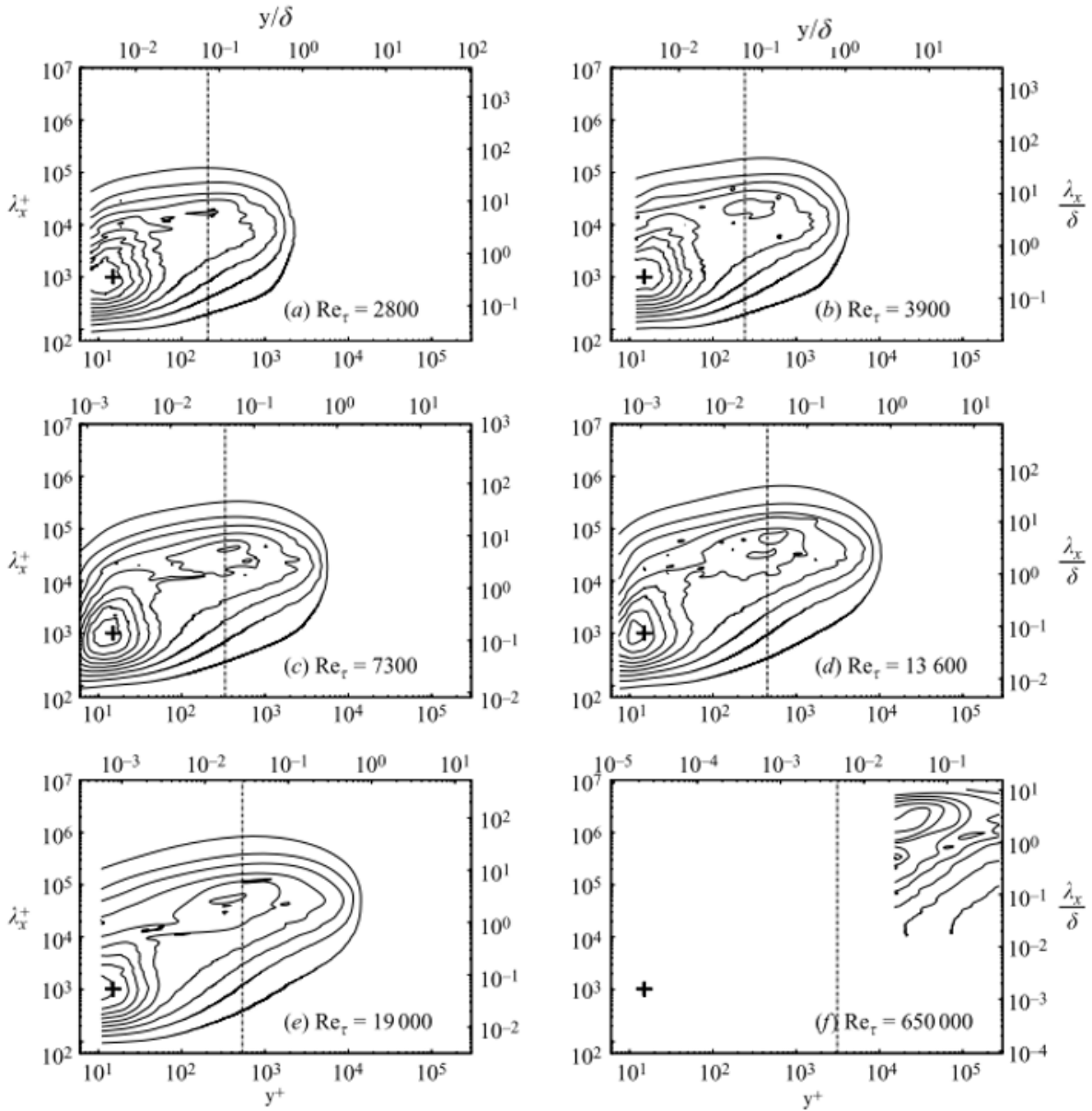


Figure 2.9: Pre-multiplied energy spectra at various  $Re_\tau$  from 2800 to 650,000. Modified from Mathis et al. (2009)

## 2.8. Concluding Remarks on Skin Friction

This chapter has covered some of the fundamentals that will show to be useful in assessing the effect on skin friction. Skin friction of a boundary layer is usually defined using the skin friction coefficient  $c_f$ , which is a normalised measure of the wall shear stress  $\tau_w$ :

$$c_f = \frac{\tau_w}{\frac{1}{2}\rho U_e^2} = 2 \frac{u_\tau^2}{U_e^2}. \quad (2.20)$$

With the magnitude of the wall shear stress directly related to the velocity gradient at the wall, as was shown in Equation 2.4, changing this velocity gradient will have a direct impact on the magnitude of the skin friction coefficient.

The velocity gradient at the wall – and thus within the viscous sublayer – is directly influenced by the structures and events within the regenerative near-wall cycle. These are responsible for the peak turbulence production close to the wall. The amplitude of these near-wall cycle events can be magnified

by the structures in the outer region, without affecting the regenerative nature of the near-wall cycle. With increasing Reynolds number, the outer layer structures get more pronounced, skewing the velocity fluctuations in the near-wall events. This way, the large-scale outer region motions indirectly influence the mean velocity gradient at the wall. Nevertheless, the relationships between (fluctuating) turbulence quantities and the mean skin friction are not straightforward. Analysis methods and metrics have been developed but are not further considered in this study.

The main point made is that reducing turbulent skin friction can be achieved by reducing the intensity of the near-wall cycle. This can be done by either

1. Directly suppressing the sweep and ejection events responsible for the majority of turbulence production
2. Reducing the amplification effect on the near-wall cycle by reducing the energy of the large-scale outer structures

These two methods will form the basis for the remainder of this review, in which the focus will be on methods of boundary layer flow control to reduce turbulent skin friction.

# Passive Flow Control for Skin Friction Reduction

Following a thorough understanding of the various flow structures within the TBL, research efforts have been focused on how these structures can be controlled to achieve a net benefit in reducing turbulent skin friction. Flow control can be achieved by active or passive means. Passive flow control would be preferred over active flow control as no power input is required to operate the system. Furthermore, passive means of flow control typically have reduced complexity as there is no need for electrical and mechanical components or control loops.

This chapter focuses on the different strategies towards passive control of TBL flow aimed at reducing turbulent skin friction specifically. In §3.1 these strategies, based on the different regions within the TBL, are outlined, after which §3.2 and §3.3 give examples of flow control based on the large scales and small scales within TBL flow. In §3.4 an alternative method for small-scale flow control is introduced using a micro-cavity array, based on which in §3.5 the hypothesis is made for the use of Helmholtz-Resonators to achieve small-scale flow control using aero-acoustic coupling.

## 3.1. Control Strategies for Skin Friction Reduction

Strategies for flow control can be divided into those that either (1) interfere with the events in the near-wall cycle or (2) interfere with the larger-scale motions in the outer layer (Corke and Thomas, 2018). These strategies only become distinctly different with sufficient scale separation within the TBL, at higher Reynolds numbers  $Re_\tau$ . Recall that sweep and ejection events are of major importance when considering turbulence production in a TBL. Therefore, if a flow control method limits the intensity of those events, turbulence production will reduce and a benefit in skin friction could be achieved. The larger scale motions amplify the magnitude of the near-wall cycle events. Therefore, interfering with these larger-scale structures can reduce turbulence production by reducing the magnitude of the velocity fluctuations associated with the near-wall cycle events.

Another distinction between different methods of boundary layer flow control can be made of those that add skin friction or pressure drag by either adding physical surfaces or inducing roughness. This inherently reduces the benefits of drag reduction, as first, the additional drag increase needs to be overcome before a net benefit can be achieved. Therefore, limiting the additional drag increase from the boundary layer flow control method will directly result in an increased net benefit.

Extensive reviews of existing methods of both active and passive drag reduction are presented by Perlin et al. (2016) and Corke and Thomas (2018). The remainder of this chapter only highlights those methods of interest for this study.

## 3.2. Large-Scale Boundary Layer Flow Control

The primary method of achieving large-scale boundary layer flow control has been with large-eddy break-up devices (LEBUs). LEBUs are typically thin flat plates or aerofoils that are placed within the outer region of the TBL. Typical heights are between  $0.1\delta < y < 0.8\delta$  (Chan et al., 2021). The working principle of LEBUs originates from unsteady vortex shedding in the wake of a LEBU (Corke and Thomas, 2018).

Based on numerical simulation, Chan et al. (2021) distinguish three regions of downstream effects in the wake of a LEBU and use those to assess the potential for drag reduction. In the first region, unsteady vortex shedding in the wake results in vortices travelling towards both the inner regions and the outer regions of the TBL. The so-called inner vortices dampen the velocity fluctuations near the wall, an effect that becomes most pronounced in the second region. Here, the inner vortices directly interact with the viscous sublayer and the largest amount of local skin friction reduction is found. In the third region, the inner vortices move away from the wall which has been associated with a regeneration of Reynolds stresses (Chan et al., 2021).

Despite (significant) reductions in local skin friction, typically no net benefit in terms of drag reduction is found with LEBUs (Corke and Thomas, 2018; Chan et al., 2021). The addition of thin flat plates in the flow inherently yields a drag increase which needs to be overcome first. Additionally, the regeneration of Reynolds stresses in the third region can yield a small local skin friction increase (Chan et al., 2021). Combined with the difficulty of the practical implementation of LEBUs to full-size aircraft, this method is not likely to be pursued.

### 3.3. Small-Scale Boundary Layer Flow Control

One of the most widely researched methods of small-scale boundary layer control has been riblets. Inspired by sharkskin, riblets were first investigated by Walsh (1983). Various studies have shown potential for drag reduction of up to 10% (Garcia-Mayoral and Jimenez, 2011; Perlin et al., 2016). Riblets have been flight tested which confirmed a drag reduction potential through reduced fuel burn, even up to larger Reynolds numbers and Mach numbers (McClean et al., 1987; Bushnell, 2003).

Typical design parameters for riblets include the riblet height and riblet spacing. Two regimes of influencing turbulent skin friction can be distinguished, as a function of riblet spacing: (1) the viscous regime at small spacing, in which the skin friction reduction increases with increasing spacing and (2) the  $k$ -roughness regime, in which the skin friction increases again with increasing spacing. In the viscous regime, drag reduction is achieved through the concept of protrusion height and the drag reduction scales linearly with increasing riblet spacing (Garcia-Mayoral and Jimenez, 2011). Beyond the optimal spacing of around  $l^*$  the viscous regime starts to break down. Garcia-Mayoral and Jimenez (2011) describe the formation of coherent spanwise vortices, which are referred to as 'rollers'. These are Kelvin-Helmholtz-like instabilities that are a typical consequence of an inflection-type mean velocity profile, which appears with sufficient roughness height or surface porosity. The formation of such spanwise rollers limits the maximum achievable drag reduction of riblets.

Besides the inherent roughness effect, full-size aircraft implementation of riblets is limited by economic viability (Bushnell, 2003). As the effectiveness of riblets is highly dependent on their size and spacing, they can be susceptible to wear and tear and surface degradation over time. This could lead to high maintenance costs, which counteracts the economic benefits of reducing fuel burn with reduced drag.

Other nature-inspired methods for small-scale boundary layer flow control have been investigated: compliant walls (Carpenter et al., 2000; Fukagata et al., 2008), permeable walls (Hahn et al., 2002) and superhydrophobic surfaces (Martell et al., 2009). While a potential for drag reduction has been shown using DNS simulations or experiments, major challenges need to be overcome before full-size aircraft implementation might become feasible. For compliant walls, while average drag reductions of 17% have been found in experiments, Bandyopadhyay et al. (2005) found that ageing effects reduce the benefits significantly after days of testing. Superhydrophobic surfaces have been shown to be susceptible to surface degradation and are typically fragile (Perlin et al., 2016). Therefore, implementing these flow control methods could lead to high maintenance costs, reducing their economic viability.

### 3.4. Micro-Cavity Array for Small Scale Boundary Layer Flow Control

A different approach towards modifying the small-scale structures to achieve turbulent skin friction reduction has been researched by Silvestri et al. (2017a; 2017b; 2018). In this string of research, an array of surface-embedded micro-cavities has been used to attempt to attenuate the intensity and duration of sweep events in the TBL.

In earlier research, Choi and Fujisawa (1993) had shown that a small net drag reduction can be achieved with a single rectangular cavity of size  $180 < d^+ < 240$ , where  $d^+$  denotes the inner-scaled cavity dimension. Furthermore, Maa (1998) used a micro-perforated panel as part of research towards sound absorption, a so-called acoustic liner. Based on this research, Silvestri et al. (2017a) hypothesised that this type of panel could also be used to absorb sweep events by "*dampen[ing] the coherent structures and disrupt[ing] the bursting cycle, which is responsible for the shear stress and viscous drag in the inner wall region*". To avoid disturbances to the spanwise and streamwise velocity profiles, cavity diameters of  $20 < d^+ < 150$  were considered. This was based on an analysis done by Chang et al. (2006) of TBL flow over an open cavity.

The initial research by Silvestri et al. (2017a) showed potential for attenuating sweep events and reducing turbulence production with all micro-cavity arrays tested. The sweep events were analysed through variable interval time-averaging (VITA) analysis of a streamwise velocity time series obtained with hot-wire anemometry. The effectiveness of the array depended significantly on the cavity diameter. It was found that a cavity diameter of  $d^+ \approx 60$  was the optimal size for attenuating sweep and turbulence intensity, with reductions of 14% and 13% respectively. For  $d^+ < 30$ , the cavity was too small to effectively capture the sweep events. For  $d^+ > 105$ , the effectiveness of the tested cavities started to reduce significantly. For these diameters, the cavity becomes too large, such that the shear layer starts to break down and turbulence production is increased as a consequence.

In follow-up research, Silvestri et al. (2017b) found that changing the cavity depth has no significant effect, but that a single backing cavity – to which all micro-cavities are connected – could further reduce sweep and turbulence intensity. Silvestri et al. (2018) investigated a range of single backing cavity volumes and individual backing cavities via the use of a mesh, both of which are shown in Figure 3.1. It was found that increasing the backing cavity volume led to greater attenuation of sweep and turbulence intensity. The individual backing cavities showed a small reduction in effectiveness, but it should be noted that the mesh used for the individual backing cavities reduced the overall backing cavity volume by 18%. No specific design principles were presented for the tested volumes of both the common backing cavity and the individual backing cavities.

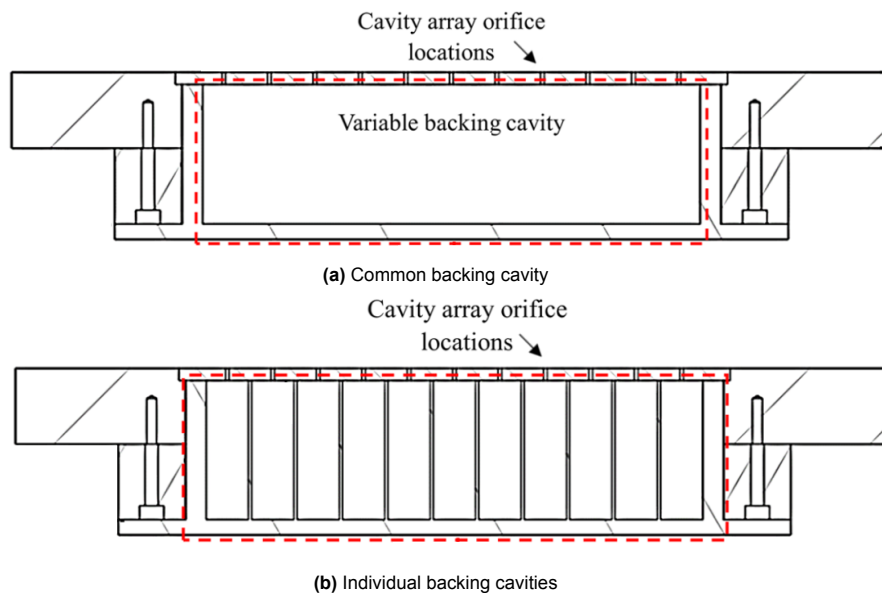


**Figure 3.1:** Micro-cavity array with different types of backing cavities. Modified from Silvestri et al. (2018)

Based on the experimental data, Silvestri et al. (2018) concluded that the sweep events are weakened by damping their energy with the micro-cavity array. This damping was then achieved through friction losses in the neck and the dissipation of energy in the large backing cavity. It should be noted that in the experimental studies, only hot-wire measurements were taken at a single downstream location of

the micro-cavity array. No spatial measurements were taken. Furthermore, to change the inner-scaled cavity diameter, in some cases, the freestream velocity was altered. This then also changes the spacing between the cavities in the array. The effect of varying spacing was not investigated. Therefore, the observed changes between the various cavity diameters tested might be the compound effect of changing cavity diameter and cavity spacing.

From a DNS simulation of the most effective array-backing cavity from the study by Silvestri et al. (2018), Bhat et al. (2021) concluded that the micro-cavities dampen the wall-normal velocity fluctuations in the log region, which then dampens the energy from the sweep and ejection events. This then also leads to a reduction in turbulence intensity and a weakening of the Reynolds shear stress in the buffer and log regions.

### **3.5. Potential for Aero-Acoustic Coupling for Boundary Layer Control**

One of the studies that the work from Silvestri et al. (2017*a*; 2017*b*; 2018) and Bhat et al. (2021) was based on, was the research on the use of a Helmholtz-Resonator for passive TBL flow control (Ghanadi et al., 2014*a*; 2014*b*; 2015 and Ghanadi, 2014). It was found that when the orifice diameter of the HR approached the thickness of the inner layer of the TBL, a reduction in sweep intensity and duration could be achieved. However, the sizing of the orifice and the cavity of the HR was not done to directly target specific structures or events in the TBL.

Arrays of HRs are widely used within the aerospace industry in acoustic liners to attenuate fan noise in turbofan engines by absorbing acoustic energy (Azimi et al., 2014). Therefore, it is hypothesised that an array of surface-embedded HRs could be used to attenuate the turbulence and sweep intensity to reduce the overall skin friction. For this, the HRs would be tuned to the velocity and pressure scales of the near-wall turbulence structures following the initial study from Silvestri et al. (2018), who showed the potential of a very similar hypothesis based on the work from Maa (1998) towards a micro-perforated plate for the absorption of sound.

# Helmholtz-Resonators

This chapter focuses on the concept of the Helmholtz-Resonator and its working principles. First, the concept of a single HR is introduced in §4.1, after which a system of two HRs is introduced in §4.2. Subsequently, the different excitation methods of a HR are outlined in §4.3, based on which different tuning strategies are proposed in §4.4. In §4.5 an assessment is made of previous research towards HRs. This forms the basis for the knowledge gap identified in §4.6 and the proposed experimental investigation. Finally, in §4.7 a note is made on the feasibility of the size of the proposed HRs in both experimental settings and typical cruise conditions.

## 4.1. Introduction of a Single Helmholtz-Resonator

The Helmholtz-Resonator is a type of resonator consisting of a thin neck and large cavity. Small induced pressure fluctuations at certain frequencies at the neck can induce a large amplitude sound response. A schematic of a cylindrical HR <sup>1</sup> is shown in Figure 5.5 with typical design parameters: neck diameter  $d_0$ , neck length  $t$  and cavity volume  $V$ , which depends on cavity length  $L$  and cavity diameter  $D$ . When the HR is embedded into a surface, the neck is typically referred to as the orifice.

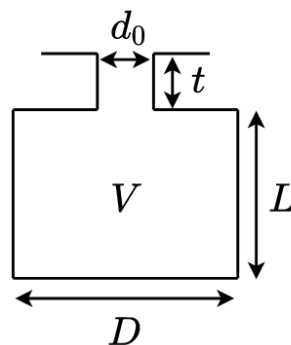


**Figure 4.1:** Schematic of a cylindrical Helmholtz-Resonator with typical design parameters

This section introduces the concept of a single HR under pure acoustic excitation. First, §4.1.1 presents the formulae for the acoustic resonance frequency of a HR, after which §4.1.2 and §4.1.3 outline the phase and gain modulation of HRs and the overtones within the HR cavity respectively.

### 4.1.1. Acoustic Resonance Frequency

Based on initial analytical derivations by Helmholtz (1860), Rayleigh (1896) derived a simplified formula for the resonance frequency of a HR that is still widely used:

$$f_0 = \frac{a_0}{2\pi} \sqrt{\frac{S}{Vt}}. \quad (4.1)$$

Here,  $a_0$  is the speed of sound and  $S$  the orifice area which is calculated as  $\pi d_0^2/4$  for cylindrical orifices. For the derivation Rayleigh (1896) assumed uniform pressure inside the cavity volume and

<sup>1</sup>The remainder of this work is confined to cylindrical HRs with cylindrical orifices unless stated otherwise

friction losses were negligible. The same result can be obtained when considering the resonator flow as a second-order mass-spring-damper system (Ghanadi, 2014), as visualised in Figure 4.2.

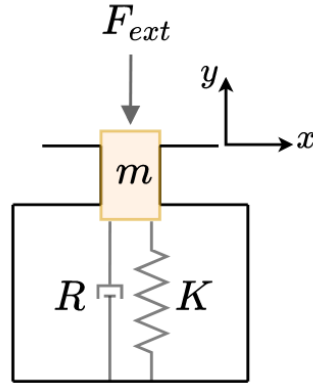


**Figure 4.2:** Helmholtz-Resonator represented as a mass-spring-damper system

Under influence of a driving force  $F_{ext}$ , the air mass  $m$  within the neck starts oscillating. In the system, compressibility effects make the cavity act as a spring with spring stiffness  $K$ . Due to friction losses and acoustic radiation the system is damped with a damping constant  $R$  (Ghanadi, 2014). The second-order differential equation for the displacement  $y$  of the air with mass  $m$  is then given by

$$m \frac{d^2 y}{dt^2} + R \frac{dy}{dt} + Ky = F_{ext}, \quad (4.2)$$

of which the natural frequency is given by

$$\omega = \sqrt{\frac{K}{m}}. \quad (4.3)$$

The air mass within the neck is given by  $m = \rho S t$ . The spring stiffness  $K = \rho a_0^2 S^2 / V$  follows from the compressibility effect following the mass  $m$  moving into the cavity (Kinsler et al., 2000). Substituting these expressions into Equation 4.3, the equation from Rayleigh (1896) in Equation 4.1 is obtained. To account for second-order effects, this equation is typically written using an end correction to the orifice depth  $t^*$  as

$$f_0 = \frac{a_0}{2\pi} \sqrt{\frac{S}{V(t + t^*)}}. \quad (4.4)$$

The end correction  $t^*$  is required, as besides the air within the neck a small portion of air inside the cavity and outside of the orifice will displace as well. For both the inside and outside of the neck an end correction component can be established,  $t_{inside}^*$  and  $t_{outside}^*$  respectively. Different end corrections can be found in literature:

1. Rayleigh (1896) proposed an end correction based on a piston that radiates into half-space. This end correction is equal for both the inside and outside and is in the range of  $\frac{\pi}{8} d_0$  and  $\frac{8}{6\pi} d_0$  per side. Here, the lower limit of the range applies to diminishing neck lengths. These end correction values consider cylindrical orifices. For arbitrary shapes of the orifice, this end correction is sometimes written as  $0.96\sqrt{S}$  for both sides together (Ingard, 1953).
2. Ingard (1953) proposed a modification to the correction of Rayleigh (1896). Rather than radiating into half-space, it was proposed that the inside end correction should reflect a piston radiating into a larger tube with diameter  $D$ . This leads to an inside end correction of  $t_{inside}^* = 0.48\sqrt{S} \left(1 - 1.25 \frac{d_0}{D}\right)$ . This approach was shown only to be valid for  $d_0/D < 0.4$ .
3. Skudrzyk (1954) proposed an end correction per side between  $0.27d_0$  and  $0.3d_0$ , based on experiments with an unflanged termination of the resonators (Urzynicok, 2003).

Based on a wave-tube analysis, Panton and Miller (1975b) showed that Equation 4.4 is only valid when the length of the cavity  $L$  is smaller than 1/16th of a wavelength  $\lambda$ . To account for longer resonator cavities, a revised formula for the resonator frequency was proposed:

$$f_0 = \frac{a_0}{2\pi} \sqrt{\frac{S}{V(t+t^*) + \frac{1}{3}L^2S}} \quad (4.5)$$

Chanaud (1994) reviews the range of applicability for the original formula from Rayleigh (1896), taking into account the propositions from Ingard (1953) and Panton and Miller (1975b). A table is presented with 1% and 5% accuracy ranges for the formula for different design parameters. However, the true end correction may vary based on parameters such as orifice geometry, cavity geometry and flow conditions. Therefore, the presented formulae and end corrections can be used to approximate the dimensions of the resonator, but the dimensions for optimal resonance should be based on experiments. Moreover, in the context of the current study, the end correction may be influenced by the grazing TBL flow. This is further discussed in §7.2.

In the design of a HR, it is still important to take into account the limitations of the used equations. The original formula from Rayleigh (1896) presented in Equation 4.4 is only valid for cavity lengths smaller than 1/16th of a wavelength. For longer cavities, the revised formula from Panton and Miller (1975b) in Equation 4.5 is required. In case the end correction from Ingard (1953) is applied, the orifice diameter and cavity diameter should be chosen such that  $d_0/D < 0.4$ .

#### 4.1.2. Phase and Gain Modulation

Whereas Equation 4.5 is meant to calculate the resonance frequency of a HR, it does not consider the changes in amplitude and phase of the pressure fluctuations inside a HR. In Figure 4.3, a typical pin-hole microphone arrangement is shown, which resembles a HR. The measured pressure  $p_p(t)$  relates to the input pressure  $p_i(t)$  through impulse transfer function  $g(t)$  (Gibeau and Ghaemi, 2021).

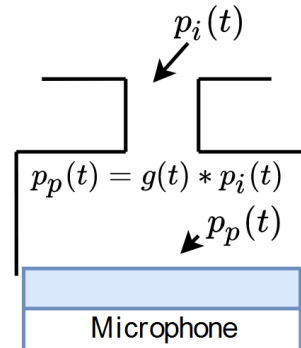


**Figure 4.3:** Typical pinhole microphone arrangement, relating measured pressure  $p_p(t)$  to input pressure  $p_i(t)$  through impulse response  $g(t)$

From the impulse transfer function  $g(t)$  the frequency transfer function  $G(f)$  is found using a discrete Fourier transform, such that  $G(f) = \mathcal{F}\{g(t)\}$ . For the frequency transfer function  $G(f)$  the amplitude  $|G(f)|$  and phase-shift  $\angle G(f)$  follow from the mass-spring-damper system as presented in Equation 4.2 (Tsuji et al., 2007):

$$|G(f)| = \left[ \left( 1 - \left( \frac{f}{f_0} \right)^2 \right)^2 + \left( \frac{2\xi f}{f_0} \right)^2 \right]^{-1/2}, \quad (4.6)$$

$$\angle G(f) = -\tan^{-1} \left[ \frac{2\xi(f/f_0)}{1 - (f/f_0)^2} \right]. \quad (4.7)$$

Here,  $\xi$  is a numerical constant that is related to the damping constant of the resonator system (Tsuji et al., 2007; Gibeau and Ghaemi, 2021). The input pressure  $p_i(t)$  can be found from the measured pressure signal  $p_p(t)$  using

$$p_i(t) = \mathcal{F}^{-1} \left\{ \frac{\mathcal{F}\{p_p(t)\}}{G(f)} \right\}. \quad (4.8)$$

In Figure 4.4, the amplitude and phase response of a pin-hole HR with design frequency  $f_0 = 2340\text{Hz}$  is plotted (Gibeau and Ghaemi, 2021). Both the result of the second-order model approximation and an experimental dynamic calibration are plotted. The amplitude response peaks around the expected resonance frequency.

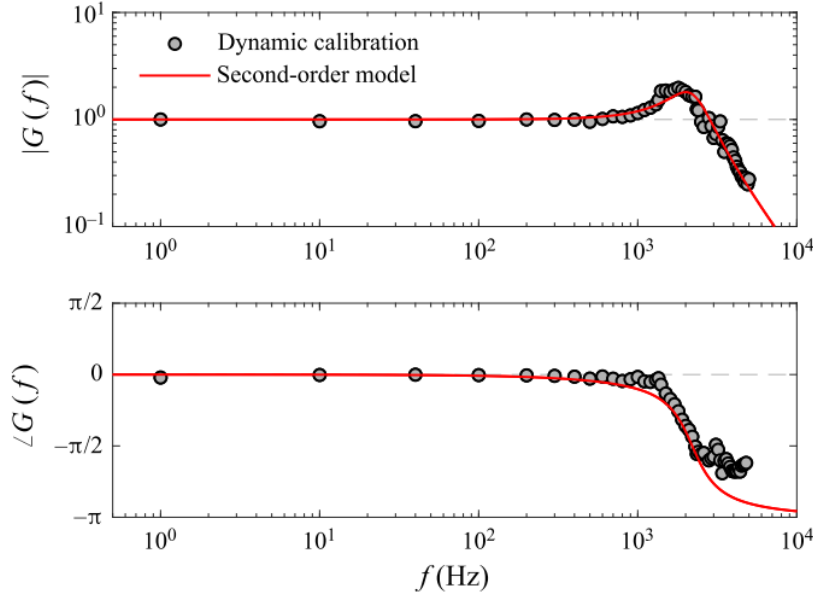


**Figure 4.4:** Amplitude and phase response of a pin-hole Helmholtz-Resonator with design frequency  $f_0 = 2340\text{Hz}$ . From Gibeau and Ghaemi (2021)

The phase response switches between frequencies below the resonance frequency and frequencies above the resonance frequency. The observed phase response may show to be an important design consideration for HRs, in case the design resonance frequency is slightly below or slightly above the frequency of the excitation pressure waves. This can be especially important when the HRs have to be tuned to purely harmonic systems – such as acoustic tones or the Tollmien-Schlichting waves in the laminar-to-turbulent transition of boundary layers (de Koning, 2021). Not much is known in this respect regarding the phase behaviour as a result of excitation using a broadband spectrum of pressure waves, as is the case for the envisioned TBL application.

### 4.1.3. Overtones

The second-order mass-spring-damper system purely considers the frequency of the Helmholtz resonance – the first mode of the system. The overtones of the HR can be found by solving the acoustic wave-tube equations (Panton and Miller, 1975b), in which the boundary conditions consist of infinite impedance at the bottom of the cavity and the reactive oscillating mass at the orifice of the HR. As schematised in Figure 4.5, two plane waves can be identified: the downward-moving plane wave  $p_-$  and upward-moving plane wave  $p_+$ .

The acoustic impedance  $Z$  in the cavity is then given by

$$Z = \frac{p_- + p_+}{U_- + U_+}, \quad (4.9)$$

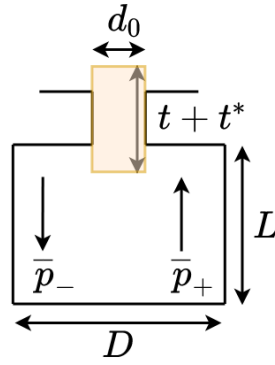


**Figure 4.5:** Helmholtz-Resonator with two plane waves for determining acoustic impedance

in which  $U_+ = p_+ / (\rho a_0 / A)$  and  $U_- = -p_- / (\rho a_0 / A)$  are the wave volume velocities, with  $A = \pi D^2 / 4$  being the cavity area (Panton and Miller, 1975b). Then using the boundary conditions, the impedance can be found. The infinite impedance at the bottom wall of the cavity results in

$$Z = i \frac{\rho a_0}{A} \cot kL, \quad (4.10)$$

with  $i = \sqrt{-1}$  the imaginary unit and  $k$  the wavenumber of the plane wave. The reactive oscillating mass has an impedance modelled by (Panton and Miller, 1975b):

$$Z = ikL \frac{a_0 \rho (t + t^*)}{LS} \quad (4.11)$$

These two expressions can then be equated as

$$\frac{(t + t^*)A}{LS} kL = \cot kL. \quad (4.12)$$

The intersections of these equations are then indicative for the wavenumbers  $k$  – and thus the frequency  $f$  – of the resonance modes of the HR. With this method, both the HR resonance frequency and the overtones can be predicted as a function of the HR geometric properties. Panton and Miller (1975b) performed this analysis on a HR with a cylindrical orifice and cylindrical cavity, similar to the HRs of the present study.

## 4.2. System of Two Adjacent Helmholtz-Resonators

The previous analysis solely considered a single HR. However, typically – and for the envisioned study – a row or array of HRs is used. Urzyncik (2003) outlines the effect of a system of HRs, which is shown in Figure 4.6.

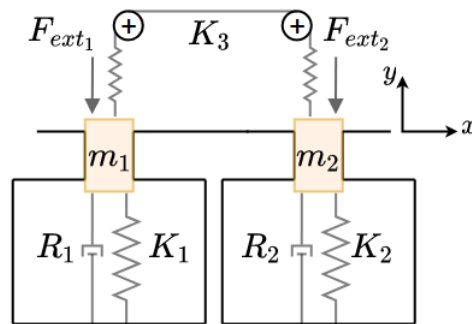


**Figure 4.6:** A system of two Helmholtz-Resonators. After Urzyncik (2003)

Following a similar analysis as in Equation 4.2, the displacement  $y_1$  and  $y_2$  of the masses  $m_1$  and  $m_2$  can be described using:

$$m_1 \frac{d^2 y_1}{dt^2} + R_1 \frac{dy_1}{dt} + K_1 y_1 = F_{ext,1}, \quad (4.13)$$

$$m_2 \frac{d^2 y_2}{dt^2} + R_2 \frac{dy_2}{dt} + K_2 y_2 = F_{ext,2}, \quad (4.14)$$

When the design of the resonators is identical, such that  $m_1 = m_2$  and  $K_1 = K_2$ , the resonating frequencies for the system become:

$$f_{0,1} = \sqrt{\frac{K_1}{m_1}} \quad (4.15)$$

$$f_{0,2} = \sqrt{\frac{K_1 + 2K_3}{m_1}} \quad (4.16)$$

While the coupling spring stiffness  $K_3$  is difficult to determine accurately, Urzyncok (2003) shows what this result means for the interaction between the HRs by analysing the eigenvectors of the system. Two options are presented. Either, both HRs oscillate at frequency  $f_{0,1}$ , which is equal to the Helmholtz frequency of a single HR. In this case, the amplitude of the oscillations is the same, but the HRs are out-of-phase diametrically. Alternatively, both HRs can oscillate at the higher frequency  $f_{0,2}$  and then the HRs are in-phase.

Experiments by Urzyncok (2003) show that the same system of two HRs under a grazing TBL can oscillate either in-phase or out-of-phase as a function of the freestream Reynolds number. When the HRs oscillated out-of-phase significantly higher sound pressure levels were obtained than when the HRs oscillated in-phase. Further analysis and experiments showed similar behaviour for systems of a larger, even number of HRs. For an odd number of HRs Urzyncok (2003) found that several oscillation modes between the resonators superimpose.

### 4.3. Excitation of a Helmholtz-Resonator

The excitation of a HR happens under influence of an external driving force  $F_{ext}$  as was shown using the mass-spring-damper-system analysis in Figure 4.2 and Equation 4.2. When excited by pressure fluctuations from a sound source, the driving force can be expressed as

$$F_{ext} = Sp e^{i\omega t}, \quad (4.17)$$

in which  $p$  is the amplitude of the incoming pressure wave (Kinsler et al., 2000). At resonance, the frequency of the incoming pressure wave  $\omega$  is equal to the resonance frequency  $f_0$ .

The excitation of a HR can occur from a pure harmonic sound source, but numerous studies have shown that a HR can also be excited by a broadband spectrum of pressure waves, such as that induced by a grazing TBL. In §2.6 it was shown that a grazing TBL flow possesses a broadband range of  $u$ -fluctuation scales. It will also be shown later that this is associated with a broadband range of scales of  $v$ -fluctuations and wall-pressure fluctuations. Two types of excitation of a HR can be distinguished, as shown in Figure 4.7. Each of the mechanisms has a different potential effect on the generation or attenuation of sound and pressure waves.

This section elaborates upon the different methods of excitation of a HR. In §4.3.1, the excitation through shear layer separation over the orifice is outlined. Subsequently, the excitation of a resonator using the wall-pressure fluctuations in the TBL is introduced. In the latter in §4.3.2, the orifice shear layer would not need to separate.

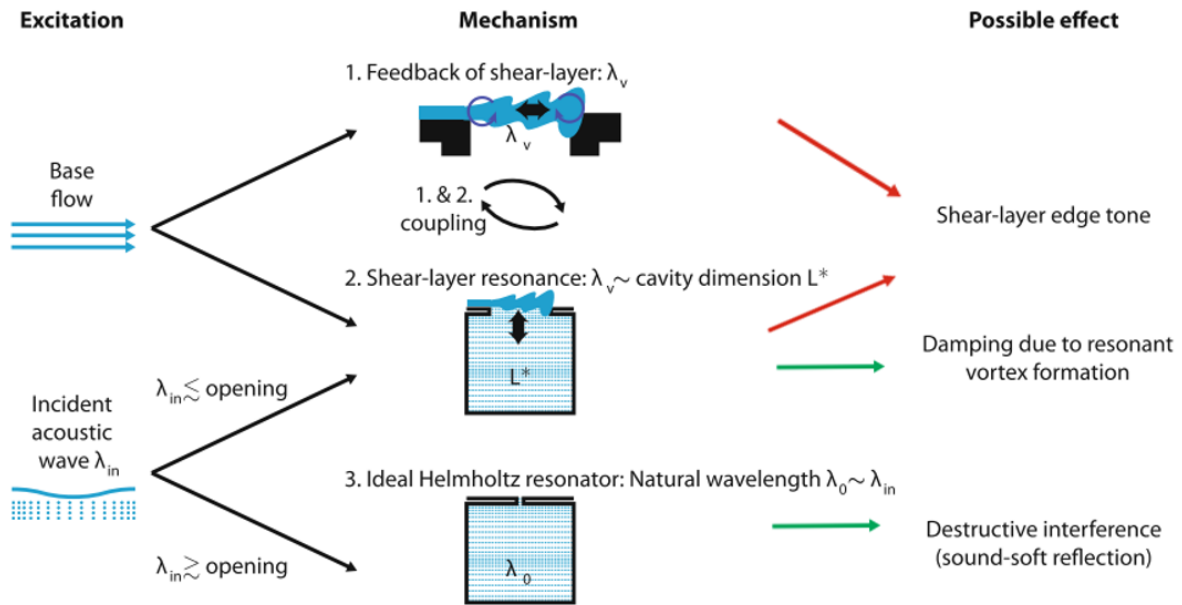


Figure 4.7: Excitation methods of a Helmholtz-Resonator with potential effects. Modified from Stein (2018)

### 4.3.1. Shear Layer Separation

The first and most studied method for excitation of a HR is through the separation of the shear layer above the orifice. Detailed numerical and experimental studies have been performed on this mechanism (Urzyncok, 2003; Ma et al., 2009; Ghanadi, 2014; Stein, 2018). These studies considered large orifice diameters, ranging from approximately 400 viscous lengths to the order of the boundary layer thickness. This is consistent with the micro-cavity array study from Silvestri et al. (2017a), who indicated diminishing skin friction benefits beyond  $d_0^+ = 145$ ; this was ascribed to the same mechanism of shear layer separation.

Figure 4.8 shows a sketch of this mechanism. As the TBL reaches the upstream edge of the orifice, it will separate into a shear layer. For the shear layer, a local Reynolds number can be defined with velocity scale  $u_\tau$  and length scale  $d_0^+$ . When the local Reynolds number remains sufficiently low, the shear layer behaves like a sheet motion. At larger Reynolds numbers, the shear layer will start rolling up into vortices similar to Kelvin-Helmholtz instabilities (Stein, 2018). When these vortices reach the downstream edge of the orifice, this creates acoustic pulses with the frequency of occurrence of these shear layer vortices. These pulses feedback upstream and then trigger the formation of the next series of vortices (Ghanadi et al., 2014b), resulting in an aero-acoustic feedback loop.

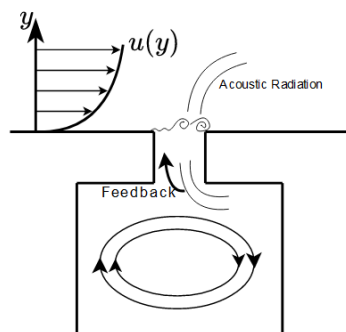
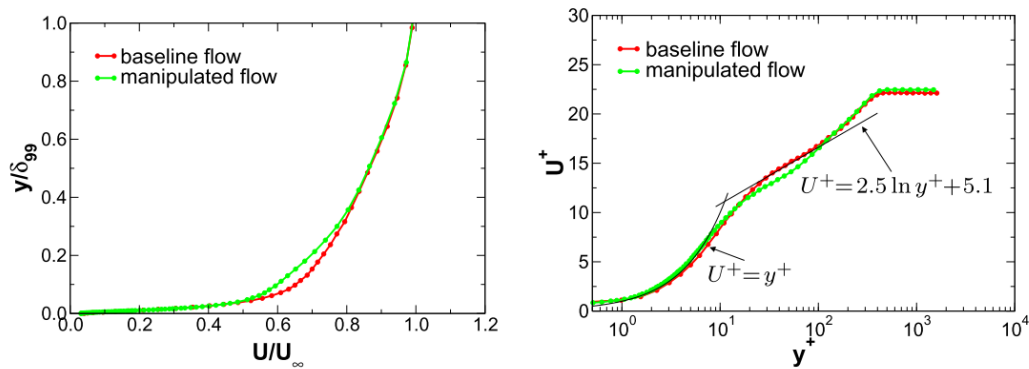


Figure 4.8: Shear layer separation over a Helmholtz-Resonator. After Ghanadi (2014)

Furthermore, these acoustic pulses can be used to excite the HR coupled to the orifice. Strong excitation (or resonance) occurs when the design resonance frequency is close to the frequency of occurrence of the Kelvin-Helmholtz instabilities in the shear layer. When this coupling occurs, a relatively small pressure fluctuation in the orifice can lead to large fluctuations in the resonator (Ghanadi et al., 2014b). This leads to a large energy transfer from turbulent energy to acoustic energy between the boundary layer flow and the cavity.

This energy transfer has been studied experimentally by Urzyncik (2003) for a zero-pressure-gradient TBL. In this study, using a HR with an orifice diameter  $d_0 \approx 0.7\delta$  a small reduction in skin friction was found. Note that due to the large form drag on such a large opening, a net drag reduction is likely not obtained. Using laser Doppler anemometry (LDA), the effect of the resonator on the boundary layer properties was examined. The results are shown in Figure 4.9. A significant momentum deficit is observed in the inner log-region, which was attributed to the aforementioned energy transfer from the boundary layer flow to acoustic energy (Urzyncik, 2003).



**Figure 4.9:** Effect of a single Helmholtz-Resonator on the mean boundary layer profile, obtained from LDA measurements  $18.65 \text{ mm}$  ( $\approx 1.35\delta$ ) downstream of the HR leading edge. From Urzyncik (2003)

In the same study, Urzyncik (2003) analysed the effect of the HR on the turbulence intensity, as shown in Figure 4.10. Both the  $u$ - and  $v$ -fluctuations increase in the log-region, but the  $u$ -fluctuations decrease directly near the wall. This was found to correspond to the slight reduction in the measured wall shear stress. The measured reduction in wall shear stress persisted for  $250 \text{ mm}$  ( $\approx 18\delta$  in this experiment) behind the single HR tested. (Urzyncik, 2003). This shows great potential for influencing the first and second-order statics of TBL flow. However, little is known about the scaling of the HR used and the effect of that on the resonance amplitude, phase and the subsequent downstream influence.

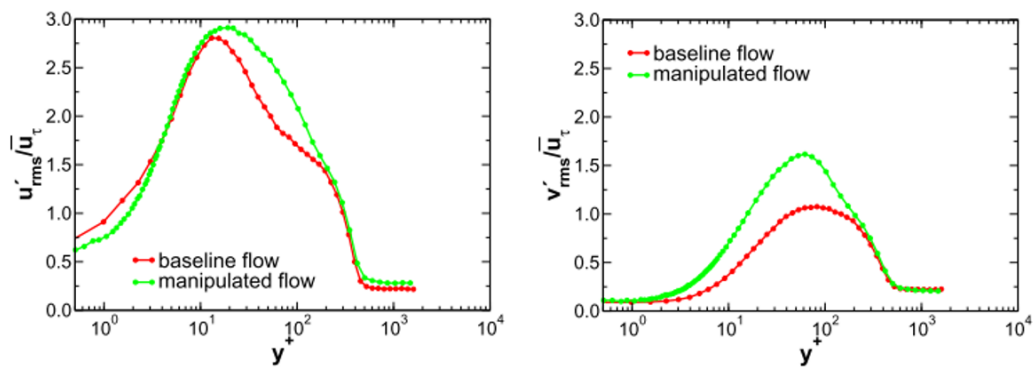


**Figure 4.10:** Effect of a single Helmholtz-Resonator on turbulence intensities, obtained from LDA measurements  $18.65 \text{ mm}$  ( $\approx 1.35\delta$ ) downstream of the HR leading edge. From Urzyncik (2003)

### 4.3.2. Turbulent Boundary Layer Wall-Pressure Fluctuations

The velocity fluctuations induced by the turbulent structures and events – especially those within the near-wall cycle – interact with the wall to create pressure fluctuations. These pressure fluctuations can then be used for the excitation of a HR, similar to the acoustic waves from a pure sound source. This would result in the third mechanism of Figure 4.7. The resonance frequency of the HR should then be matched to the frequency of the most energetic pressure fluctuations. When a pressure fluctuation near the wall of that frequency interacts with the HR, this will create large velocities in the cavity, which could lead to considerable viscous dissipation (Gad-el-Hak, 2000). This could then ideally lead to the destructive interference of the pressure fluctuations downstream of the HR (Stein, 2018).

It is hypothesised that if these pressure fluctuations are reduced in the downstream boundary layer, this would result in a reduction of turbulence intensity associated with the turbulence structures and events in the near-wall cycle. The latter is typically associated with a reduction in skin friction. Up to now, no research has been done specifically on this method of excitation of a HR under a grazing TBL, despite it being suggested by for instance Gad-el-Hak (2000).

The potential benefit of this method of excitation is that it would not necessarily require the separation of the shear layer over the orifice. With a dense array of HRs, this shear layer separation could induce coherent spanwise rollers – similar to the roughness regime reducing the skin friction benefits with larger-spaced riblets. This was also found to reduce the drag benefits of the micro-cavity array from Silvestri et al. (2017a) with increasing orifice diameters.

## 4.4. Spatial and Temporal Tuning of Helmholtz-Resonators

Based on the different methods of excitation of a HR under grazing TBL flow, various strategies for the tuning of a HR are proposed. With these strategies, it is attempted to establish a systematic approach towards studying the aero-acoustic coupling between HRs and the TBL flow. In each design strategy, spatial tuning and temporal tuning can be distinguished. Spatial tuning refers to sizing the orifice of the resonator with respect to the size of boundary layer flow structures. Temporal tuning involves matching the resonance frequency to the frequency of the most energetic fluctuations of structures and events within the TBL. In Figure 4.11, the pre-multiplied energy spectra for the  $u$ -,  $v$ - and pressure fluctuations are shown as a function of streamwise inner-scaled wavelength  $\lambda_x^+$ . The most energetic  $u$ -fluctuations occur at  $\lambda_x^+ \approx 1000$ , whereas the most energetic  $v$ - and wall-pressure fluctuations coincide at a wavelength of  $\lambda_x^+ \approx 250$ . Three different strategies involving combined spatial and temporal tuning are outlined in this section.

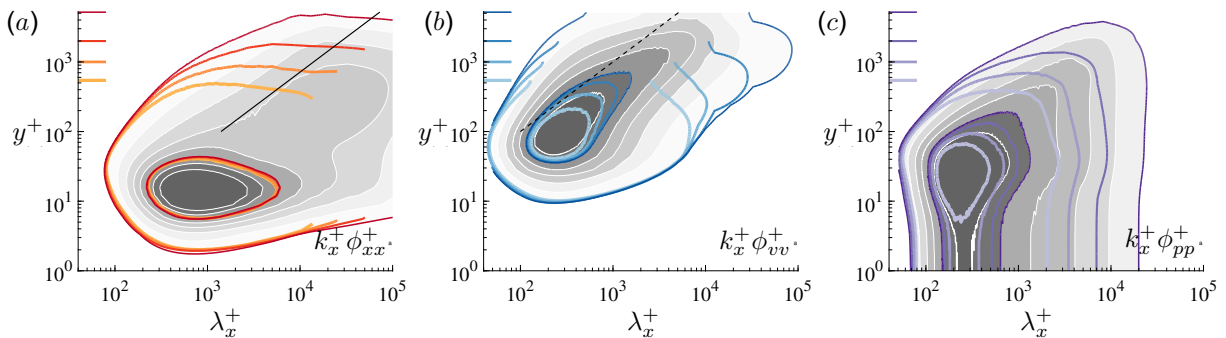


**Figure 4.11:** Pre-multiplied 1D energy spectra of (a)  $u$ -fluctuations, (b)  $v$ -fluctuations and (c) pressure fluctuations. Increased colour intensity contours indicate increasing Reynolds number. After Lee and Moser (2015) and Panton et al. (2017)

### 4.4.1. Strategy 1: Spatial and Temporal Tuning towards Most Energetic $u$ -Fluctuations

The first strategy towards tuning a HR follows the excitation method of shear layer separation to induce an energy transfer from turbulent to acoustic energy. To achieve this, the first strategy consists of both spatial and temporal tuning focused towards the most energetic  $u$ -fluctuations. In this strategy, the orifice size is such that half a wavelength of the  $u$ -fluctuations is captured over the orifice.

The design wavelength corresponds to  $\lambda_x^+ = 1000$ , leading to an orifice diameter of  $d^+ = 500$ . The frequency of occurrence of the most energetic  $u$ -fluctuations directly follows from the wavelength and the convection velocity  $U_c$ . Here,  $U_C^+ = 11$  is chosen following the discussion in §2.6. This would lead to an inner-scaled frequency of  $f_0^+ = 0.011$ . The temporal tuning is then such that this frequency is matched by the resonance frequency of the HR. The first design strategy is visualised in Figure 4.12.

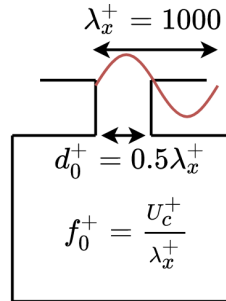


Figure 4.12: Tuning Strategy 1, with  $d_0^+ = 500$  and  $\lambda_x^+ = 1000$

#### 4.4.2. Strategy 2: Spatial Tuning towards Attenuating Sweep Events, Temporal Tuning towards Most Energetic $u$ -Fluctuations

The second strategy aims to split the spatial and temporal tuning of a HR. In the study towards the micro-cavity array from Silvestri et al. (2017a), it was found that an orifice diameter of  $d_0^+ = 60$  is the most efficient for attenuating sweep events. Therefore, in this strategy, this would become the orifice size. For the temporal tuning, again the most energetic  $u$ -fluctuations are chosen, such that  $\lambda_x^+ = 1000$  and  $f_0^+ = 0.011$ . This strategy is visualised in Figure 4.13.

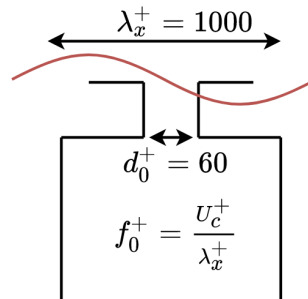


Figure 4.13: Tuning Strategy 2, with  $d_0^+ = 60$  and  $\lambda_x^+ = 1000$

This strategy aims to assess whether it is possible to excite a HR through shear layer interaction while limiting the shear layer separation. Essentially, this revisits the backing cavity study from Silvestri et al. (2017b). Similar levels of turbulence intensity reduction found were found with individual backing cavities as with a common backing cavity, despite the individual cavities reducing the cavity volume considerably. The backing cavity volume was considered the main parameter in that study. However, in this study, no details considering temporal tuning of the backing cavities were outlined. This strategy then aims to assess whether temporal tuning to the most energetic  $u$ -fluctuations could lead to a further improvement in reducing turbulence intensity.

#### 4.4.3. Strategy 3: Spatial Tuning towards Attenuating Sweep Events, Temporal Tuning towards Most Energetic $v$ -/Pressure Fluctuations

The third strategy is aimed at using the wall-pressure fluctuations of the TBL for the excitation of a HR to achieve destructive interference of these pressure fluctuations. The temporal tuning is now chosen

to be biased towards the most energetic  $v$ - and wall-pressure fluctuations, which coincide at  $\lambda_x^+ \approx 250$ . This leads to an inner-scaled frequency of  $f_0^+ = 0.044$ . This strategy is similar to the second strategy in terms of spatial tuning of the orifice of the HR. To achieve maximum sweep attenuation, the orifice diameter is chosen to be  $d_0^+ = 60$ . The third design strategy is visualised in Figure 4.14.

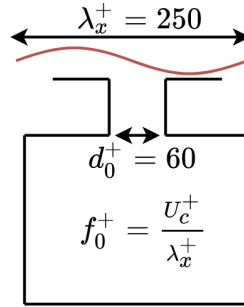


**Figure 4.14:** Tuning Strategy 3, with  $d_0^+ = 60$  and  $\lambda_x^+ = 250$

With this combination of spatial and temporal tuning, it is sought to amplify the sweep attenuation mechanism of the micro-cavity array from Silvestri et al. (2017a). The destructive interference of wall-pressure fluctuations intended with the proposed temporal tuning is hypothesised to lead to further damping of the wall-normal velocity fluctuations, which were shown to be key in attenuating the sweep events with the micro-cavity array (Bhat et al., 2021).

#### 4.4.4. Design Considerations for Arrays of Helmholtz-Resonators

The three proposed spatial and temporal tuning strategies apply to a single HR. For practical application – on for instance an aircraft fuselage – likely a dense array of HRs needs to be applied. This then also leads to the question of how to space the HRs most effectively in both the streamwise and spanwise directions.

Two potential strategies for the streamwise spacing can be distinguished. The first strategy would be to place a downstream HR once the effect of the HR directly upstream starts to reduce. For instance, Urzunicok (2003) found the effect of the tested HR to persist  $250mm$  downstream. This would then dictate a streamwise spacing of  $250mm$ . This strategy would lead the smallest number of overall HRs, limiting the induced pressure-drag aspect that is inherently present.

The alternative strategy would be to space the HRs to establish interaction between them, as outlined in section 4.2. Potentially, this could enhance the effects as compared to a single HR. However, no existing research is found that simultaneously describes this interaction and assesses the effect on the boundary layer properties. Therefore, further research would be required.

For the ideal spanwise spacing of HRs, little is found in existing research. Research towards riblets has shown that spanwise spacing can have a considerable effect on the amount of drag reduction achieved. Quantifying this effect for HRs would require dedicated parameter studies.

### 4.5. Assessment and Characterisation of Existing Studies towards Helmholtz-Resonators under a Grazing Turbulent Boundary Layer

With the different design strategies and considerations established, the various existing studies and findings can be put into perspective. An overview of the existing studies with the main parameters used can be found in Table 4.1. Only the studies that have investigated the effect of HRs on TBL flow have been included. Typically, past research involved relatively large orifice diameters, most resembling design strategy 1 from §4.4.1. However, often no reasoning for the temporal tuning of the resonators is provided, making the assessment of results difficult.

Study	$U_\tau$	$Re$	$d_0$	$f_0$	Obtained Result
Panton and Miller (1975a)	$1.2 \text{ m/s}^a$	$Re_\tau = 1600^b$	$400l^* - 800l^{*b}$	$0.0026t^* - 0.0104t^{*b}$	"Strong excitation" when turbulent eddies are twice the orifice diameter and impose a frequency equal to resonance frequency of resonator.
Eider (1978)	Unknown	Unknown	$0.45 \text{ cm} - 3.45 \text{ cm}^a$	$278 Hz - 1343 Hz^a$	Resonant oscillation when streamwise slot with is 1/4th of disturbance wavelength
Panton et al. (1987)	$1 \text{ m/s}^b$	$Re_\tau = 2000^b$	$687l^{*b}$	$0.0087t^{*b}$	1. Strongest excitation when $f_0 d_0 / U_e = 0.23$ . 2. Decrease in momentum near the wall with increased streamwise turbulence intensity
Flynn et al. (1989, 1990)	$1.0 \text{ m/s}^a$	$Re_\tau = 1866^b$	$687l^{*b}$	$0.0086l^{*b}$	Large increase in turbulent fluctuations with row of 10 resonators
Urzynicok (2003)	Unknown	Unknown	$0.68\delta$	Unknown	Small reduction in skin friction on a zero-pressure-gradient TBL
Ghanadi (2014)	$0.78 \text{ m/s} - 1.12 \text{ m/s}^a$	$Re_\tau = 800 - 2000^a$	$250l^* - 1600l^{*b}$	$0.005t^* - 0.0184t^{*b}$	Reduction in turbulence intensity when orifice diameter approached thickness of the inner layer of the TBL
Silvestri et al. (2018)	$0.24 \text{ m/s} - 0.375 \text{ m/s}^a$	$Re_\theta = 2393 - 3771^a$	$60l^{*a}$	Unknown	Similar reduction in turbulence intensity with individual backing cavities and shared backing cavity.

**Table 4.1:** Overview of past studies towards flow-excited Helmholtz-Resonators. Where possible, diameter and frequency are converted to inner-scaled variables. <sup>a</sup>As mentioned in study paper. <sup>b</sup>Calculated using parameters mentioned in study paper

One of the HRs flight-tested by Panton and Miller (1975a), is close to the parameters proposed in design strategy 1, with  $d_0^+ = 600$  and  $f_0^+ = 0.0104$ . This was also the HR that gave the largest amplitude response, which was referred to as "strong excitation".

In further research on the effect of similarly sized HRs on TBLs, Panton et al. (1987) and Flynn et al. (1989, 1990) found a decrease in momentum from the near-wall log-region to the beginning of the wake region, as well as increased velocity fluctuations in these regions. Based on this the conclusion was drawn that the HRs "suck" (Flynn et al., 1989). However, while Urzynicok (2003) found the same effects in the log-region, near-wall measurements ( $y^+ < 7$ ) showed a reduction in velocity fluctuations in the viscous sublayer. Consequently, a small reduction in skin friction was found. No sizing considerations of the HR with respect to the TBL scales are found from Urzynicok (2003) – except the relatively large orifice size of  $d_0 = 0.68\delta$  – making a direct comparison to the research by Flynn et al. (1989) difficult.

The studies of Ghanadi (2014) and Silvestri et al. (2018) are the first to explore HRs of smaller diameters. Ghanadi (2014) found a reduction in turbulence intensity when the orifice diameter approached the thickness of the inner layer of the TBL at approximately 300 viscous units. However, no reasoning for the temporal scaling was provided and it is difficult to find which combination of size and frequency was responsible for the reduction in turbulence intensity. In the research from Silvestri et al. (2018), the individual backing cavities were not necessarily designed to function as HRs and as such, no temporal tuning has been done.

Interestingly, the studies by Silvestri et al. (2018) and Urzynicok (2003) both suggest a reduction in skin friction through apparently completely different mechanisms and through different surrogate metrics. For the micro-cavity array of Silvestri et al. (2018), Bhat et al. (2021) have shown through DNS simulation that damping of the wall-normal velocity fluctuations is achieved with a reduction in turbulence intensity in the buffer and inner log-region. For the HR used by Urzynicok (2003), an increase in turbulence intensity was found in these regions. This was then accompanied by a reduction in turbulence intensity in the viscous sublayer. The latter was then responsible for the measured local reduction in skin friction.

This seems to indicate different mechanisms play a role in reducing skin friction, resembling the different excitation methods of HRs categorised by Stein (2018) in Figure 4.7. The HR used by Urzynicok (2003) had a large orifice with respect to the boundary layer thickness, from which the excitation through shear layer separation can be expected. The reduction in skin friction would then be through the energy transfer from turbulent to acoustic energy. The arrays used by Silvestri et al. (2018) involved significantly smaller orifice diameters. Here, the shear layer separation would not be present and the formation of Kelvin-Helmholtz instabilities is not expected. The reduction of skin friction here is then more likely a result of destructive interference of the incoming pressure fluctuations.

#### **4.6. Knowledge Gap in Research towards Helmholtz-Resonators under Turbulent Boundary Layer**

Based on the proposed strategies for combined spatial and temporal tuning of HRs and the assessment of existing research, a clear knowledge gap can be identified.

None of the existing research has considered the temporal tuning of the HRs to the most energetic velocity fluctuations and pressure fluctuations within the TBL. Furthermore, all studies except that from Silvestri et al. (2018) – where the backing cavities were not specifically aimed to behave as HRs – consider large orifice sizes like those proposed in design strategy 1, in which shear layer separation is responsible for acoustic excitation. Even though there are signs that this could give small benefits in terms of skin friction (Urzynicok, 2003; Ghanadi, 2014), it can be reasoned that the shear layer separation and the consequent formation of Kelvin-Helmholtz instabilities reduce the drag-reduction potential.

HRs with spatial tuning according to design strategies 2 and 3 ( $d_0^+ \approx 60$ ) have not yet been researched at all. Furthermore, temporal tuning of HRs or acoustic liners using the wall-normal pressure fluctuations has not yet been researched.

Therefore, experimental research is proposed towards HRs with the spatial and temporal tuning from design strategies 2 and 3. Both have an approximate orifice diameter of  $d_0^+ = 60$  and are tuned to have an inner-scaled resonance frequency of  $f_0^+ = 0.011$  and  $f_0^+ = 0.044$ , corresponding to the frequency of the most energetic  $u$ - and  $v$ -wall-pressure fluctuations of the near-wall cycle respectively. This should show whether these have potential for reducing the mean turbulent skin friction by manipulating the near-wall flow dynamics.

#### 4.7. Full-Scale Applicability of Proposed Tuning Strategies

For a flow control method to be considered realisable, realistic dimensions should be obtained for both experimental and full-size settings. Table 4.2 shows rough HR sizing estimates following the different design strategies and using Equation 4.5. All three design strategies lead to realistic values for experimental testing in the order of millimetres. The estimates lead to designs that are feasible to produce using rapid-prototyping methods.

Tuning Strategy	Typical Wind Tunnel Conditions ( $U_e = 15 \text{ m/s}$ , $U_\tau = 0.54 \text{ m/s}$ $a_0 = 343 \text{ m/s}$ , $\nu = 1.5 \cdot 10^{-5} \text{ m}^2/\text{s}$ )	Typical Cruise Conditions ( $U_e = 250 \text{ m/s}$ , $U_\tau = 7.1 \text{ m/s}$ $a_0 = 295 \text{ m/s}$ , $\nu = 3.5 \cdot 10^{-5} \text{ m}^2/\text{s}$ )
1) $d_0^+ = 500$ , $\lambda_x^+ = 1000$	$r_0 = 7 \text{ mm}$ $R = 43 \text{ mm}$ $L = 78 \text{ mm}$	$r_0 = 1.2 \text{ mm}$ $R = 3 \text{ mm}$ $L = 0.5 \text{ mm}$
2) $d_0^+ = 60$ , $\lambda_x^+ = 1000$	$r_0 = 0.833 \text{ mm}$ $R = 11.6 \text{ mm}$ $L = 50 \text{ mm}$	$r_0 = 0.147 \text{ mm}$ $R = 0.665 \text{ mm}$ $L = 1.11 \text{ mm}$
3) $d_0^+ = 60$ , $\lambda_x^+ = 250$	$r_0 = 0.833 \text{ mm}$ $R = 5.3 \text{ mm}$ $L = 26 \text{ mm}$	$r_0 = 0.147 \text{ mm}$ $R = 0.36 \text{ mm}$ $L = 0.25 \text{ mm}$

**Table 4.2:** Rough design parameter estimates for proposed Helmholtz-Resonators in wind tunnel conditions and for a fuselage in typical cruise conditions. Cruise conditions adopted from Modesti et al. (2021)

In typical cruise conditions, applying the HRs to an aircraft fuselage would result in dimensions that are below or in the order of a millimetre. This is in the order of magnitude of the skin thickness of a fuselage. Whereas this does not yet consider the effects on stress concentrations, the size of the proposed HRs initially seems feasible.

# Experimental Setup and Methodology

The previous chapters have shown the reasoning for an experimental study towards the use of HRs, tuned towards the near-wall cycle turbulence structures and events, as a passive flow control method. This chapter presents the experimental setup in §5.1 and the design of the proposed HRs in §5.2. Subsequently, the available measurement techniques are outlined in §5.3.

## 5.1. Wind Tunnel Setup

The available setup consists of two test sections to be used downstream of the 600 mm x 600 mm contraction of the W-Tunnel at the TU-Delft. The test sections are shown in Figure 5.1. In total, the floor of the test sections forms a flat plate with a total length of 3750 mm. The ceiling of both sections is adjustable to vary the streamwise pressure gradient  $dp/dx$ . The pressure gradient can be measured using two rows of pressure taps, which are located symmetrically off-centre.

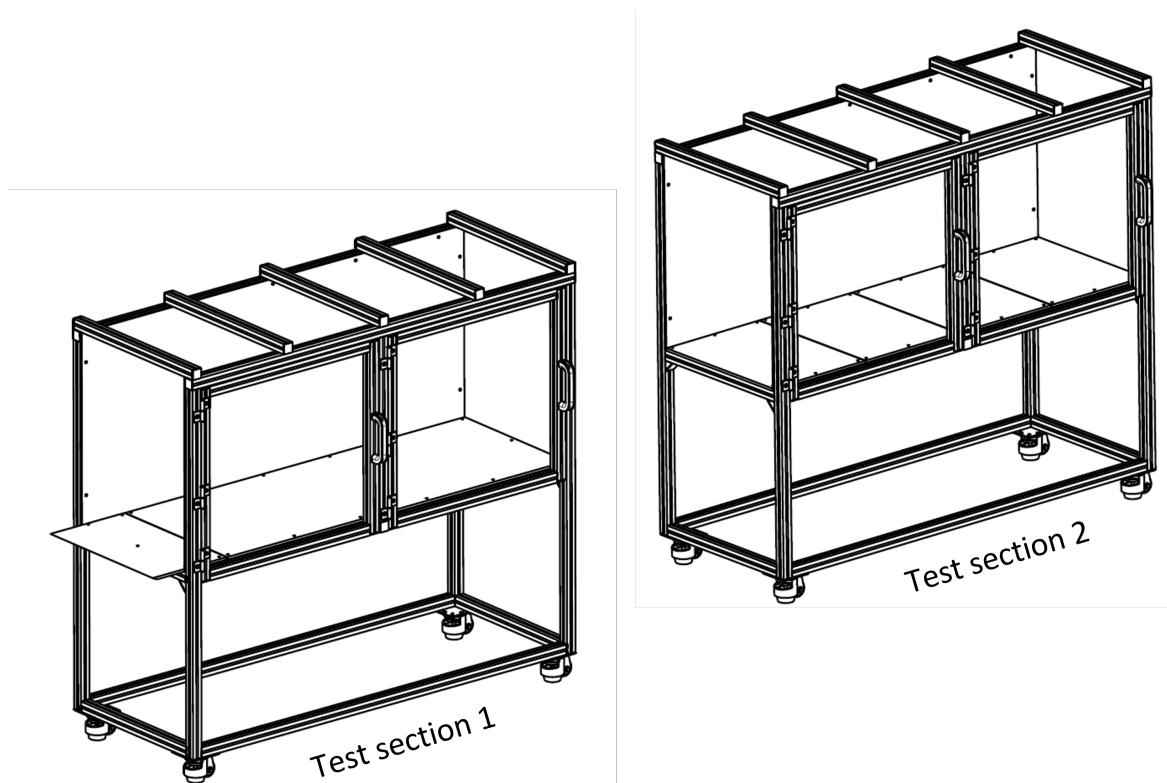


Figure 5.1: Test sections of the wind tunnel setup. From Baars (2021)

Figure 5.2 and Figure 5.3 show schematics of the top view and side view of the combined test sections, as well as the adopted coordinate system. Sandpaper is applied to the circumference of the upstream 150 mm of the first test section to trip the boundary layer to a turbulent state. The second test section has four interchangeable floor plates of 600 mm x 450 mm, to allow for testing surface treatments such

as the proposed HRs. The sides of the test sections have doors to access the interchangeable plates. For the current test, it is chosen to use the third interchangeable plate – between  $x = 2850 \text{ mm}$  and  $x = 3300 \text{ mm}$ . This allows the TBL to have sufficiently developed without it being affected significantly by the open exit of the test sections. To take into account the displacement thickness of the boundary layer, the ceiling is adjusted such that over the full length of the plate zero pressure gradient is achieved.

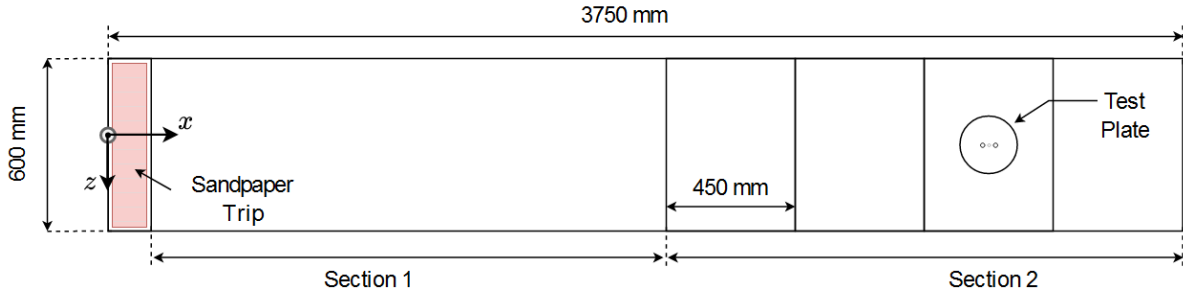


Figure 5.2: Schematic top view of the test setup

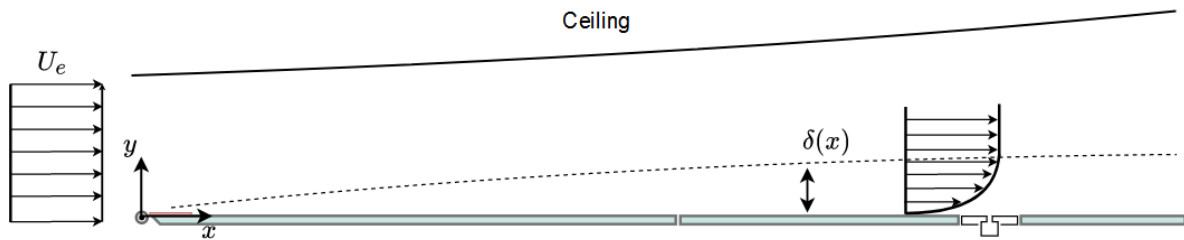


Figure 5.3: Schematic side view of the test setup. Dimensions not to scale for illustrative purposes

In the W-Tunnel, free-stream velocities from  $U_e = 3 \text{ m/s}$  to  $U_e = 15 \text{ m/s}$  can be reached. With the available setup, this corresponds to a friction velocity of up to  $u_\tau = 0.54 \text{ m/s}$  and a friction Reynolds number of up to  $Re_\tau \approx 2200$  (Dacome and Baars, 2021). This Reynolds number is comparable to previous experimental tests of HRs and other flow control methods.

## 5.2. Experimental Design

A 'plug-in-plate'-style modular setup is designed in the third plate of the second test section to allow to quickly interchange between different HR geometries, as indicated in Figure 5.2. Two different HR setups are used: a setup with a single HR, as well as a setup with an array of HRs. Schematics of the top plates for each of the setups are shown in Figure 5.4. In principle, the single HR could have been formed by taping off all but one HR in the array setup. However, it was considered that having the incoming TBL develop over a tape on an orifice might not be ideal. Therefore, it was preferred to design a separate setup with a single HR in an attempt to get the highest measurement accuracy.

To achieve the largest Reynolds Number  $Re_\tau$ , it is chosen to focus to fix the freestream velocity to the maximum achievable  $U_e = 15 \text{ m/s}$ . An overview of the conditions and the main TBL scaling parameters is presented in Table 5.1. These parameters then dictate the physical dimensions for the tested HRs.

Wind tunnel velocity $U_e$	$15 \text{ m/s}$
Friction velocity $u_\tau$	$0.54 \text{ m/s}$
Reynolds number $Re_\tau$	2200
Viscous length scale $l^*$	$2.8 \cdot 10^{-3} \text{ m}$
Viscous time scale $t^*$	$5.1 \cdot 10^{-5} \text{ s}$

Table 5.1: Overview of experimental conditions used for the design of the experimental setup

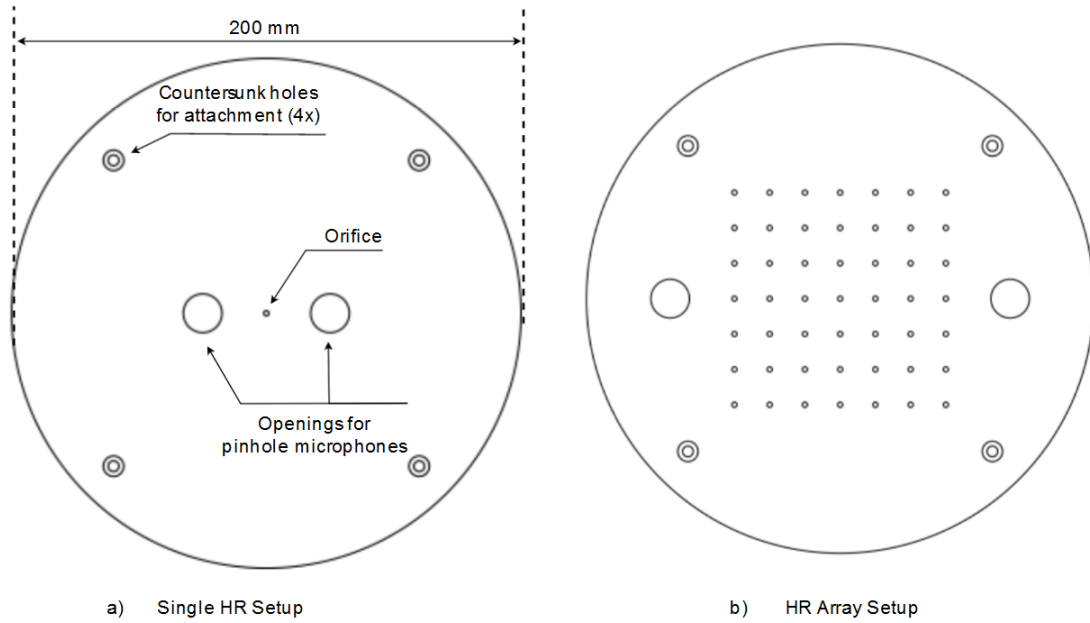


Figure 5.4: Top views of a) single HR setup and b) HR array setup

This section elaborates on the design parameters and considerations for the two setups of HRs. First, in §5.2.1, the reasoning behind the chosen HR design strategy is explained. Subsequently, §5.2.2 outlines each of the HR design parameters.

### 5.2.1. Chosen Design Strategy

The three strategies for combined spatial and temporal tuning of HRs – as identified in §4.4 – are summarised in Table 5.2. For this experimental campaign, it was decided to focus on one strategy only to limit the scope. With the main consideration of reducing skin friction drag, design strategies 2 and 3 were thought to be preferred over design strategy 1 because of their smaller orifice sizes. The choice between design strategies 2 and 3 is dictated by the setup.

Strategy	Spatial Tuning	Temporal tuning	Orifice diameter $d_0^+$	Wavelength $\lambda_x^+$
1	$u$ - fluctuations	$u$ -fluctuations	$\approx 500$	$\approx 1000$
2	Attenuation of sweep events	$u$ -fluctuations	$\approx 60$	$\approx 1000$
3	Attenuation of sweep events	$v$ -fluctuations / wall-pressure fluctuations	$\approx 60$	$\approx 250$

Table 5.2: Summary of various proposed design strategies

A design wavelength of  $\lambda_x^+ = 1000$  corresponds to a design resonance frequency of  $f_0 = 200 \text{ Hz}$  for design strategy 2 at the experimental conditions. It was found that this frequency coincides with the blade-passing frequency of the wind tunnel fan. Therefore, it would be hard to distinguish the effects of the tested HRs from the wind tunnel noise. For this reason, it is chosen to focus on design strategy 3 for this experimental campaign.

### 5.2.2. Design Parameters for Helmholtz-Resonators

With the experimental conditions and design strategy established, the actual design parameters for the tested HRs can be determined. This subsection elaborates on the choice of design parameters, as well as the range for each of the parameters to be considered.

### Tested Resonance Frequencies

The wavelength of the most energetic  $v$ -fluctuations is at  $\lambda_x^+ = 250$ , which corresponds to a frequency of  $f_0 \approx 850 \text{ Hz}$  at the experimental conditions. This is taken as the nominal design resonance frequency. Based on the considerations in section 4.1 on the phase and amplitude response of a HR, additional design frequencies are tested. From Equation 4.7 it can be deduced that at the resonance frequency, the HR induces a phase shift of  $-\pi/2 \text{ rad}$ . For frequencies below the resonance frequencies, the HR does not induce a phase shift. For frequencies higher than the resonance frequency, a phase shift of  $-\pi \text{ rad}$  is induced.

The additional tested design frequencies are referred to as subresonance (a lower design resonance frequency) and superresonance (a higher design resonance frequency) and aim to test this effect of the phase differences between the HRs and the incoming flow. For subresonance, the design wavelength is chosen to be 50% higher than the most energetic wavelength, such that  $\lambda_x^+ = 375$ . This corresponds to a design resonance frequency of  $f_0 \approx 600 \text{ Hz}$ . At this frequency, the HR is expected to induce a phase switch at the frequency of the most energetic  $v$ -fluctuations of the incoming flow. With superresonance, the design wavelength is 50% lower than the most energetic wavelength, resulting in a design frequency of  $f_0 \approx 1400 \text{ Hz}$ . At this frequency, there is no induced phase switch expected between the HR and the incoming flow.

Resonance	Wavelength $\lambda_x^+$	Design resonance frequency $f_0$ [Hz]	Expected phase shift [rad]
Nominal resonance	250	850	$-\pi/2$
Subresonance	375	600	$-\pi$
Superresonance	125	1400	0

**Table 5.3:** Summary of chosen design resonance frequencies at the experimental conditions

### Tested Orifice Diameters and Neck Lengths

The spatial tuning of design strategy 3 is based on the micro-cavity array study from Silvestri et al. (2017a). It was found that the most efficient attenuation of sweep events occurred at an inner-scaled orifice diameter of  $d_0^+ \approx 60$ . This leads to an orifice diameter of  $d_0 = 1.806 \text{ mm}$  at the test conditions. For manufacturing purposes an orifice diameter of  $d_0 = 2 \text{ mm}$  was adopted, corresponding to  $d_0^+ = 72$ . The ratio between neck length and orifice diameter was chosen to be 2, such that the neck length of the orifice becomes  $t = 4 \text{ mm}$ .

As the studies from Silvestri et al. (2017a) indicate a large variation in effectiveness depending on the orifice diameter, two additional orifice diameters are considered for the test:  $d_0 = 1 \text{ mm}$  ( $d_0^+ = 36$ ) and  $d_0 = 3 \text{ mm}$  ( $d_0^+ = 108$ ). While these orifice diameters are expected to be less effective in attenuating sweep events, they should show the different flow mechanisms as described by Silvestri et al. (2017b). At  $d_0^+ = 36$ , the orifice diameter is expected to capture fewer sweep events due to it being too small with respect to the size of the structures that it tries to influence. At  $d_0^+ = 108$ , shear layer separation is expected to start playing a role, with reduced effectiveness as a result.

For manufacturing reasons, all resonators have the same neck length. This way, all orifices can be milled out of the same plate of  $4 \text{ mm}$  thickness. This comes with the downside that the ratio between neck length and orifice diameter is different for each orifice diameter. This downside was deemed acceptable based on the findings by Silvestri et al. (2017a) that the neck length had a negligible effect on the effectiveness of the array. However, after finalising the designs for the experimental campaign, a new paper was published indicating a larger sensitivity to the neck length (Severino et al., 2022). Based on the findings of the new study, this design choice should potentially be re-evaluated for future studies.

The chosen orifice diameters and neck lengths are summarised in Table 5.4.

Orifice diameter $d_0^+$	Orifice diameter $d_0$ [mm]	Neck length $t$ [mm]	$t/d$
36	1	4	4
72	2	4	2
108	3	4	4/3

**Table 5.4:** Summary of chosen orifice diameters and neck lengths at the experimental conditions

### Spacing between HRs, HR Cavity Diameter and Cavity Length

The chosen HR cavity diameter  $D$  follows from the desired spacing of HRs in the HR array setup. The spacing is chosen to be  $500l^*$  – corresponding to  $13.9\text{ mm}$ . This value is based on streamwise extent of the low-speed streaks – with which interference is sought – of approximately  $1000l^*$ . With a spacing of  $500l^*$ , it is then sought to create an interaction between subsequent HRs as they interact with the same low-speed streak. In total, an array of  $7 \times 7$  HRs is fitted on the test plate. By taping off specific orifices, the streamwise and spanwise spacing can be varied. This means the possible values of spacing between HRs can vary between  $500l^*$  and  $3000l^*$ . The HR cavity diameter is chosen to be  $D = 11\text{ mm}$ . This way, there is  $2.9\text{ mm}$  of material between resonators in the array to design a mechanical assembly.

For all tested HRs, the cavity diameter  $D$  stays the same. As the resonance frequency is primarily a function of the HR cavity volume, the resonance frequency can then be controlled by changing the cavity length  $L$ . In Figure 5.5, a side view of a row of 7 HRs designed for nominal resonance is shown, with orifice diameter  $d_0^+ = 72$ .

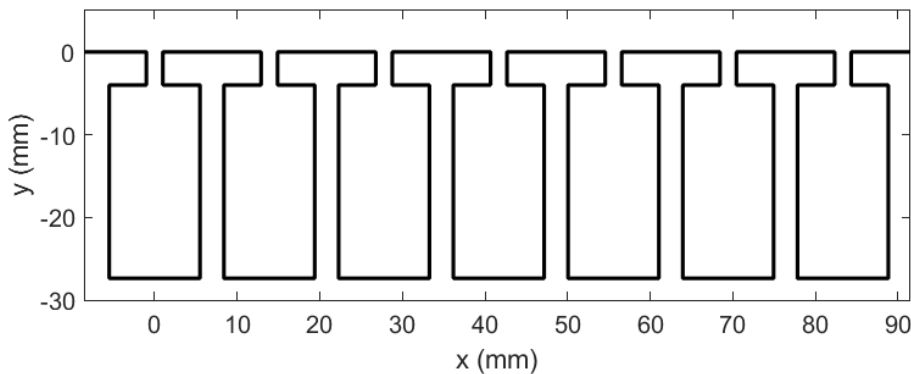


**Figure 5.5:** Side view of a row of 7 HRs for  $d^+ = 72$  at nominal resonance

### Assembly/Mechanical Considerations

With the main HR design parameters set up, it is important to design an assembly that allows for quick interchanging between the different HRs. Both the single HR setup and the HR array setup have their own assembly. Figure 5.6a shows the sideview of the HR array setup, with the different components indicated. From the mounting plate the HR array assembly is bolted to the test section from underneath. The mounting plate is fitted with set screws to allow for small adjustments to make sure the top plate is flush with the remainder of the test plates.

As previously mentioned, changing between the different orifice diameters can be done by interchanging top plates. These are constructed such that they are mounted independently to the rest of the assembly.

To control the resonance frequency for each of the top plates, only the cavity length is varied. For the HR array setup, this is done using  $8\text{ mm}$  thick stack plates. One of these stack plates is shown in Figure 5.6b. This way, the cavity length can be varied in steps of  $8\text{ mm}$ . Figure 5.6a shows an example of the HR array setup with 4 stack plates mounted. Together with the mounting plate and the plate directly underneath the top plate – which are also both  $8\text{ mm}$  thick – a cavity length of  $L = 48\text{ mm}$  is achieved. With the bottom plate, the HRs are closed, except for one row of HRs in which microphones can be placed. These microphones then form the bottom of the remaining HRs.

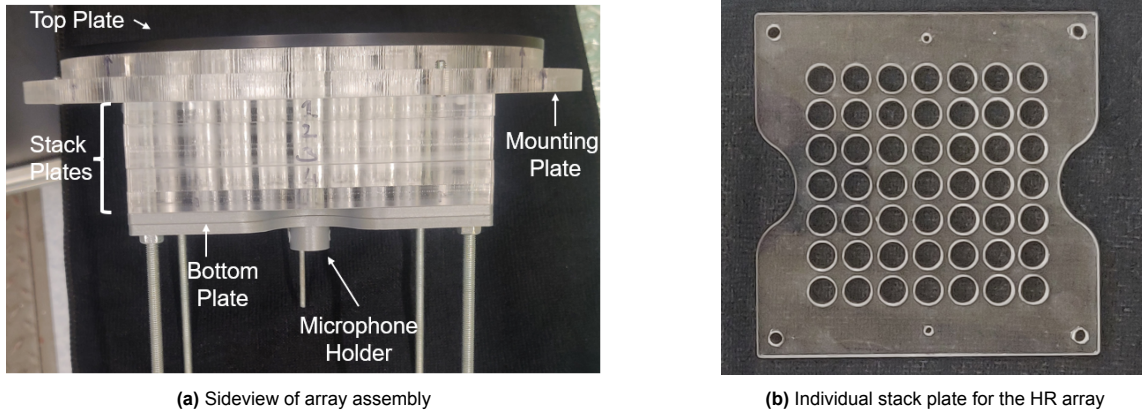


Figure 5.6: HR array assembly

The single HR setup is slightly simpler in design. The top plate and mounting plate construction are similar to that of the HR array setup, but the cavity is now formed by a single plexiglass tube of 11 mm inner diameter. The bottom of the cavity is closed by inserting a microphone. The cavity length is then varied by re-positioning the microphone.

More detailed schematics of both the single HR setup and the HR array setup are presented in Appendix A.

#### Final Test Design Parameters

In Table 5.5, a final overview is presented of the different HRs that can be tested in the experimental campaign. In total, 9 different HR geometries can be tested to give an insight into the sensitivity to what are expected to be the critical design parameters.

$d_0$ [mm]	$d_0^+$	Resonance	$L$ [mm]	$f_0$ [Hz]	$\lambda_x^+$
1	36	Subresonance	16	560	380
		Nominal resonance	8	797	265
		Superresonance	2	1580	135
2	72	Subresonance	48	581	370
		Nominal resonance	24	843	252
		Superresonance	8	1485	145
3	108	Subresonance	80	585	365
		Nominal resonance	48	794	264
		Superresonance	16	1454	147

**Table 5.5:** Overview of possible HRs available to test during the experimental campaign at the experimental conditions. All listed HRs can be tested with both the single HR setup and the 7x7 HR array setup

For the HR array setup, the cavity length can be varied in steps of 8 mm. Therefore, for each HR the cavity length is rounded to the nearest 8 mm – except for the  $d = 1$  mm superresonance case, for which a special plug is designed. This leads to slight variations in resonance frequency between the different orifice diameters. With the single HR setup, the cavity length can be varied in smaller steps, but it is chosen to use the same cavity lengths as the HR array setup for consistency.

### 5.3. Measurement Techniques

With the available test setup, a variety of measurements can be done to assess the response of a HR and the subsequent effect on the grazing TBL flow. This section outlines the available measurement techniques. In §5.3.1, microphone measurements are outlined. Subsequently, in §5.3.3 and §5.3.2 hot-wire anemometry and particle image velocimetry (PIV) measurements are introduced respectively.

### 5.3.1. Microphones for Acoustic and Wall-Pressure Analysis

Microphone measurements play an important role in quantifying the acoustic response and the subsequent effect on the wall-pressure spectrum of the TBL. The adopted microphone arrangement is presented in Figure 5.7 for the single HR setup. The arrangement consists of two microphones in pin-hole (PH) configuration for wall-pressure measurements, one microphone in the cavity of the HR and a free-stream noise microphone. With GRAS 46BE microphones, a time series of pressure fluctuations is measured at a frequency of  $51.2\text{ kHz}$ .

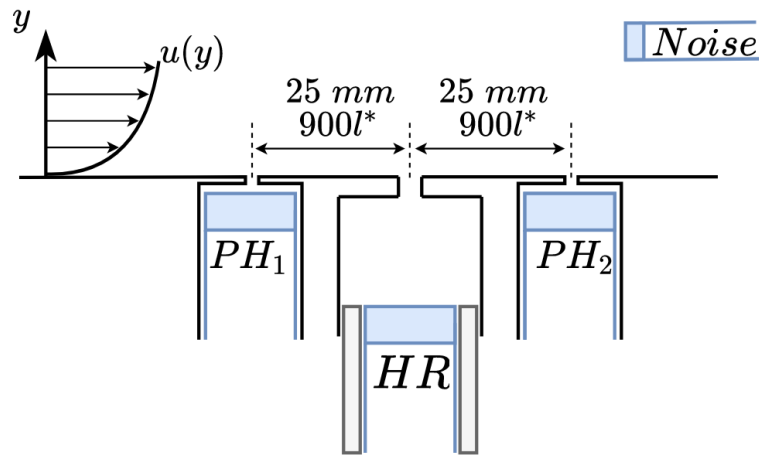


**Figure 5.7:** Schematic of microphone anemometry arrangement for measuring acoustic pressure response of HR with pin-hole microphone setup. Dimensions not to scale for illustrative purposes.

The two microphones in pinhole configuration – one upstream of the HR and one downstream – are used to measure the wall pressure while minimising the disturbance of the grazing TBL flow. The pinholes function as a HR, as visualised in the schematic in Figure 5.8a. The orifice diameter of  $d^+ = 18$  ( $d = 0.5\text{ mm}$ ) and the ratio of neck length and orifice diameter  $t/d = 2$  are based on considerations from Gibeau and Ghaemi (2021). The design resonance frequency is chosen to be  $f_0 = 2700\text{ Hz}$ , such that it is sufficiently high that it does not coincide with highly-energetic frequencies within the wall-pressure spectrum. The frequency is also chosen higher than the frequency of the most energetic velocity fluctuations to not induce a phase shift with the pinhole setup. The sleeve for the pinhole microphones is shown in Figure 5.8b.

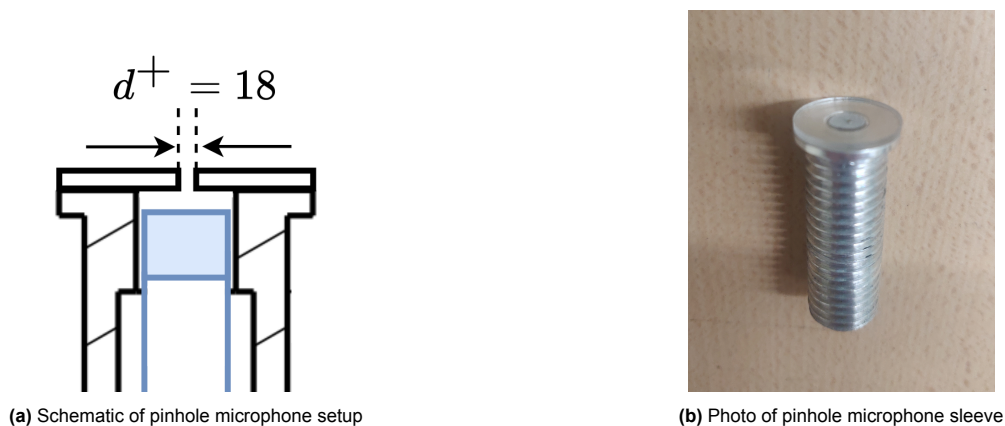


**Figure 5.8:** Pinhole microphone design

The microphone in the cavity of the HR gives insight into the acoustic response of the HR. The microphone is mounted in a sleeve and forms the bottom of the cavity. Through moving the location of the

microphone, the cavity length  $L$  can be influenced to vary the resonance frequency  $f_0$  of the HR. For the HR array setup, microphones can be placed in either one spanwise or one stream row of HRs to measure the interaction between the different HRs.

The measurements from both the pinhole and HR cavity microphones are influenced by facility noise. There are various noise sources in the experimental facility that cannot be eliminated – such as the wind tunnel fan. To be able to correct for the noise, a dedicated noise microphone is placed in the freestream. It is mounted in a holder that also holds the pitot tube for the freestream velocity measurements, as shown in Figure 5.9. The microphone is placed 120  $mm$  away from the sidewall of the test section and approximately 300  $mm$  above the test plate. This is to make sure the microphone is clear of the boundary layers of the setup. It is equipped with a special nose cone to minimise the disturbance to the incoming flow.



**Figure 5.9:** Freestream microphone and pitot tube setup

Before the wind tunnel experimental campaign, an acoustic characterisation campaign of both the HRs and the pinhole microphones is performed at the quasi-anechoic chamber of the A-tunnel at TU Delft. This allows for a comparison of the differences between pure acoustic excitation of HRs and excitation of HRs under a grazing TBL.

The main parameters for the microphone measurements are summarised in Table 5.6, as well as some additional microphone specifications<sup>1</sup>.

Microphones	GRAS 46BE
Acquisition frequency	51.2 $kHz$
Sensitivity $s$	3.34 $mV/Pa$ - 4.60 $mV/Pa$
Frequency range	4 $Hz$ - 80 $kHz$
Dynamic Range	35 $dB(A)$ - 160 $dB$

**Table 5.6:** Main parameters for microphone measurements

### 5.3.2. PIV Measurements

PIV is used to obtain velocity measurements over a two-dimensional plane. The PIV setup consists of the Quantel Evergreen 200 laser, with the Lavision sCMOS and programmable timing unit (PTU) used for the timing and the capturing of images. Instantaneous flow measurements can be performed over a pre-defined field of view (FOV) at 15  $Hz$ . The PIV measurements are done in parallel with the microphone measurements, to allow for the phase-averaging of the PIV measurements.

First, one global FOV was applied, as outlined in Figure 5.10. The PIV measurements were the first flow measurements to be taken. Based on the findings by Urzynicok (2003), a relatively long stream-wise extent of the effects of the larger-scale HR on the TBL flow was expected. Therefore, this FOV

<sup>1</sup><https://www.grasacoustics.com/products/measurement-microphone-sets/constant-current-power-ccp/product/143-46be>

was chosen to verify whether this would also be the case for the inner-scaled HRS. The initial findings were initially intended to indicate how to proceed with the remainder of the flow measurements.

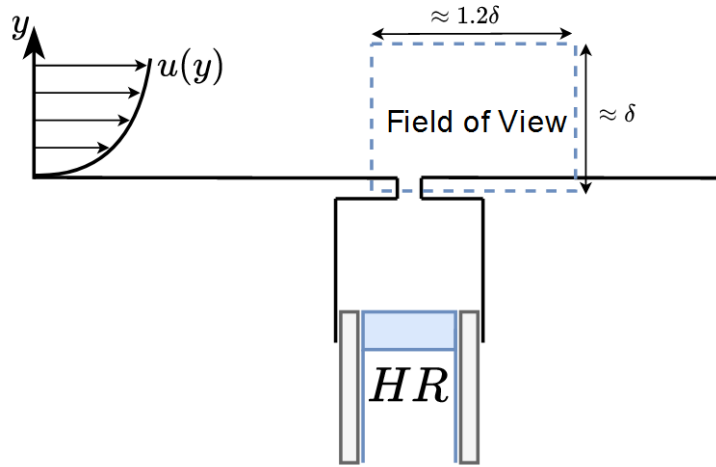


Figure 5.10: PIV field of view arrangements

However, the initial analysis of the PIV measurements of the global FOV showed a very small influence of the HRs on the TBL flow – which is elaborated upon later. Therefore, it was decided to not proceed with two further intended FOVs. These FOVs were a more zoomed-in FOV on the exit of the HR and a wall-parallel plane over the HR array setup.

The main parameters for the PIV measurements are presented in Table 5.7.

Laser	Quantel Evergreen 2000
Synchroniser	Lavision PTU
Camera	Lavision sCMOS
Lens focal length	60 mm
Lens f-stop	8
Camera resolution	2560 pixels x 2160 pixels
Field of View	$\approx 1.2\delta \times \approx \delta$
$dt$ between images in pair	35 $\mu s$
Acquisition frequency	15 Hz
Number of images per measurement	2000

Table 5.7: Main parameters of the PIV measurements

### 5.3.3. Hot-Wire Anemometry

Hot-wire anemometry is used to obtain a time series of the streamwise velocity  $u_{HW}(t)$ . In Figure 5.11, the hot-wire setup is schematised. Using a Dantec 55P15 boundary-layer probe, measurements close to the wall can be obtained. By traversing the probe in the wall-normal direction, a profile of streamwise velocity time series  $u_{HW}(t, y)$  can be obtained. Data acquisition is done using the IFA 300 constant temperature anemometer at a frequency of 51.2 kHz.

The hot-wire anemometer outputs a voltage signal that is converted to a velocity signal using a user-defined calibration. First, the signal is scaled such that at the lowest flow setting ( $U_e = 0 \text{ m/s}$ ) the anemometer output is  $-5 \text{ V}$ , while at the highest flow setting ( $U_e = 15 \text{ m/s}$ ) the anemometer outputs  $5 \text{ V}$ . Subsequently, a 4th order polynomial curve is fitted through 17 measurement points to set the conversion from voltage to velocity. The calibration is repeated periodically to account for variations in atmospheric conditions.

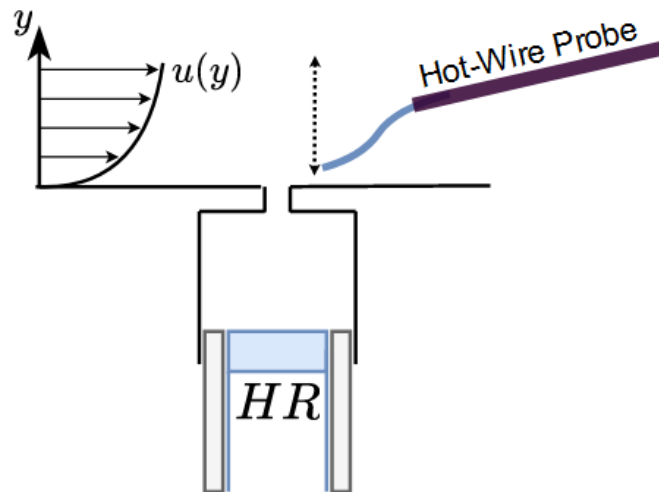


Figure 5.11: Hot-wire arrangement for boundary layer measurements. Not to scale

Before each measurement, the hot-wire probe needs to be positioned relative to the wall. Figure 5.12 illustrates the two different positioning procedures that have been used. Using a telescope a close-up image of the probe can be obtained. However, the exact location of the wall itself is often difficult to see. Typically, when the probe gets sufficiently close to the wall, its reflection can be seen in the wall. The telescope can then be adjusted to measure the distance between the probe and its reflection. This measurement is then equal to twice the wall distance  $y_{wall}$  of the hot-wire probe.

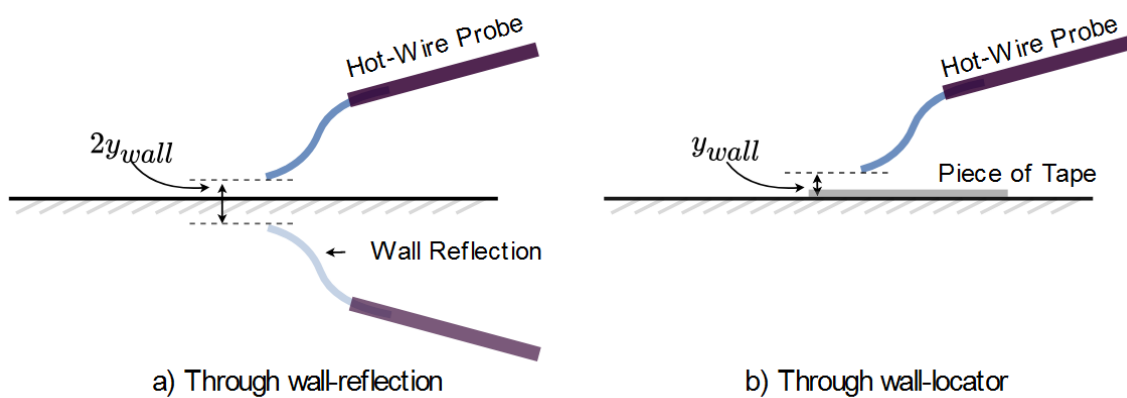


Figure 5.12: Schematics of the applied wall-positioning procedures for the hot-wire probe

In some cases, the reflection of the probe is not clear enough for an accurate measurement. Therefore, as an alternative method, a wall-locator can be used. In this experiment, this was a dark piece of tape positioned behind the probe. The bottom edge of this tape gives a clear reference of the location of the wall. The distance between the bottom edge of the tape and the probe is a direct measurement of the wall distance  $y_{wall}$ .

The telescope used for locating the hot-wire probe can be adjusted in steps of  $0.02 \text{ mm}$  ( $\approx 0.7l^*$ ). Between the two different methods of positioning the probe with respect to the wall, small differences were observed of up to approximately  $0.05 \text{ mm}$  ( $\approx 1.8l^*$ ).

Each hot-wire profile consists of 20 wall-normal measurement locations, using a logarithmic spacing

from  $0.2 \text{ mm}$  to  $3 \text{ mm}$  ( $y^+ \approx 7$  to  $y^+ \approx 108$ ). This allows for capturing the full near-wall cycle with an increased resolution near the wall. All profiles are measured at the same downstream distance of the HR, which was  $4 \text{ mm}$  ( $\approx 144l^*$ ).

The main parameters for the hot-wire measurements are summarised and presented in Table 5.8.

Anemometer	IFA 300
Hot-wire probe	Dantec 55P15
Temperature range	$50^\circ C$
Traverse	Zaber (single-stage)
Acquisition frequency	$51.2 \text{ kHz}$
Measurement range	$0.2 \text{ mm} - 3 \text{ mm}$ ( $7l^* - 108l^*$ )
Measurement points per profile	20
Profile spacing	Logarithmic
Measurement location (downstream of HR)	$4 \text{ mm}$ ( $144l^*$ )

**Table 5.8:** Main parameters for hot-wire measurements

## Data Processing

This chapter outlines how the measurement data will be processed to give insight into the working principles of the proposed HRs and the subsequent effects on the TBL flow. §6.1 introduces the data-processing techniques for the microphone measurements. Subsequently, the data-processing steps for the PIV measurements and the hot-wire measurements are outlined in §6.2 and §6.3 respectively.

### 6.1. Microphone Measurements

Figure 6.1 shows the microphone measurement arrangement of the single HR setup, indicating each of the measured signals  $p(t)$ .

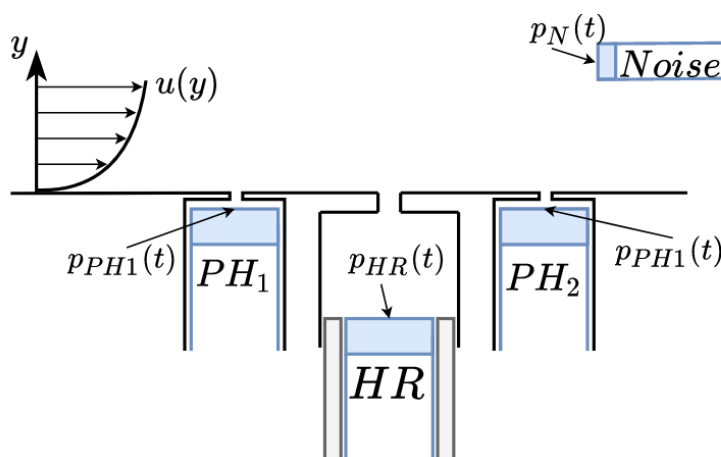


**Figure 6.1:** Schematic of microphone anemometry arrangement for the single HR setup with indication of measured time signals of pressure fluctuations  $p(t)$

The time series of pressure fluctuations  $p(t)$  are measured as voltage signals. Therefore, the signals have to be converted to Pascals using the sensitivity  $s$  of the microphones, expressed in  $mV/Pa$ . Each of the GRAS 46BE microphones has a slightly different sensitivity, in the range of  $3.34 mV/Pa$  to  $4.60 mV/Pa$ . These values are measured by the manufacturer and listed in the datasheet of each respective microphone. With the sensitivity  $s$  known,  $p(t)$  in Pascals then becomes

$$p(t)[Pa] = \frac{p(t)[V]}{s}. \quad (6.1)$$

#### 6.1.1. Spectral Analysis

For each of the signals, the energy spectrum of pressure fluctuations  $\phi_{pp}(f)$  is calculated. As a first step, the non-normalised spectrum of one signal  $S_{pp}(f)$  is calculated using ensemble averaging with ensemble size  $N$  and 50% overlap between ensembles:

$$S_{pp}(f) = \langle P(f)\overline{P(f)} \rangle, \quad (6.2)$$

where  $P_i(f) = \mathcal{F}\{p_i(t)\}$  is the Fourier transform of a single ensemble  $p_i(t)$  and  $\langle \cdot \rangle$  denotes the use of ensemble averaging. The Fourier transform has been implemented using the fast-Fourier transform method in Matlab. Therefore, it has to be scaled using  $N^2/T$  to obtain the spectrum per frequency

step, where  $T$  denotes the measurement time. Furthermore, the spectrum has to be multiplied by 2 to obtain the one-sided spectrum. The normalised energy spectrum  $\phi_{pp}(f)$  then becomes:

$$\phi_{pp}(f) = 2 \frac{S_{pp}(f)T}{N^2} \quad (6.3)$$

For a time series of pressure fluctuations  $p(t)$  the units of the energy spectrum  $\phi_{pp}(f)$  are  $Pa^2/Hz$ . The pre-multiplied energy spectrum can be shown, in which each value of  $\phi_{pp}(f)$  is multiplied by its respective frequency  $f$  or wavenumber  $k$ . Alternatively, the acoustic pressure spectra can be shown using the sound-pressure-level (SPL), which is calculated from  $\phi_{pp}(f)$  as

$$SPL(f) = 20 \log \frac{\phi_{pp}(f)}{(20 \cdot 10^{-6})^2}. \quad (6.4)$$

Both methods are shown in Figure 6.2 for ensemble size  $N = 2^{12}$ . For visualisation purposes, the spectra can be filtered with a bandwidth-moving filter (BMF). Figure 6.3 shows the spectra with a 5% BMF. Applying the filter reduces the noise in the spectra, but also reduces the magnitudes of the peaks. Reducing the ensemble size  $N$  has a similar effect on the peak magnitudes, but simultaneously reduces the resolution of the spectra.

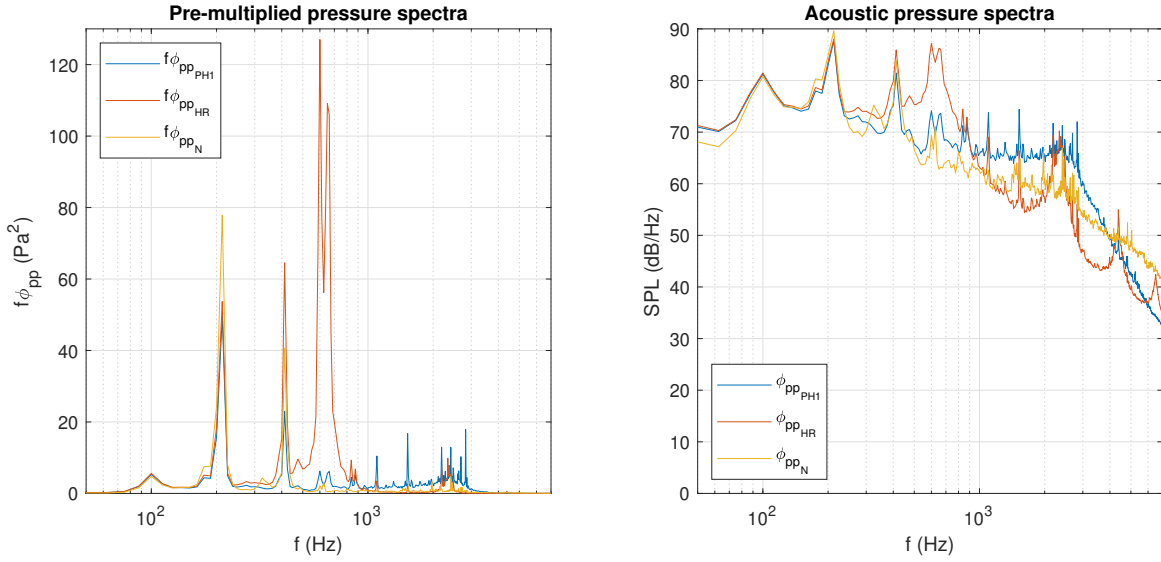


**Figure 6.2:** Non-corrected energy spectra calculated from the microphone measurements with  $N = 2^{12}$  for the single HR setup with  $d^+ = 108$ , subresonance

In Figure 6.3, a clear peak can be seen around the expected resonance frequency for this HR around  $f_0 \approx 600 Hz$ , as well as several overtones at higher frequencies. Additionally, several peaks can be seen that are very similar between the various spectra shown. These can be attributed to wind tunnel noise and other noise sources around the experimental setup.

### 6.1.2. Noise Correction using Linear Spectral Stochastic Estimation

Correcting for the wind tunnel and setup noise is done using linear spectral stochastic estimation. With this method, the cross-spectrum is calculated to find the coherence between two signals, based on the method outlined by Baars et al. (2016). For example, take the HR microphone signal  $p_{HR}(t)$  and the signal from the freestream noise microphone  $p_N(t)$ . The cross-spectrum between the two signals is calculated as

$$S_{pp(N,HR)} = \langle P_N(f) \overline{P_{HR}(f)} \rangle. \quad (6.5)$$

The linear coherence spectrum (LCS) then follows from the cross-spectrum as

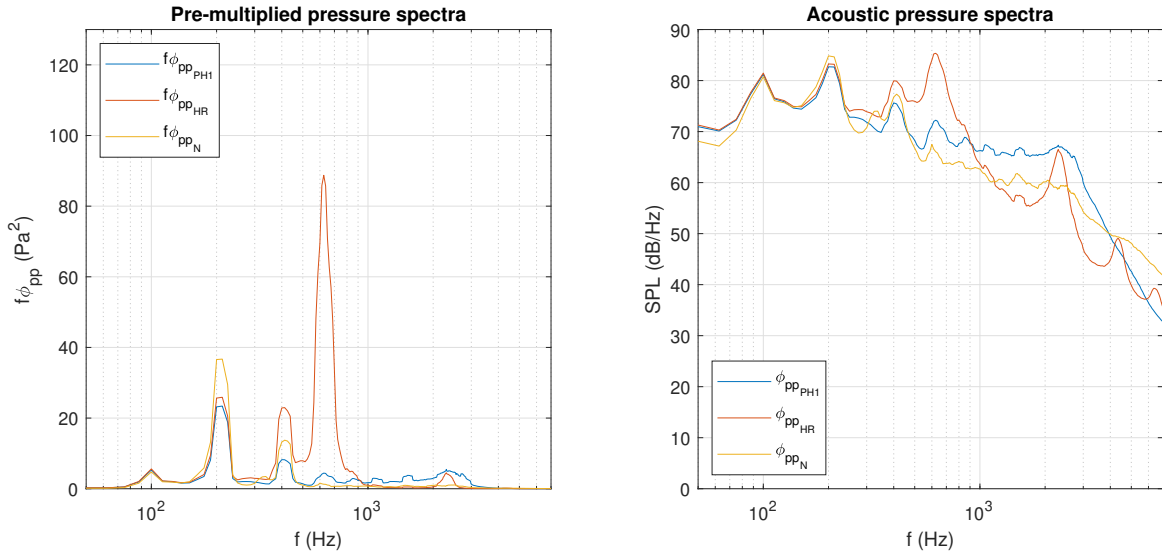


**Figure 6.3:** Non-corrected energy spectra with 5% BMF calculated from the microphone measurements with  $N = 2^{12}$  for the single HR setup with  $d^+ = 108$ , subresonance

$$\gamma^2(f) = \frac{|\langle P_N(f) \overline{P_{HR}(f)} \rangle|^2}{\langle |P_N(f)|^2 \rangle \langle |P_{HR}(f)|^2 \rangle}. \quad (6.6)$$

The magnitude of the LCS indicates how much the analysed signals are coupled (Baars et al., 2016). A value of 0 denotes no coherence and a value of 1 denotes perfect coherence between the signals. The LCS for the signals  $p_{HR}(t)$  and  $p_N(t)$  is plotted in Figure 6.4, with the acoustic spectra as reference. Large values of coherence can be seen between 200 Hz and 400 Hz. Around these frequencies, large peaks are observed in the raw spectra of both signals that show a high resemblance. These peaks are found to be originating directly from the wind tunnel fan noise.

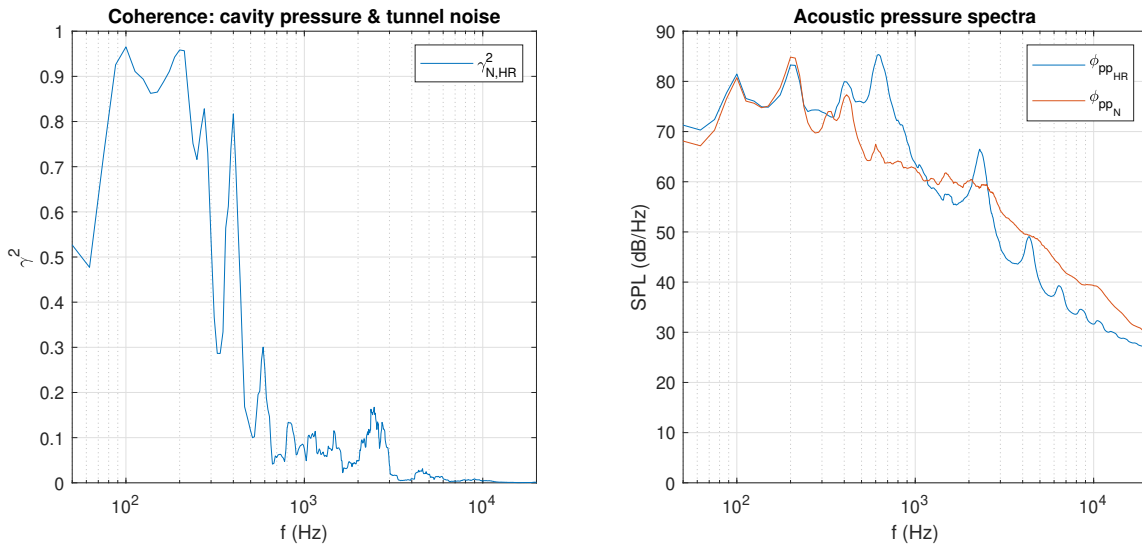


**Figure 6.4:** LCS between the HR microphone signal and the noise microphone signal with  $N = 2^{12}$  for the single HR setup with  $d^+ = 108$ , subresonance. On the right the acoustic pressure spectra of both signals are plotted for reference

The magnitude of the LCS is also used to correct for the noise. If there is a 0.9 coherence between the HR microphone signal  $p_{HR}(t)$  and the noise signal  $p_N(t)$  at a certain frequency, it is assumed that

90% of the energy at that frequency is stemming from the noise source. The other 10% of the energy is then assumed to be from the reaction of the HR to the TBL excitation. With this assumption, the noise-corrected spectrum  $\tilde{\phi}_{pp}$  is calculated as

$$\tilde{\phi}_{pp}(f) = \phi_{pp}(f)(1 - \gamma^2(f)) \quad (6.7)$$

Figure 6.5 shows the noise-corrected pressure spectra  $\tilde{\phi}_{pp}$ . The large peaks that originate from the wind tunnel and setup noise – around 200 Hz and 400 Hz – have almost completely been filtered out. For the HR cavity spectrum  $\tilde{\phi}_{pp}$ , a large peak remains around the expected resonance frequency, as well as the clear overtones around the higher frequencies. The magnitude of the peak has been slightly reduced with the noise-correction procedure. As the procedure removes phase-consistent parts of the signal, there is a risk that the procedure removes more than it should if there is a two-way coupling between the signals.

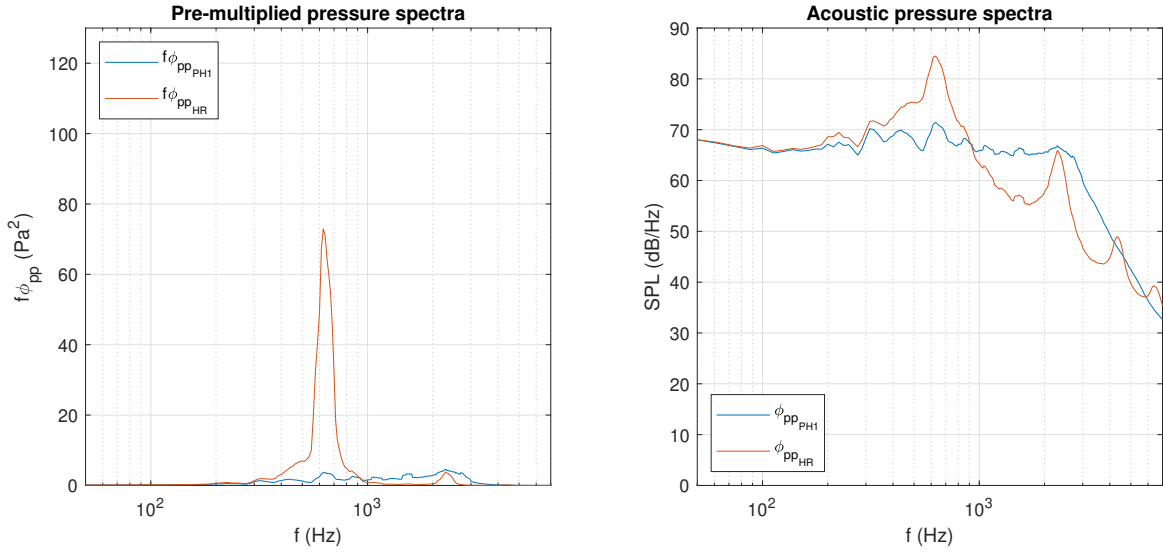


**Figure 6.5:** Noise-corrected energy spectra calculated from the microphone measurements with  $N = 2^{12}$  for the single HR setup with  $d^+ = 108$ , subresonance

Based on the cross-spectrum, an experimental transfer function  $H(f)$  between the two signals can be defined as

$$H(f) = \frac{\langle P_N(f) \overline{P_{HR}(f)} \rangle}{\langle P_N(f) \overline{P_N(f)} \rangle}. \quad (6.8)$$

The transfer function  $H(f)$  is complex-valued, and thus can be split up in a gain and phase modulation (Baars et al., 2016):

$$|H(f)| = \frac{|\langle P_N(f) \overline{P_{HR}(f)} \rangle|}{\langle |P_N(f)|^2 \rangle}, \quad (6.9)$$

$$\angle H(f) = \arctan \left\{ \frac{\text{Re}[\langle P_N(f) \overline{P_{HR}(f)} \rangle]}{\text{Im}[\langle P_N(f) \overline{P_{HR}(f)} \rangle]} \right\} \quad (6.10)$$

Using the transfer function between the signals  $p_{HR}(t)$  and  $p_N(t)$ , an estimate of the noise-corrected time series  $\tilde{p}_{HR}(t)$  is given by

$$\tilde{p}_{HR}(t) = p_{HR}(t) - \mathcal{F}^{-1} [H(f) \mathcal{F}[p_N(t)]]. \quad (6.11)$$

### 6.1.3. Use of Transfer Function to Determine HR Resonance Frequency

The transfer function  $H(f)$  can also be used to determine the resonance frequency of a HR. Consider the noise-corrected spectra as shown in Figure 6.5. If the excitation spectrum of the HR would be purely flat – e.g. a white noise acoustic signal – the peak of the energy spectrum of the HR would directly indicate the resonance frequency of the HR. However, since the energy spectrum of wall-pressure fluctuations of the grazing TBL is not flat, a larger response peak of the HR might be purely a result of larger energy in the excitation spectrum at that frequency.

Recall §4.1, in which the gain and phase modulation of the transfer function  $G(f)$  of a HR were introduced from the second-order model approximation, as a function of HR resonance frequency  $f_0$  and damping constant  $\xi$ :

$$|G(f)| = \left[ \left( 1 - \left( \frac{f}{f_0} \right)^2 \right)^2 + \left( \frac{2\xi f}{f_0} \right)^2 \right]^{-1/2}, \quad (6.12)$$

$$\angle G(f) = -\tan^{-1} \left[ \frac{2\xi(f/f_0)}{1 - (f/f_0)^2} \right]. \quad (6.13)$$

By fitting the second-order model approximation of the transfer function  $G(f)$  to an experimentally obtained transfer function  $H(f)$ , the resonance frequency  $f_0$  and damping  $\xi$  of the tested HR can be found. The damping  $\xi$  is indicative of the magnitude of resonance, with a lower value for  $\xi$  indicating a higher magnitude of resonance. From Equation 6.12, an amplification factor  $\alpha$  can be defined indicating the magnitude of the transfer function gain  $|G(f)|$  at the resonance frequency  $f_0$ :

$$\alpha = \frac{1}{2\xi} \quad (6.14)$$

This section outlines the used methods for determining the HR resonance frequency for the different measurements: 1) for the acoustic excitation measurements in the quasi-anechoic chamber and 2) for the measurement of the HRs under grazing TBL flow.

#### Determine Resonance Frequency for Acoustic Excitation Measurements

For the acoustic characterisation measurements in the quasi-anechoic chamber, a direct reference measurement of the excitation sound source was acquired. Therefore, the second-order model is directly fitted to the experimental transfer function  $H(f)$ . The fit is done using a combined least-squares optimisation of both the phase and gain response using the resonance frequency  $f_0$  and damping  $\xi$  as free variables. As the second-order model only consider the Helmholtz mode, the optimisation is performed on a frequency band between 50% and 150% of the calculated design resonance frequency.

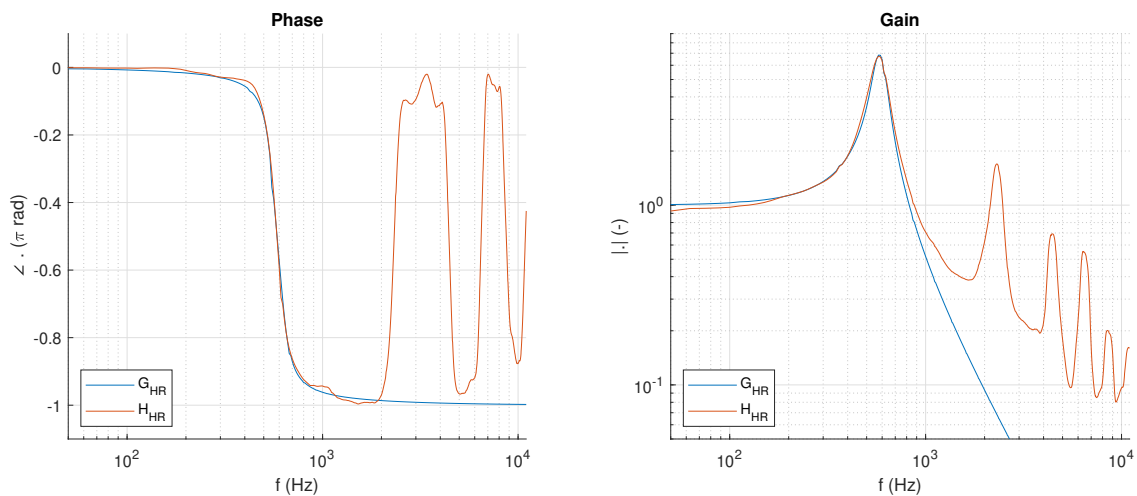


**Figure 6.6:** Experimentally obtained transfer function  $H$  from direct reference measurement, with the second-order model fitted transfer function  $G$ . Measurements from acoustic characterisation for the single HR setup with  $d^+ = 3 \text{ mm}$ , subresonance

The result of this optimisation shown is in Figure 6.6. Around the resonance frequency, the model predicts the HR response with seemingly high accuracy. Therefore, this is a useful tool for determining the resonance frequency  $f_0$  and damping  $\xi$  of a HR. Since in the derivation of the second-order model overtones are not considered, the model fails to accurately predict the response at higher frequencies.

### Determine Resonance Frequency for Turbulent Boundary Layer Excitation Measurements

For the wind tunnel measurements, no direct reference measurement of the wall-pressure spectrum is available. The wall pressure is estimated from the pinhole microphone measurement. From the acoustic excitation measurements in the quasi-anechoic chamber, the transfer function  $G(f)_{PH}$  of the pinhole microphone setup is estimated. The result of the least-squares fit is shown in Figure 6.7. With the second-order model, the response is well predicted up to  $f \approx 4000$  Hz.

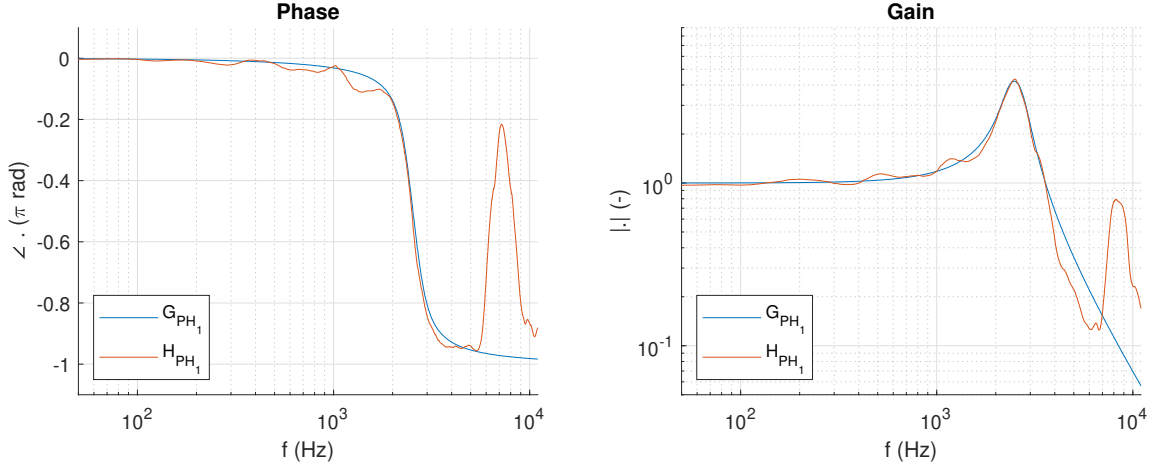


**Figure 6.7:** Experimentally obtained transfer function  $H$  from direct reference measurement, with the second-order model fitted transfer function  $G$ . Measurements from acoustic characterisation for the pinhole microphone.

For the wind tunnel measurements, the wall-pressure spectrum  $\tilde{\phi}_{ppWP}$  is estimated from the noise-corrected pressure spectrum of the pinhole microphone  $\tilde{\phi}_{ppPH}$  using

$$\tilde{\phi}_{ppWP} = \frac{\tilde{\phi}_{ppPH}}{G_{PH}^2}. \quad (6.15)$$

The estimated wall-pressure spectrum  $\tilde{\phi}_{ppWP}$  is then assumed to be the excitation spectrum of the HR. The gain of the experimental transfer function  $|H_{HR}|$  can be estimated as:

$$|H_{HR}| = \sqrt{\frac{\tilde{\phi}_{ppWP}}{\tilde{\phi}_{ppHR}}}, \quad (6.16)$$

in which  $\tilde{\phi}_{ppHR}$  is the noise-corrected pressure spectrum as calculated from the HR cavity microphone signal. This method only gives the gain of the transfer function and contains no information about the phase angle. Therefore, the least-squares fit of the second-order is only performed for the gain of the transfer function. This was found to give results with similar accuracy as compared to the cases in which the least-squares fit was performed using both the phase and gain. Figure 6.8 shows an example of a fit using this method. The phase response of the HR  $\angle G_{HR}$  can be implied from the second-order model.

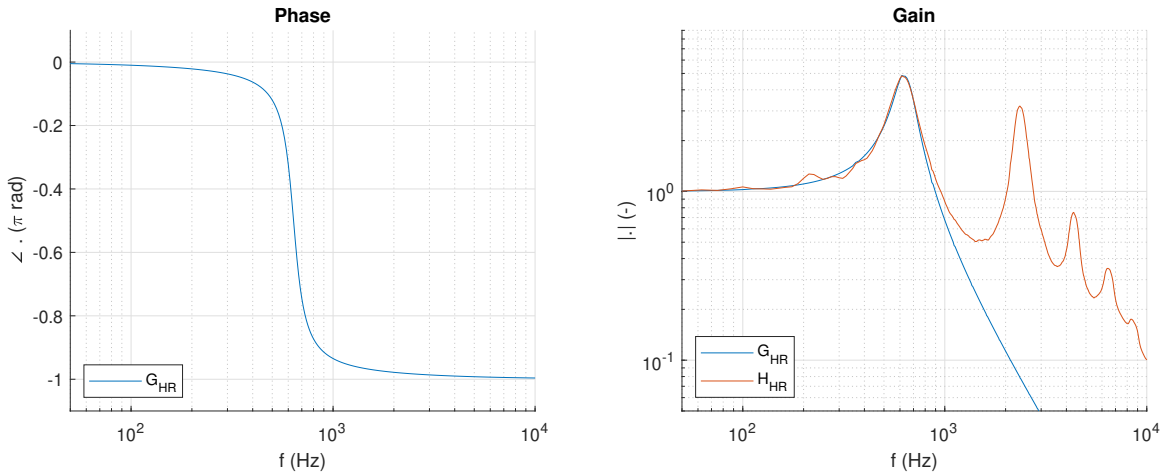


**Figure 6.8:** Experimentally obtained transfer function  $H$  via pinhole measurement, with the second-order model fitted transfer function  $G$ . Measurements from wind tunnel test for the single HR setup with  $d^+ = 3 \text{ mm}$ , subresonance. Phase modulation implied from model as no experimental data is obtained with the used method

### 6.2. PIV Measurements

Figure 6.9 shows the workflow for the processing of the PIV image, with the arrows indicating the results of which processing steps are being used as input for the next processing step. This section elaborates on each of the processing steps and the reasoning behind the interconnection of the processing steps. First, the image pre-processing and processing methods are introduced in §6.2.1 and §6.2.2 respectively. Subsequently, §6.2.3 elaborates on the wall-finding procedure. §6.2.4 introduces a phase-averaging procedure for the PIV images. Finally, some remarks are made on the mean boundary layer profiles and quadrant analysis in §6.2.5 and §6.2.6 respectively.

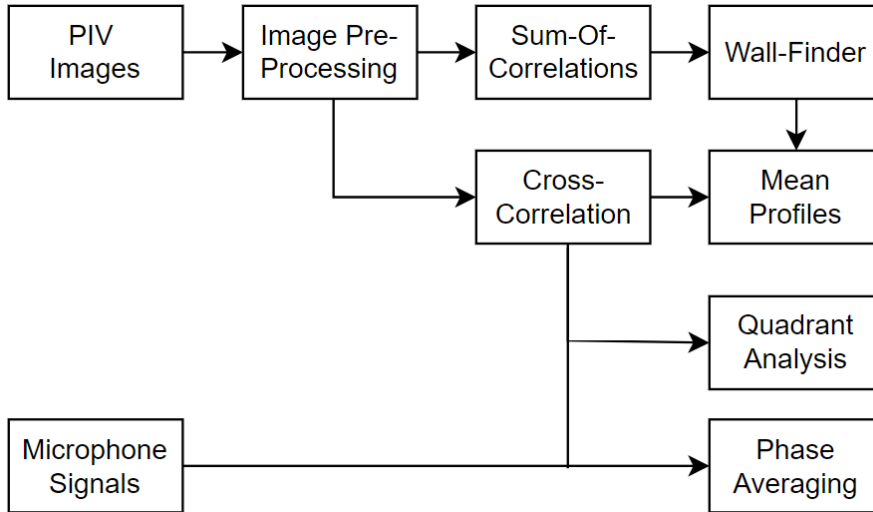


**Figure 6.9:** Workflow for processing of PIV images

#### 6.2.1. Image Pre-Processing

To reduce the influence of reflections on the final PIV results, the raw images were pre-processed. The following pre-processing steps were applied:

1. Butterworth high-pass filter with a length of 7 images
2. Subtract sliding average filter with a length of 12 pixels

The effect of both steps is shown in Figure 6.10. Visible reflections are reduced significantly, at the cost of a reduction in image intensity. However, this is accepted as the individual particles are still clearly recognisable and thus suitable for further processing.

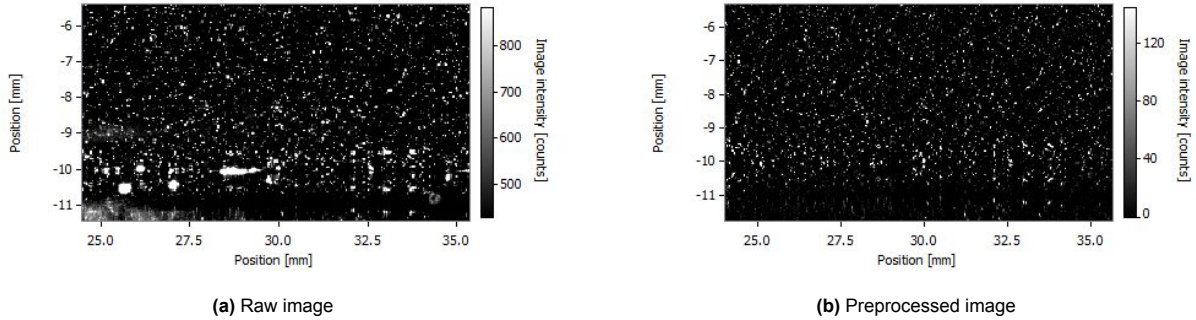


Figure 6.10: Comparison between raw PIV images and the pre-processed PIV images

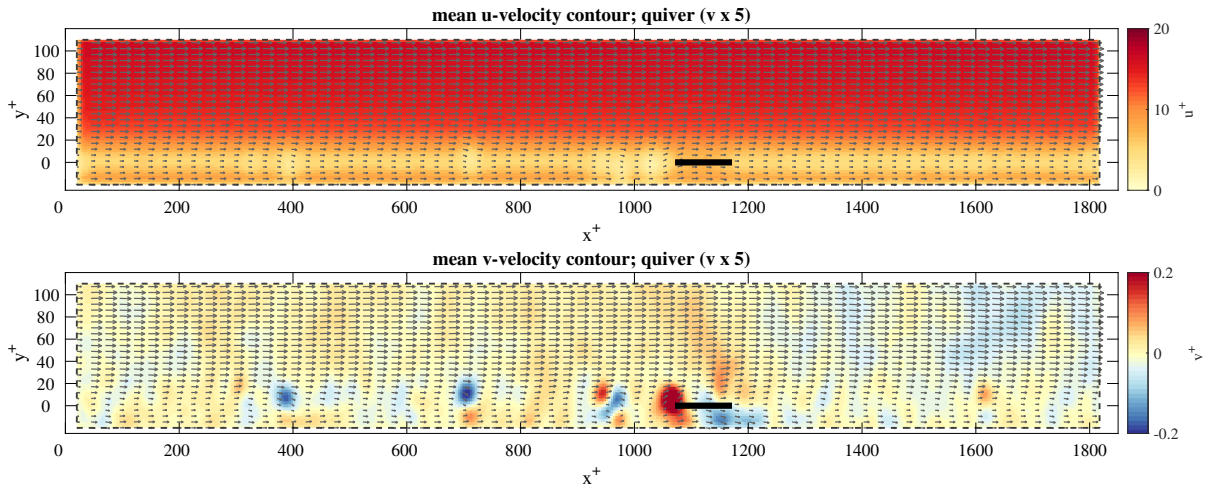
### 6.2.2. Image Processing

Two different statistical methods are used for processing the filtered images into velocity fields. The cross-correlation method processes each image separately, whereas the sum-of-correlation correlates all images from the data set to output one mean velocity field. The used settings and the resulting spatial resolution for both methods are presented in Table 6.1. With the cross-correlation method, larger interrogation window sizes have to be used, but it comes with the advantage that it calculates the instantaneous velocity field for each image. This then allows for certain statistical quantities to be computed. With sum-of-correlations, smaller window sizes can be used. To also reduce the window size of the initial pass, the second image of each image pair is shifted according to the mean velocity obtained from the cross-correlation processing. All window-size are chosen such that they are as small as possible without the introduction of spurious vectors and noise in the resulting images.

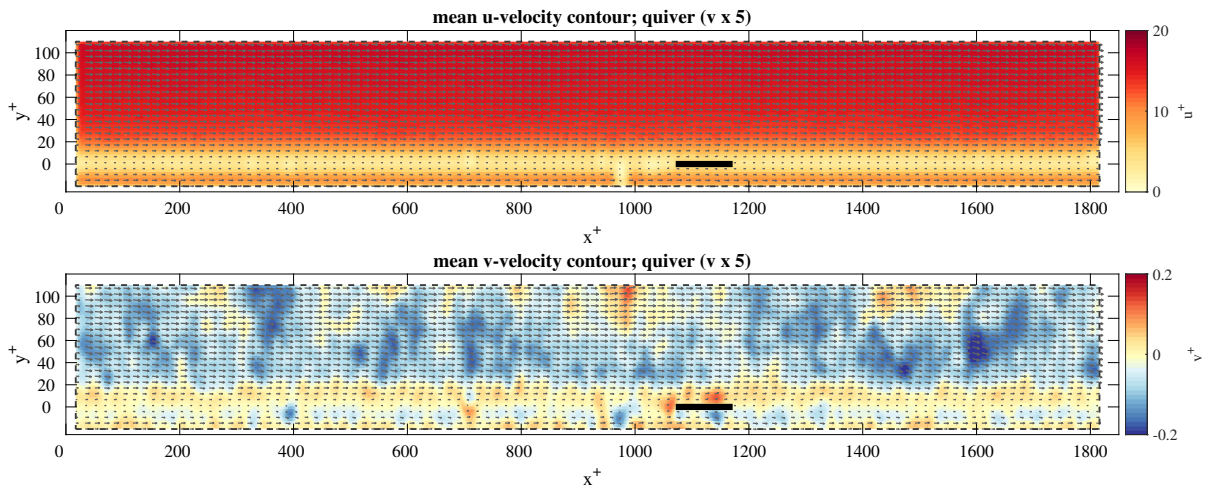
	Cross-Correlation	Sum-Of-Correlations
Preshift	None	Cross-correlation mean velocity
Initial pass window size	32x32 (75% overlap)	24x24 (50 % overlap)
Initial pass window shape	Elliptical 2:1	Elliptical 2:1
Number of initial passes	2	2
Final pass window size	12x12 (75% overlap)	8x8 (75% overlap)
Final pass window shape	Elliptical 2:1	Elliptical 4:1
Number of final passes	2	2
Final pass window shape	Elliptical 2:1	Elliptical 2:1
Spatial resolution ( $mm$ )	0.12	0.08
Spatial resolution ( $l^*$ )	4.19	2.79

Table 6.1: Image processing settings for the cross-correlation method and the sum-of-correlation methods respectively

Figure 6.11 and Figure 6.12 show the resulting mean velocity fields from the cross-correlation processing and the sum-of-correlation processing respectively. Some effects of the reflections remain visible in the cross-correlation processing, despite the image pre-processing. This is most notable around  $x^+ \approx 1080$ , where the reflection from the leading edge of the HR orifice is found. Due to the smaller interrogation window sizes for the sum-of-correlations, the effects of reflections are significantly lower. Combined with the increased spatial resolution, this makes the sum-of-correlations more suitable for determining an accurate wall location. However, further away from the wall, the small interrogation windows cause the results to be noisier. This is especially apparent in the mean  $v$ -velocity contours. For these reasons, it was decided to use the sum-of-correlations processing primarily for determining the wall location, while for the remainder of the data analysis methods the cross-correlation processing is used.



**Figure 6.11:** Mean velocity from the cross-correlation processing for the single HR with  $d_0^+ = 108$ , nominal resonance. Black line indicates the location of the HR orifice



**Figure 6.12:** Mean velocity field as obtained from the sum-of-correlations processing for the single HR with  $d_0^+ = 108$ , nominal resonance. Black line indicates the location of the HR orifice

### 6.2.3. PIV Wall-Finding Procedure

Because of the use of interrogation windows for the processing of PIV images, the exact location of the wall does not directly become apparent from the processed images. Therefore, during post-processing, a wall-finder algorithm has been implemented. For this process, the results of sum-of-correlation processing have been used due to its higher wall-normal spatial resolution.

Figure 6.13 outlines the PIV wall-locating procedure. As a first step, the wall-normal profile of the streamwise mean velocity at  $x = x_i$  ( $u(x_i, u)$ ) has been spline-interpolated to artificially further increase the spatial resolution. Subsequently, the inflection point of the mean velocity profile is sought as it is indicative of the approximate wall location. Figure 6.13a shows an interpolated, uncorrected mean velocity profile around its inflection point. As expected, due to the averaging effects of the interrogation windows, the mean velocity does not go to 0.

In the viscous sublayer of a TBL, the mean velocity profile is linear and thus the velocity gradient is constant. The computed velocity gradient is shown in Figure 6.13b. It can be seen that from the inflection point of the mean velocity profile, the gradient first increases until it hits a peak around  $y = 0.6 \text{ mm}$ .

Afterwards, the velocity gradient reduces steadily. It is assumed that the peak of the velocity gradient coincides with a location in the viscous sublayer that is far enough away from the wall not to be affected by near-wall averaging effects.

Subsequently, a linear fit is made around this point of maximum velocity gradient. This fit is shown in Figure 6.13c. 3 data points before and 3 points after the point of the maximum velocity gradient are used for the linear fit to reduce the fit error. From this linear fit, the wall location can now be determined: the value of the linear fit has to be 0 at the wall. Therefore, the offset required to let the linear fit go through (0,0) is the wall offset. Figure 6.13d shows the mean velocity profile, corrected for the wall offset. This process is now repeated over all streamwise positions in the processed velocity fields. The results are plotted in Figure 6.14, as well as a second-order polynomial fit. This fit has been used in subsequent processing steps as the wall position.

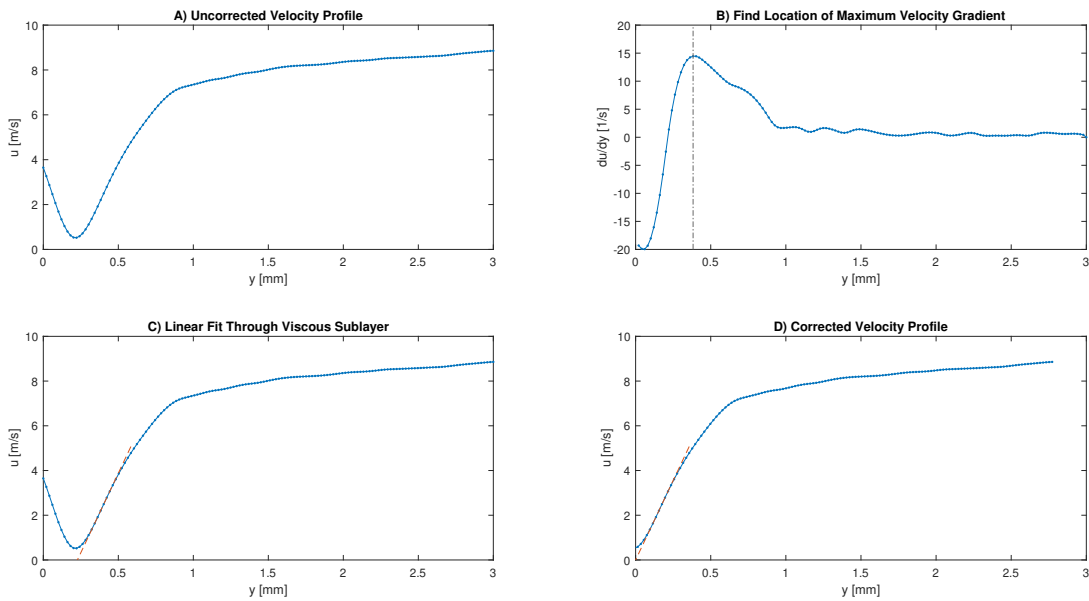


Figure 6.13: PIV wall-finding procedure

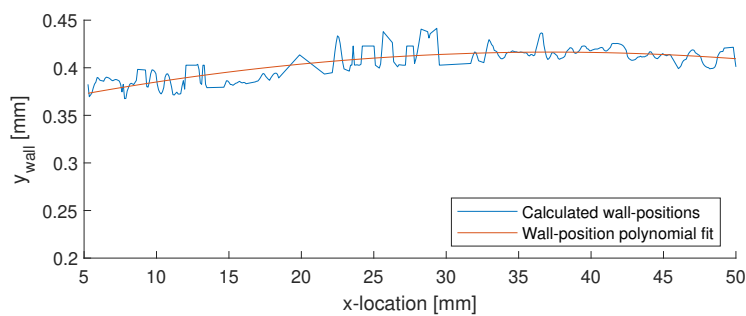
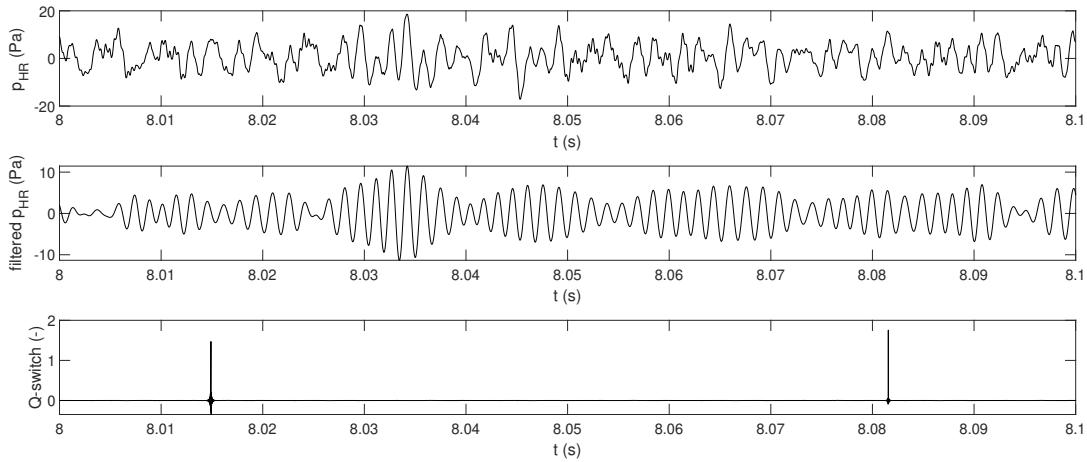


Figure 6.14: Results from the PIV wall-finding procedure with a polynomial fit for the single HR with  $d_0^+ = 108$ , nominal resonance

#### 6.2.4. Phase-Averaging

It is postulated that the HR induces a harmonic perturbation in the grazing TBL flow. To visualise and assess this over a cycle of HR resonance, the results of the PIV are phase-averaged. The capturing of each PIV image is triggered by the PTU system with a pulse signal. This trigger signal can be acquired as a time-series voltage signal and allows to record the timestamp of each image. Combined with

the simultaneous microphone measurements this forms the basis for the phase averaging of the PIV measurements. Figure 6.15 shows a snapshot of the cavity microphone signal, the bandpass filtered HR cavity signal 100  $Hz$  above and below the HR resonance frequency, and the trigger signal.



**Figure 6.15:** Visualisation of the signals used for the phase averaging of PIV images.

For each HR pulse of the trigger signal, it can be identified what the corresponding phase is of the filtered cavity signal. Each pulse is stored in either of 6 bins, which are divided equally over a single period of the HR resonance. To limit the noise in the results, only pulses corresponding to 'strong resonance' events are stored. A strong resonance event is when the peak of the period around a pulse is larger than 55 % of the total signal standard deviation. A signal corresponding to the trigger pulses is shown in Figure 6.16. For the shown case, 1649 out of 2000 pulses are binned.

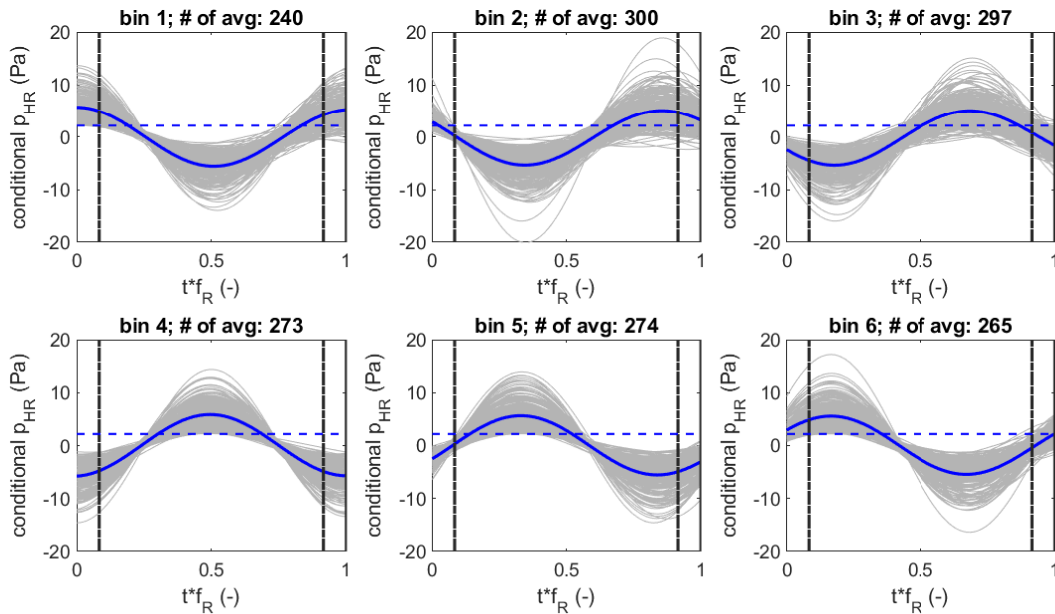


**Figure 6.16:** Results of the binning procedure for the phase-averaging of the PIV measurements for the single HR with  $d_0^+ = 108$ , subresonance

Subsequently, per bin, all of the instantaneous velocity fields from the cross-correlation processing corresponding to these pulses are averaged. This is done separately for both the streamwise velocity

$u$  and the wall-normal velocity  $v$ . Before the averaging, all velocity fields are filtered with a Gaussian filter to reduce the noise in the results. To further enhance the convergence of the results, the assumption of inflow-outflow symmetry is made. With this assumption, it is assumed that the effect of inflow is the exact opposite of that of outflow. Therefore, all events corresponding to bin 4 of Figure 6.16 are multiplied by  $-1$  and then added to bin 1. This then increases the number of images used for the averaging of bin 1 from 240 to 513.

### 6.2.5. Mean Boundary Layer Profiles

With the wall positions found, the mean velocity profiles of the TBL can be established. While for the wall-locating procedure the sum-of-correlation processing method has been applied, it was decided to use the averaged cross-correlation processing for the mean profiles. The cross-correlation shows better convergence than the sum-of-correlations due to the larger window sizes. The profiles are averaged over a streamwise extent of  $5 \text{ mm}$  to reduce the effect of local inaccuracies of the processing.

### 6.2.6. Quadrant Analysis

Using the instantaneous velocity fields from the cross-correlation processing, a quadrant analysis of the velocity fluctuations is performed, as outlined in Figure 6.17. Per data-set, one upstream and one downstream quadrant analysis is performed on a rectangular area of  $5 \text{ mm} \times 0.6 \text{ mm}$ , corresponding to 50 and 5 data points respectively. The area is centred at a wall-normal location of  $y^+ = 25$ .

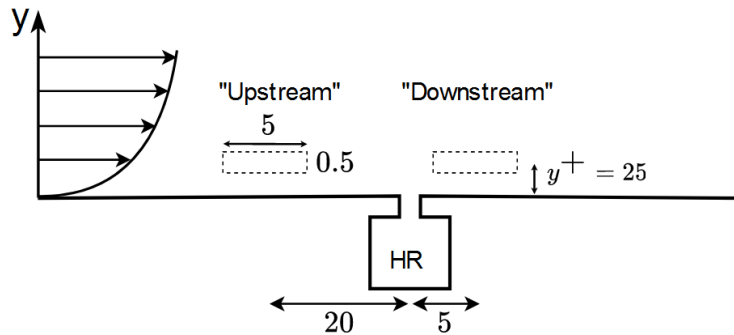


Figure 6.17: Schematic for the quadrant analysis as applied to the PIV instantaneous velocity fields

## 6.3. Hot-Wire Measurements

This section outlines the processing steps for the combined hot-wire and microphone measurements, with the obtained signals outlined in Figure 6.18. First, the wall-correction procedure is introduced in §6.3.1. Subsequently, some remarks are made for the spectral analysis performed on the hot-wire measurements in §6.3.2. Finally, the VITA analysis and phase-averaging procedure are outlined in §6.3.3 and §6.3.4 respectively.

### 6.3.1. Correction of Wall-Position

The available methods for positioning the hot-wire probe with respect to the wall are not perfectly accurate, with a measurement error of approximately  $0.02 \text{ mm}$  ( $\approx 0.7l^*$ ) and an observed difference between the used methods of up to  $0.05 \text{ mm}$  ( $\approx 1.8l^*$ ). Offsets of this magnitude in wall-positioning can already significantly affect the results in the near-wall region. From the non-corrected data in Figure 6.19, it becomes clear that there likely is an offset in the wall position between the measurements. From the non-corrected data, it appears there is a significant decrease in velocity near the wall. The maximum variance is increased but the profile appears to be shifted wholesale to higher  $y^+$ . The results also do not agree with what was later found in the PIV measurements.

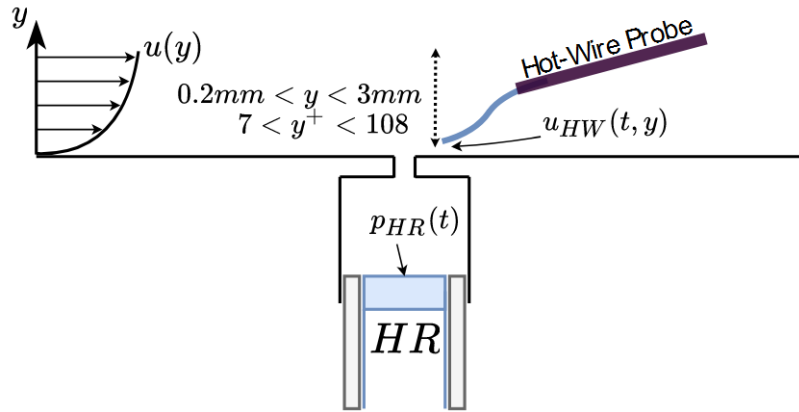


**Figure 6.18:** Schematic of the hot-wire anemometry arrangement indicating the measured signals and measurement region

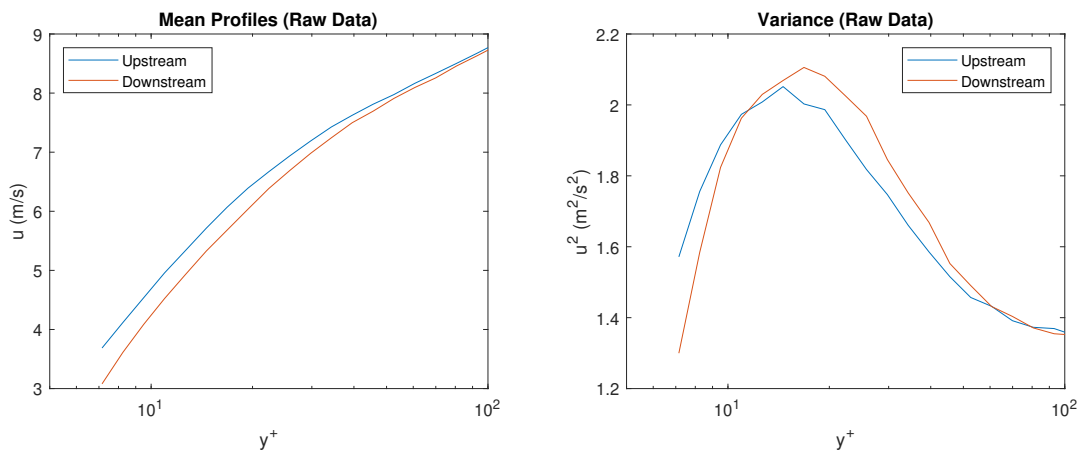


**Figure 6.19:** Non-corrected hot-wire measurements for the single HR setup with  $d^+ = 108$ , subresonance

Therefore, to gain confidence in the accuracy of the results, the first processing step of the hot-wire measurements is to correct the wall position. This correction is done through a least-squares fit of the measured mean profiles to a reference profile of a TBL from DNS at  $Re_\tau = 2000$ <sup>1</sup>. Two variations of the fitting procedure were performed:

1. Fit in the region  $25 < y^+ < 95$ : Initial analysis showed coherence between the microphone signals until  $y^+ = 25$ . It was then assumed that the profiles upstream and downstream of the result would be identical beyond this point.
2. Fit in the region  $6 < y^+ < 95$ . This tries to fit the mean profile to the reference DNS profile over the full measurement range.

In Figure 6.19, the results of the two fits are shown. The fit between  $25 < y^+ < 95$  shows a significant increase in mean velocity and variance very close to the wall. It also requires a shift in wall position that is almost beyond the perceived accuracy of the initial wall-positioning methods. The fit between  $6 < y^+ < 95$  shows a mean velocity deficit between  $15 < y^+ < 40$ . This result appears similar to what was found by Urzyncok (2003) for larger-orifice HRs – with the present measurement affecting a region closer to the wall. This method is also more in agreement with what was later found with the PIV measurements. Furthermore, the required shift in wall position is small and in the order of the measurement accuracy of the initial wall-positioning procedure. For these reasons, the DNS fit between  $6 < y^+ < 95$  is used for all hot-wire measurements.

<sup>1</sup>Obtained from [https://turbulence.odon.utexas.edu/channel2015/content/Data\\_2015\\_2000.html](https://turbulence.odon.utexas.edu/channel2015/content/Data_2015_2000.html)

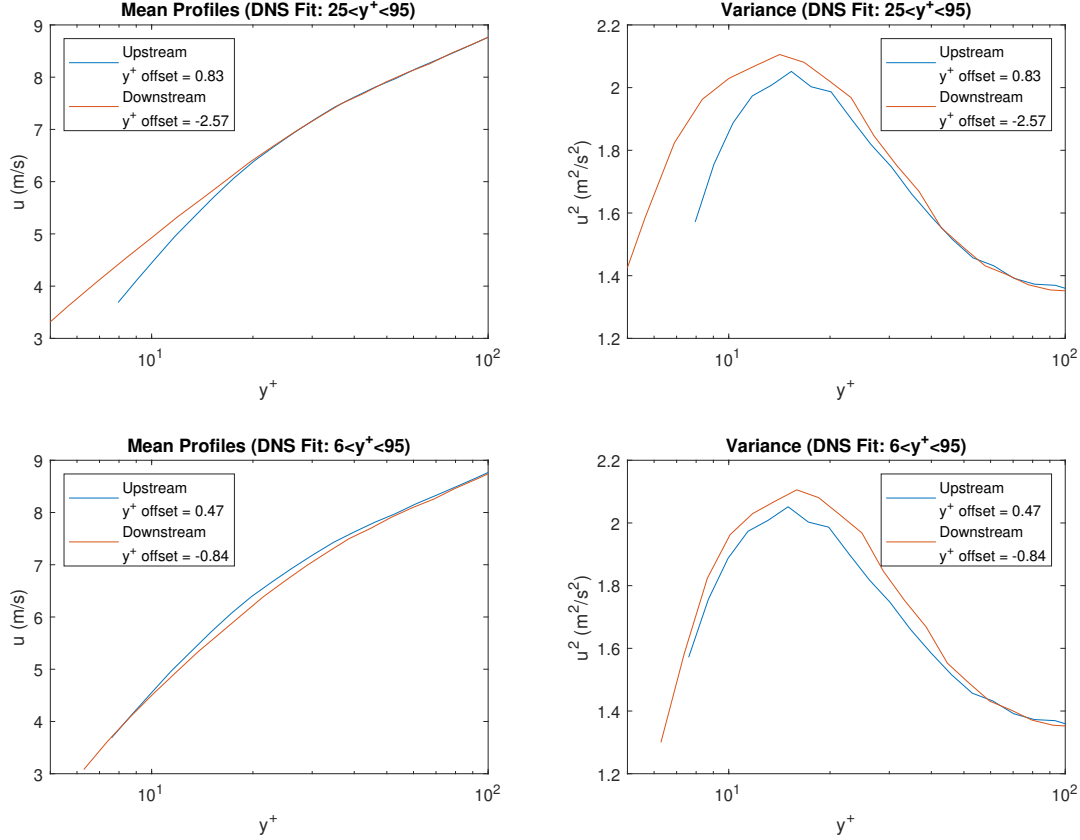


**Figure 6.20:** Two variations of the wall-correction procedure for the hot-wire measurements through least-squares fit with a reference DNS profile.

### 6.3.2. Spectral Analysis

For each of the 20  $y^+$ -stations of the hot-wire profile, the pre-multiplied energy spectrum can be generated from the time series of streamwise velocity  $u_{HW}(t)$ . This process is identical to the generation of the spectra for the microphone measurements as outlined in §6.1.1, without the need for noise-correction. The spectra are plotted as contour plots using the streamwise wavelength  $\lambda_x^+$  and wall-normal location  $y^+$  on the axes.

All spectra are generated with the wall-offset  $\Delta y^+$  applied from the wall-finder procedure. The results are then interpolated on a common  $y^+$ -grid to allow for calculating the spectral differences. All values for  $\lambda_x^+$  are calculated using one reference  $U_\tau$  and with the convection velocity  $U_c$  as outlined in §2.6.2.

### 6.3.3. VITA Analysis

The main analysis method used for the micro-cavity array study of Silvestri et al. (2017a), is the variable-interval time averaging (VITA) analysis. This method was introduced by Blackwelder and Kaplan (1976) and attempts to detect sweep and ejection events from a streamwise velocity time series by detecting higher-than-average levels of signal variance. Over a small time interval  $T_w$ , the local time average  $\hat{u}(t, T_w)$  is defined as (Silvestri et al., 2017a)

$$\hat{u}(t, T_w) = \frac{1}{T_w} \int_{t-T_w/2}^{t+T_w/2} u(s) ds. \quad (6.17)$$

To accurately capture the near-wall turbulence events,  $T_w$  should be in the order of the viscous time scale (Blackwelder and Kaplan, 1976). For this study, this value is selected to be  $T_w^+ = 15$ . From the local time average  $\hat{u}(t, T_w)$  the local variance  $Var(t, T_w)$  can be calculated as

$$Var(t, T_w) = \hat{u}^2(t, T_w) - [\hat{u}(t, T_w)]^2. \quad (6.18)$$

Based on the value of the ratio of the local variance  $Var(t, T_w)$  and the variance of the full signal  $Var(t)$ , it is judged whether a sweep or ejection has occurred. This ratio is denoted by  $k$  and a typical threshold value for the detection of a sweep or ejection event is 1.2 (Silvestri et al., 2017a). To distinguish between a sweep or ejection event, the local time derivative  $du/dt$  of the velocity is analysed. When  $du/dt > 0$ , a sweep event is considered to have occurred and an ejection event has occurred when  $du/dt < 0$ . As such, a detection vector  $D(t)$  for sweep and ejection events can be established such that

$$D(t) = \begin{cases} 1 & \text{if } Var(t, T_w) > kVar(t) \text{ and } du/dt > 0 \text{ (sweep)} \\ 0 & \text{if } Var(t, T_w) < kVar(t) \\ -1 & \text{if } Var(t, T_w) > kVar(t) \text{ and } du/dt < 0 \text{ (ejection)} \end{cases} \quad (6.19)$$

The process of generating the detection vector  $D(t)$  is visualised in Figure 6.21. The detection function is filtered such that every event only appears once in the detection vector.

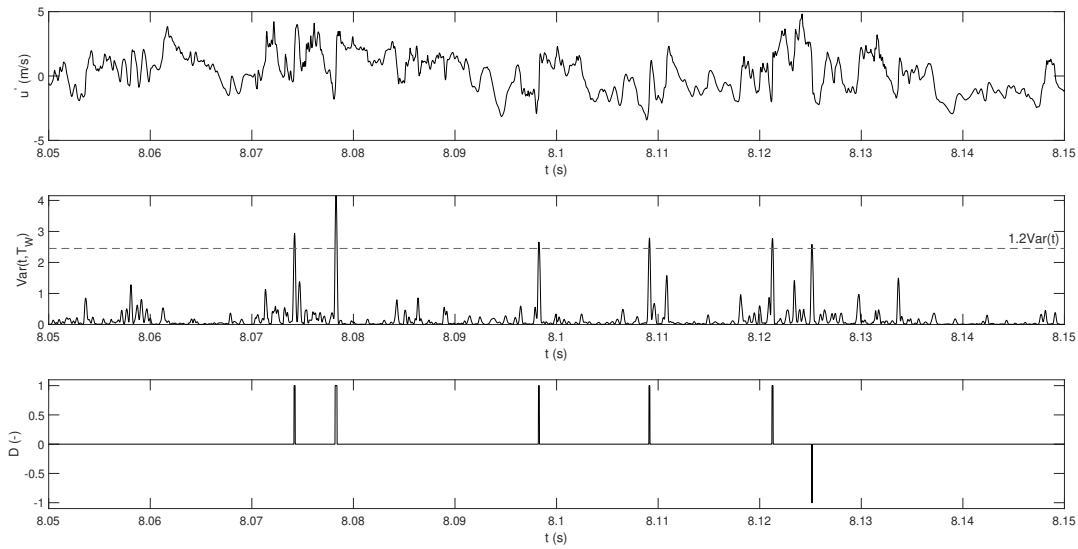


**Figure 6.21:** Visualisation of the detection procedure of VITA-events using detection function  $D$

When a sweep or ejection event has been detected, the point with the maximum value of  $|du/dt|$  is considered to be the moment the event occurs. Subsequently, the event is plotted over a range of  $[t - T_{ens}, t + T_{ens}]$ , with  $T_{ens}^+ = 30$  (Silvestri et al., 2017a). The results of a VITA analysis for sweep events are shown in Figure 6.22. The average of the found sweep events is an indication of its characteristics. The time between peaks of the averaged sweep can be considered the 'sweep duration'. The peak-to-peak value of the averaged sweep event can be considered a measure of the 'sweep intensity' (Silvestri et al., 2017a).

### 6.3.4. Phase-Averaging

The simultaneous hot-wire and microphone measurements allow for phase-averaging of the hot-wire measurements. First, the HR cavity pressure time series  $p_{HR}(t)$  is band-pass filtered around the measured HR resonance frequency  $f_0$ . As the response of the HR is not perfectly harmonic, a band of 100 Hz below and above the resonance frequency is used for the band-pass filter. From the filtered signal, the local peaks can be found and the timestamps of each peak can be stored in a pulse vector. This vector is then used as input for a time-synchronous averaging of the hot-wire signal. Figure 6.23 shows an instantaneous snapshot of the involved signals.

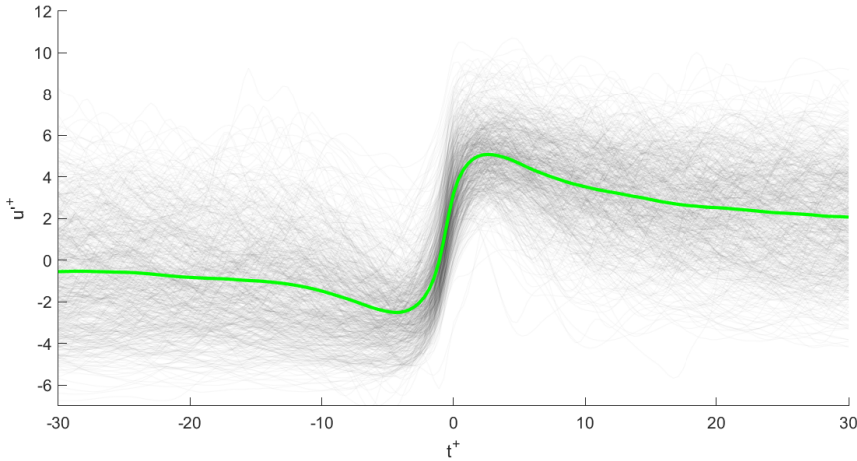


Figure 6.22: VITA analysis for sweep events for the single HR setup with  $d_0^+ = 108$ , subresonance. Grey lines indicate individual detected events, with the average of all events indicated in green.

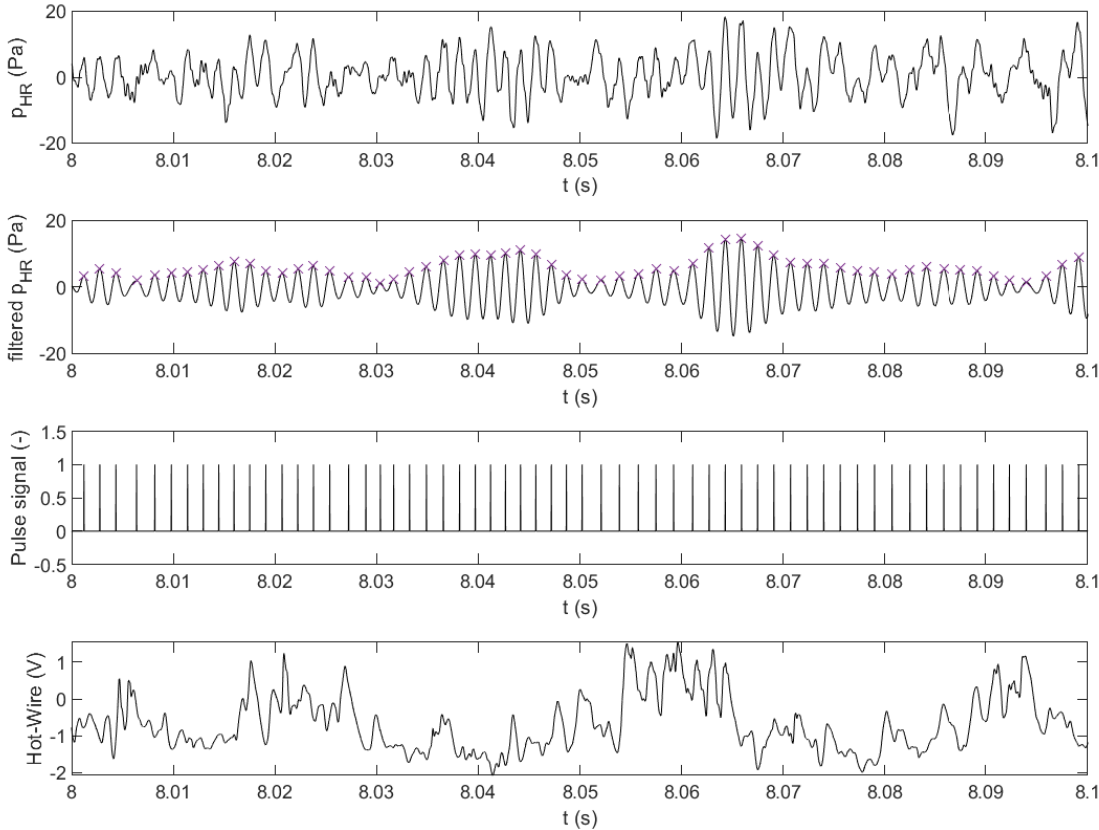


Figure 6.23: Visualisation of the used time signals for the phase-averaging of the hot-wire measurements

## Results: Microphone Measurements

This chapter presents the results of the microphone measurements to characterise the acoustic response of the tested HRs. First, §7.1 presents the results for the acoustic characterisation of the HRs as measured in the quasi-anechoic chamber of the A-Tunnel at the TU Delft. Subsequently, the results for the TBL excitation of HRs are presented in §7.2.

### 7.1. Acoustic Characterisation of Helmholtz-Resonators

The results for the acoustic characterisation of the tested HRs are presented in Figure 7.1, with the calculated values for the resonance frequency  $f_0$ , damping  $\xi$  and amplification factor  $\alpha$  presented in Table 7.1. For the HRs with orifice diameters  $d_0 = 2 \text{ mm}$  and  $d_0 = 3 \text{ mm}$  the measured resonance frequencies match the calculated frequencies closely. For the HRs with  $d_0 = 1 \text{ mm}$ , the resonance frequencies deviate more. However, very low amplitudes of resonance are achieved with relatively high noise at this orifice diameter. Therefore, the second-order model fit to determine the resonance frequency cannot be applied with high accuracy.

Two main general trends are observed with respect to the amplification factors of the tested HRs: 1) the amplification factor significantly increases with increasing orifice diameter and 2) the amplification factor appears to increase slightly with reducing the resonance frequency for the same orifice diameter. These changes appear to be primarily caused by the relative geometric differences of the HRs. With increasing orifice diameter, the ratio of neck thickness to orifice diameter  $t/d$  reduces and the ratio of cavity length to diameter  $L/D$  increases. By reducing the resonance frequency for the same orifice diameter,  $L/D$  increases as well.

The change in neck length-to-orifice diameter  $t/d$  is considered to be the primary reason for the observed differences between the orifice diameters. The friction loss within the neck of a HR is hypothesised to be one of the main sources of damping within the HR system. Therefore, a reduction in the relative neck length of a HR could result in reduced friction losses. This then reduces the damping of the HR system and appears in the results as an increased amplification factor.

The change in the ratio of cavity length to cavity diameter  $L/D$  was initially not expected to have a large effect on the HR resonance, as the resonance frequency is primarily dictated by the HR cavity volume. If anything, it was expected that friction losses within the cavity would slightly increase, with increased damping as a result. However, upon further analysis, there are small signs from studies by Selamet et al. (1997) that increasing  $L/D$  results in a higher pressure level at the bottom of the HR cavity due to a change in the propagation of the pressure waves within the HR cavity. At low  $L/D$ , radial propagation is dominant, whereas at high  $L/D$  axial propagation is dominant. In the simulations shown by Selamet et al. (1997), the HRs with  $L/D$  – and thus primarily axial propagation of pressure waves – higher pressure levels are measured at the bottom wall of the HR cavity. Since the microphones are placed at the bottom of the HR cavity, this could explain the observed changes.

The observed differences are slightly larger than what was anticipated during the design phase. In the further interpretation of the results of this study, these differences will have to be taken into account.

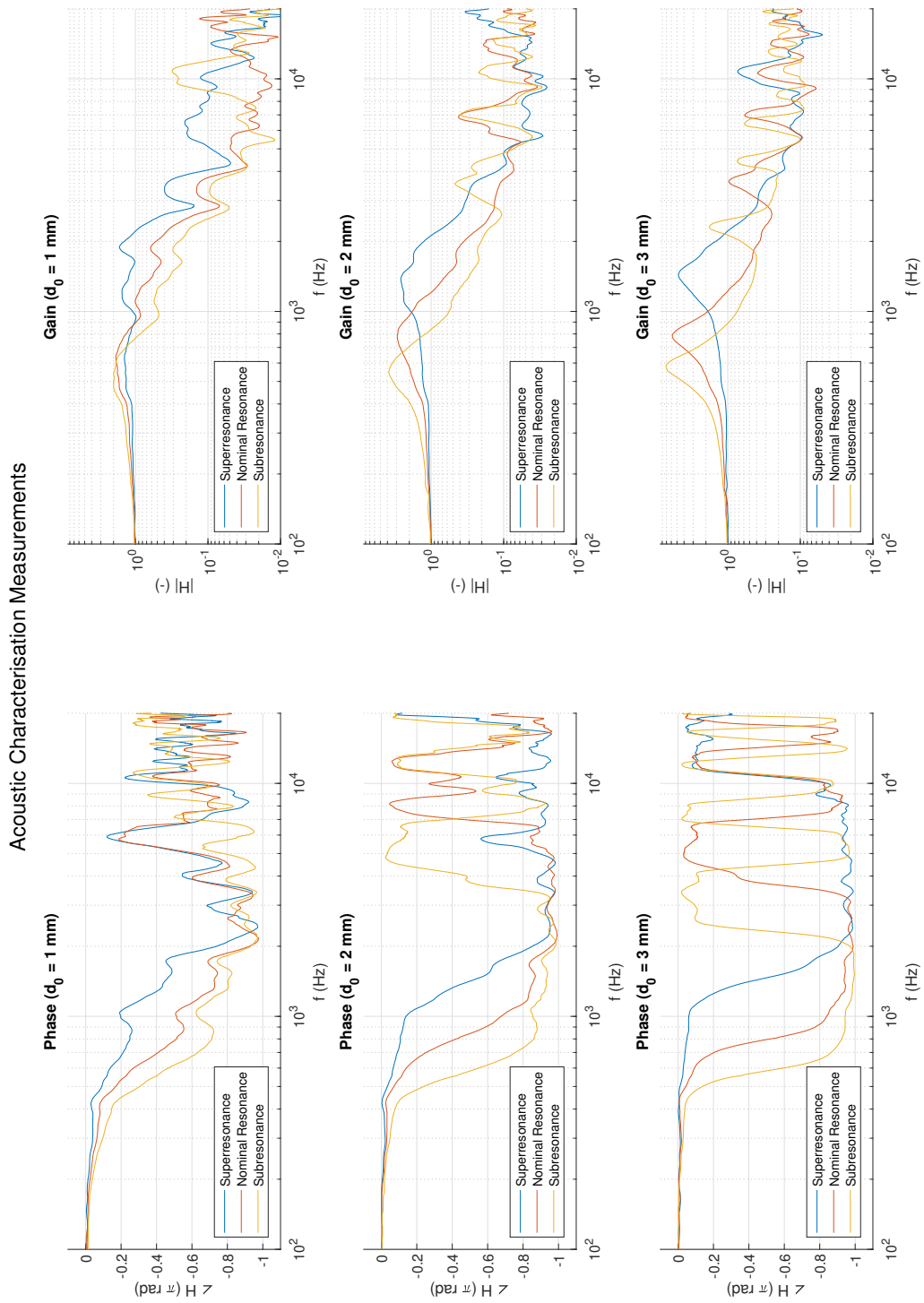


**Figure 7.1:** Phase and gain of the measured transfer function  $H_{HR}$  for the acoustic characterisation measurements of the tested HRs

$d_0$ [mm]	Resonance	Predicted $f_0$ [Hz]	Measured $f_0$ [Hz]	$\xi$ [-]	$\alpha$ [-]
1	Superresonance	1580	1670	0.4162	1.20
	Nominal resonance	797	767	0.322	1.55
	Subresonance	560	601	0.2564	1.95
2	Superresonance	1485	1414	0.1948	2.57
	Nominal resonance	843	827	0.1679	2.98
	Subresonance	581	574	0.1258	3.97
3	Superresonance	1454	1454	0.0996	5.02
	Nominal resonance	794	791	0.080	6.24
	Subresonance	585	582	0.062	8.04

**Table 7.1:** Summary of acoustic characterisation results. The measured resonance frequencies and damping result from the second-order model approximation fit of the measured transfer functions.

Figure 7.2 shows how the model-predicted overtones compare to the acoustic measurements. All modes – both the HR resonance frequency and the subsequent overtones – are predicted accurately, confirming that the designed HRs work as expected. An interesting note can be made with regards to the effect of the overtones on the phase response of the HRs. For the HR resonance frequency, the phase response closely follows the predicted behaviour from the second-order model approximation. However, each subsequent overtone seems to induce an opposite phase switch around the frequency of that overtone. This behaviour is present for all measured HRs, but is most clearly visible for the HRs with  $d_0 = 3$  mm. Since the measured values of the gain at the overtones are relatively low, it is not expected that this observed behaviour will have a significant influence on the effect of the tested HRs on the TBL flow.

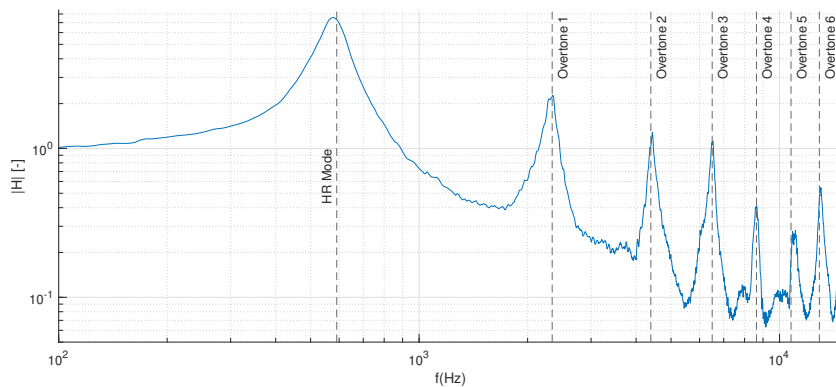


**Figure 7.2:** Transfer function gain as function of frequency. Dotted lines indicate the calculated frequencies of the overtones. Wind tunnel measurements for single HR setup for  $d_0 = 3$  mm, subresonance

## 7.2. Turbulent Boundary Layer Excitation

This section presents the results for the TBL excitation of HRs. First, the measurement of the wall-pressure spectrum is introduced in §7.2.1, before the response of the single HRs to TBL excitation is presented in §7.2.2. In §7.2.3 and §7.2.4 remarks are made on the downstream wall-pressure measurements and the measurements from the HR array setup, respectively.

### 7.2.1. Measured Wall-Pressure Spectrum with Pinhole Microphones

Figure 7.3 shows the pre-multiplied wall-pressure spectrum as calculated from the pinhole microphone measurements, as well as a reference wall-pressure spectrum from a DNS simulation at  $Re_\tau = 2000$  Panton et al. (2017). For the pinhole measurements, both the raw and noise-corrected calculated pressure spectra are presented. The wall-pressure spectrum from the noise-corrected pinhole measurement appears to match the DNS wall-pressure spectrum closely up to  $\lambda_x^+ \approx 400$ , but is under-approximated at higher wavelengths. However, this is potentially a result of the noise-correcting procedure over-correcting at the higher wavelengths. The noise at these higher wavelengths corresponds to the wind tunnel and setup noise which is present across all measurements taken. This noise may be

dominant in the excitation of the pinhole response, rather than the pressure waves at this wavelength from the TBL flow. This could cause the noise-correcting procedure to overestimate the correction.

The underestimation of the wall-pressure spectrum at higher wavelengths is not deemed to be problematic for the use of the pinhole measurements for the determination of the resonance frequencies of the HRs under TBL excitation. As the noise-correction procedure is identical for both the pinhole measurements and the HR cavity measurements, any possible overestimation of the noise correction will apply to both measurements. Since the transfer function is based on the ratio of pressure spectra, the relative difference between the pinhole measurement and the HR cavity measurement will still be an accurate representation.

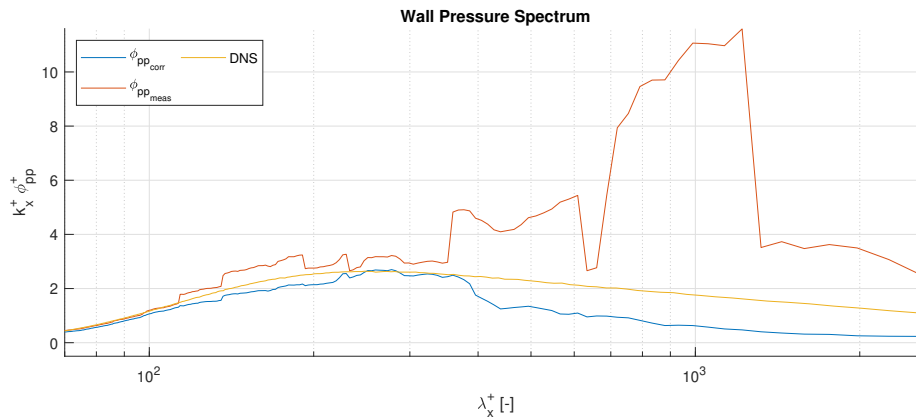


**Figure 7.3:** Estimation of the wall-pressure spectrum from the pinhole microphone measurement. Reference wall-pressure spectrum from a DNS at  $Re_\tau = 2000$

### 7.2.2. Excitation of Single Helmholtz-Resonators

The results of the microphone measurements for TBL excitation of HRs are visualised in Figure 7.4. The numeric results are compared to those of acoustic excitation as shown in Table 7.2. In general, the measured resonance frequencies are higher for TBL excitation compared to acoustic excitation. Due to the grazing TBL, there is an effective convective velocity above the HR orifice. This requires a modification of the end correction as the flow above the resonator is no longer radiating into half-space – the main assumption for establishing the end correction. Effectively, the grazing TBL flow reduces the end correction, leading to a higher resonance frequency. However, no consistent modification to the end correction could be established that was applicable to all measurements.

For the nominal resonance and superresonance cases of both tested orifice diameters, damping is reduced with TBL excitation as compared to acoustic excitation, with a higher amplification factor. This is likely to be a result of the multiple HR excitation mechanisms – as outlined in §4.3 – simultaneously playing a role. The main excitation mechanism is from the wall-pressure fluctuations within the TBL. Additionally, there is always a degree of shear layer separation over the orifice, which through shear-layer resonance can further increase the resonance of the HR.

This theory initially does not seem to apply to the subresonance cases of both tested orifice diameters, with the damping significantly increased with TBL excitation compared to acoustic excitation. However, a downside of the noise-correcting method might become apparent here. With subresonance, significant coherence of 0.3 between the noise microphone signal and the cavity microphone signal is measured at the HR resonance frequency. Therefore, 30 % of the spectral energy at this frequency gets filtered out. However, the noise microphone may be picking up the HR resonance, meaning it is not actually background noise. For the nominal resonance and superresonance cases, the noise microphone is not picking up any considerable noise at this frequency – nor at that of the HR resonance frequency. Therefore, it appears that the subresonance cases show an artificially high damping and low amplification factor.

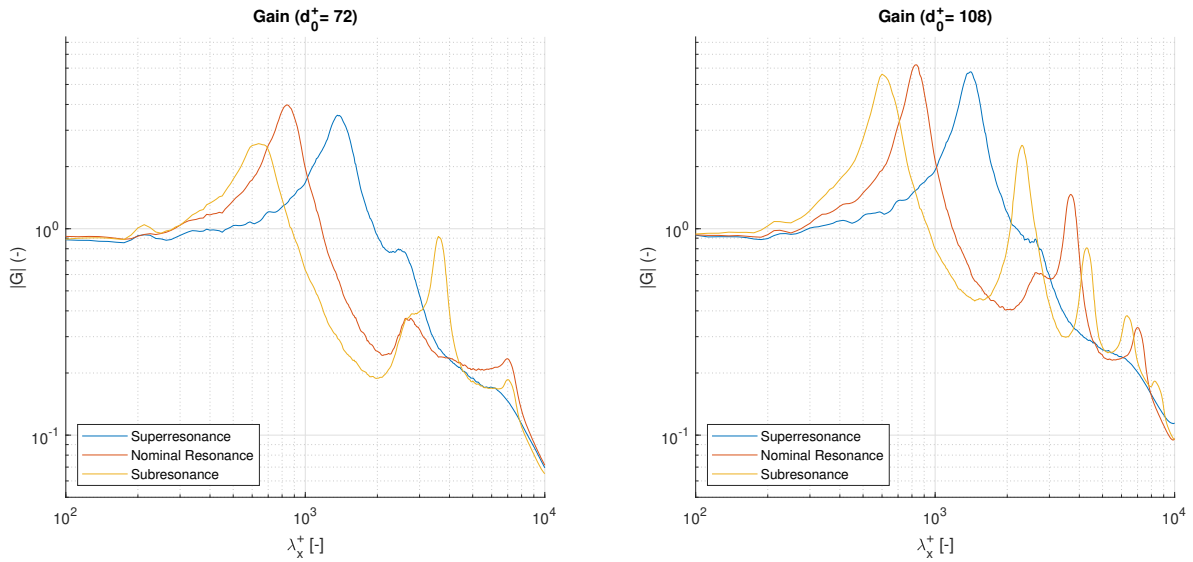


Figure 7.4: Phase and gain of the measured transfer function  $H_{HR}$  for the wind tunnel measurements of the tested HRs

$d_0$ [mm]	$d_0^+$ [-]	Resonance	TBL Excitation			Acoustic Excitation		
			$f_0$ [Hz]	$\xi$	$\alpha$	$f_0$ [Hz]	$\xi$	$\alpha$
2	72	Superresonance	1410	0.1464	3.41	1414	0.1948	2.57
		Nominal resonance	854	0.1260	3.97	827	0.1679	2.98
		Subresonance	665	0.1998	2.5	574	0.1258	3.97
3	108	Superresonance	1494	0.0814	6.14	1454	0.0996	5.02
		Nominal resonance	838	0.0754	6.63	791	0.0800	6.24
		Subresonance	623	0.0829	6.03	582	0.0620	8.04

Table 7.2: Summary of results from the microphone measurements during the wind tunnel tests. The measured resonance frequencies and damping result from the second-order model approximation fit of the measured transfer functions

Figure 7.5 shows how the measured transfer function gain compares to the predicted HR frequency and the corresponding overtones. The overtones are still predicted with high accuracy – and seemingly are not changed by TBL excitation compared to acoustic excitation. For the HR frequency, it appears to confirm the hypothesis that the TBL excitation effectively reduces the required end correction.

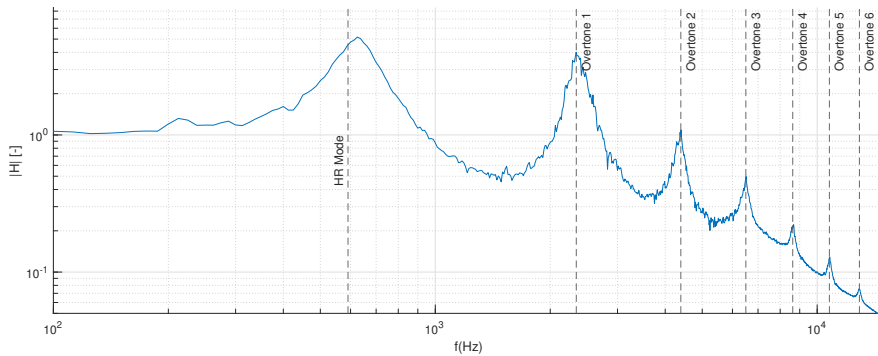


Figure 7.5: Transfer function gain as function of frequency for. Dotted lines indicate the calculated frequencies of the overtones. Wind tunnel measurements for single HR setup for  $d_0^+ = 108$ , subresonance

### 7.2.3. Remarks on Downstream Wall-Pressure Measurements

The downstream wall pressure is measured using the pinhole microphone 25 mm (900 $l^*$ ) downstream of the resonator. While small differences in the downstream wall pressure are measured, it is chosen

to omit them from the report. From the phase-averaged PIV measurements – which will be elaborated upon in §8.3.2 – it is found that the streamwise extent of the effects of the tested HRs on the TBL flow is smaller than  $900l^*$ . Therefore, it is considered that the observed changes in the measured downstream wall pressure are not a direct effect of the HR on the TBL flow.

#### 7.2.4. Remarks on the HR Array Measurements

The measurements from the HR array setup have been omitted from the report. In Figure 7.6 and Figure 7.7 the raw and noise-corrected energy spectra are shown for a streamwise line of 5 HRs. Figure 7.8 shows the corresponding second-order model fit for determining the HR resonance frequency. Compared to the measurements from the single HR setup, it stands out that from neither the raw or noise corrected energy spectra a very clear resonance peak can be distinguished. For the shown HRs, the HR resonance frequency is expected to be around  $f_0 = 850 \text{ Hz}$ . Furthermore, the magnitude of the HR response is significantly lower than what was achieved with the single HR setup. The measured transfer function  $H(f)$  appears significantly more noisy, with a lower achieved maximum gain.

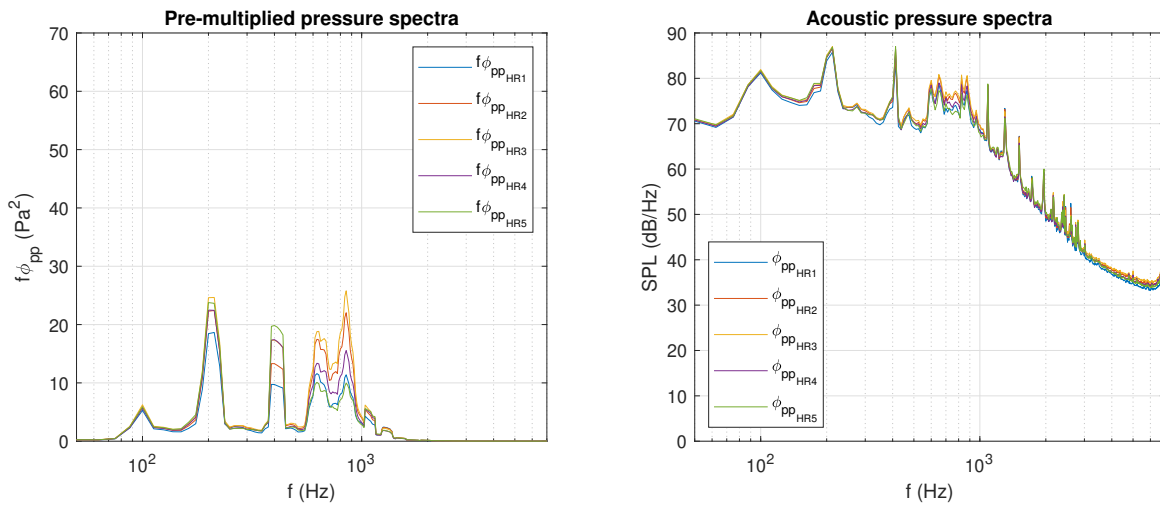


**Figure 7.6:** Non-corrected energy spectra calculated from the microphone measurements with  $N = 2^{12}$  for a streamwise line of 5 HRs of the HR array setup with  $d^+ = 72$ , nominal resonance

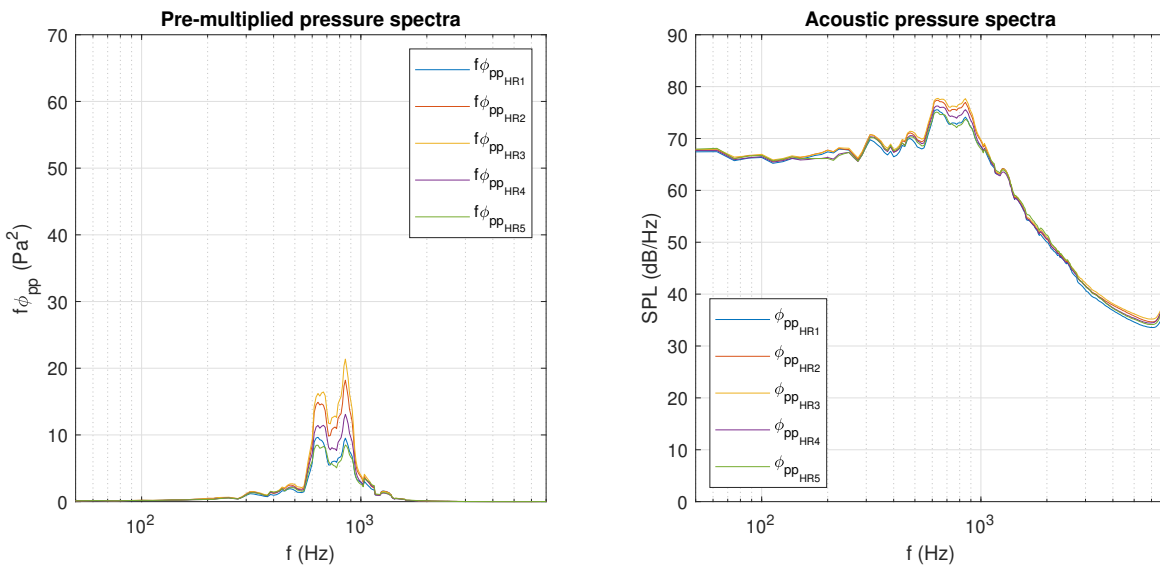


**Figure 7.7:** Noise-corrected energy spectra calculated from the microphone measurements with  $N = 2^{12}$  for a streamwise line of 5 HRs of the HR array setup with  $d^+ = 72$ , nominal resonance

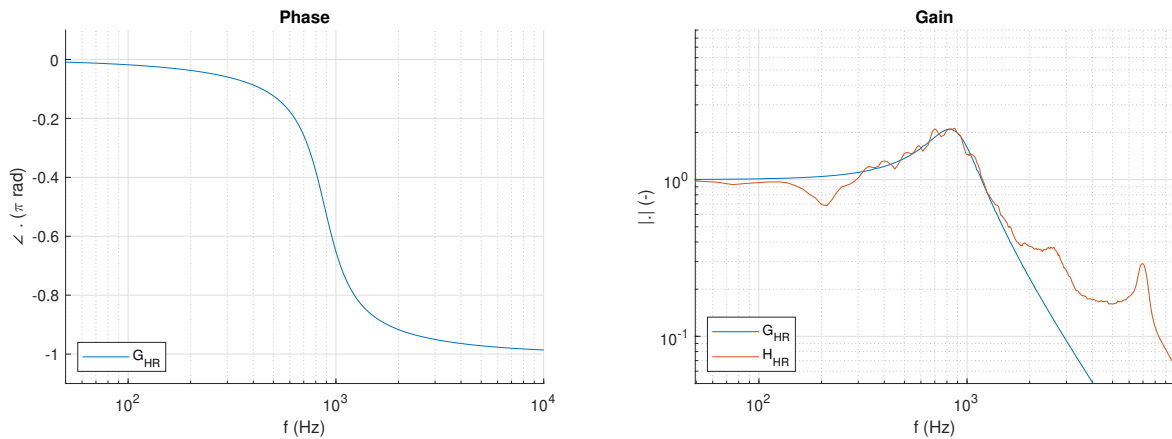


**Figure 7.8:** Experimentally obtained transfer function  $H$  via pinhole measurement, with the second-order model fitted transfer function  $G$ . Measurements from wind tunnel test for the first HR in a streamwise line of 5 HRs of the HR array setup with  $d^+ = 72$ , nominal resonance. Phase modulation implied from model as no experimental data is obtained with the used method

It is considered that the modularity of the HR array setup is the main contributor to the measured differences. With the use of the stack plates to control the cavity length, slight discontinuities are introduced in the HR cavities. Furthermore, despite the stack plates being clamped together, there might be a risk that the formed cavities are not completely airtight. This would allow for intercommunication between the HR cavities, which could negatively affect the results. While small differences were expected in the design phase of the experimental setup, the fundamental differences in response with the HR array setup were not anticipated.

For the above-mentioned reasons, it is considered that the measured results for the HR array setup will not give an accurate representation of the effect of a system of HRs. Furthermore, no direct comparison with the single HR setup is possible. Therefore, the results of the HR array setup will not contribute to the understanding of the working of HRs under a grazing TBL. The remainder of the report solely focuses on the results from the single HR setup.

# Results: Flow Measurements

This chapter presents the results of the hot-wire and PIV flow measurements for the single HR setup. First, the coherence between the HR cavity pressure and TBL flow from the hot-wire measurements is presented in §8.1 to show whether the intended pressure-velocity coupling is achieved. Subsequently, energy spectra of velocity fluctuations are presented in §8.2. The phase-averaged results for both hot-wire and PIV measurements are shown in §8.3. §8.4 presents the results of the quadrant analysis of the PIV measurements. In §8.5, the VITA analysis of the hot-wire measurements is shown, before in §8.6 the mean boundary layer statistics are presented.

## 8.1. Linear Coherence Spectra

Contour plots of the LCS between the HR cavity microphone signal and the hot-wire signal are shown in Figure 8.1. For the subresonance cases, coherence of up to 0.5 is measured in a frequency band of approximately 100  $Hz$  below and above the HR resonance frequency. It extends to a wall-normal location of  $y^+ = 25$ . This indicates that a significant pressure-velocity coupling is achieved between the HR cavity pressure and the streamwise velocity fluctuations of the grazing TBL flow. However, significant differences in the LCS are observed based on the frequencies of the tested HRs. With nominal resonance, the coherence is still apparent, but significantly weaker than with subresonance. With superresonance, no coherence between the HR and TBL flow is measured.

A potential explanation for the differences in LCS between the various tested frequencies can be found in the phase shift that is induced with the HR. The chosen frequencies were chosen such that with subresonance, a phase switch was induced between the HR and the TBL flow at the frequency of the most energetic  $v$ -fluctuations. It should be noted that this phase shift is measured at the bottom of the HR cavity, so it is not exactly known what the phase shift is at the exit of the HR. However, it is clear that subresonance – and to a lesser extent nominal resonance – induces a phase shift that is not induced with superresonance. Therefore, it appears that establishing a phase shift with the HR is required to achieve a clear pressure-velocity coupling between the HR cavity pressure and the streamwise velocity fluctuations of the TBL flow.

In the further interpretation of the results, it is assumed that the HR resonance only influences the TBL flow in those cases where a clear and apparent pressure-velocity coupling is achieved. This means that only the nominal resonance and subresonance cases for both orifice diameters indicate the effect of HR resonance on the TBL flow. In the absence of pressure-velocity coupling for the superresonance cases, these results are considered to primarily show the effect of an orifice in isolation. However, it should be noted that this remains an assumption that cannot be proven in the absence of a dedicated measurement of an orifice in isolation.

While the trends are similar between both presented orifice diameters, larger values for coherence are found for the HRs with orifice diameter  $d_0^+ = 108$  compared to the HRs  $d_0^+ = 72$ . This is considered to primarily be an effect of the increased amplification factors of these HRs, mostly attributed to the relative geometric differences – as discussed in §7.1. While the HR cavity pressure is measured at the bottom of the cavity, these results appear to confirm that a higher measured cavity pressure propagates to the exit of the HR, resulting in an increased pressure velocity coupling between the HR cavity pressure and the streamwise velocity fluctuations of the TBL flow.

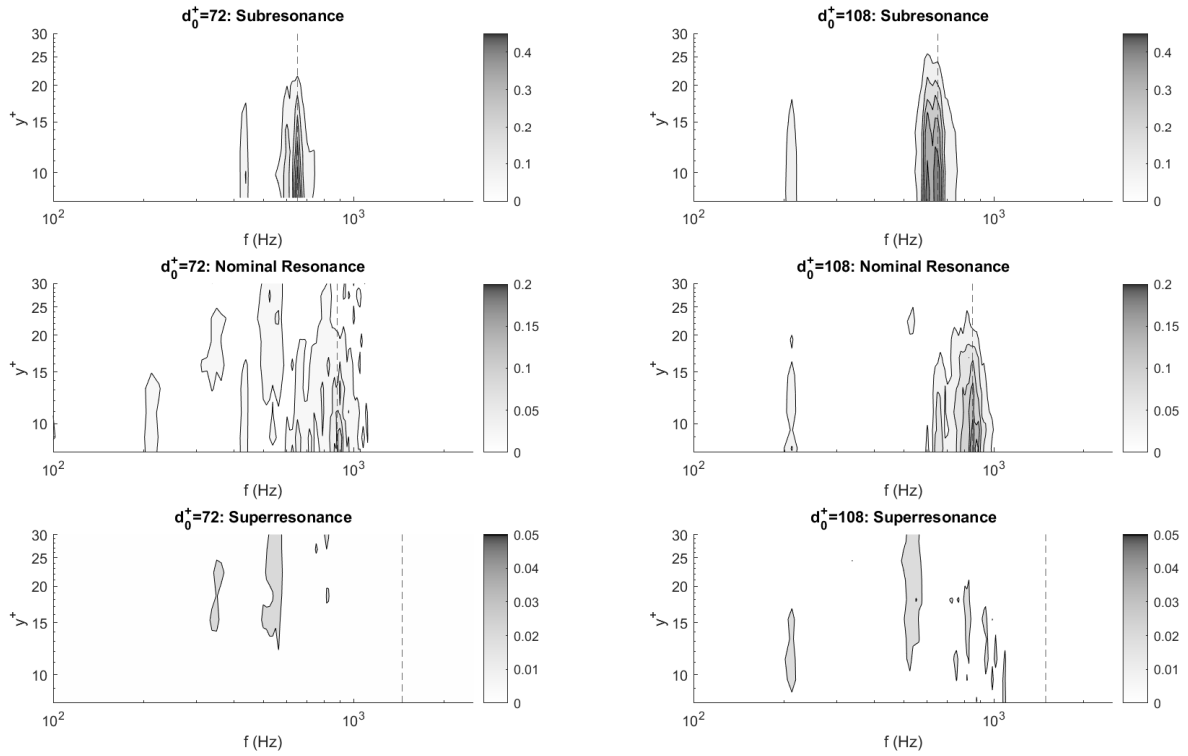


**Figure 8.1:** Contour plots of the LCS between the HR cavity microphone signal and the hot-wire measurements. Note the different colour scales for each row of plots that are used because of the large difference in coherence for the different resonance cases. Dotted lines indicate respective HR resonance frequencies

## 8.2. Spectral Analysis

The energy spectra of streamwise velocity fluctuations for the HRs with orifice diameter  $d_0^+ = 108$  are shown in Figure 8.2, while Figure 8.3 shows how the spectra have changed compared to the reference spectrum. Two clear regions of effect can be identified: 1) an increase in spectral energy at the wavelengths below  $\lambda_x^+ = 1000$  and 2) a decrease in spectral energy at higher wavelengths. The effects extend to a wall-normal distance of  $y^+ = 40$ , beyond which the spectra become similar to that of the reference measurement. The regions of effect are present for all three tested frequencies, but clear differences can be identified that are in line with the observations from the LCS.

For both nominal resonance and subresonance, the increase in spectral energy is centred around the HR resonance frequency, with the largest magnitudes of increase at the wall. With subresonance, larger increases in spectral energy are observed than with nominal resonance, which reflects the larger measured coherence between the HR cavity pressure and the TBL flow. The region of highly increased energy around the HR reference frequency appears to extend to approximately  $y^+ = 25$ , which is also consistent with the observations from the LCS.

With superresonance, the increase of spectral energy at lower wavelengths is not centred around the HR resonance frequency. This is according to expectation in the absence of coherence between the HR cavity pressure and the grazing TBL flow. Therefore, it appears that this increase in spectral energy is primarily the result from an orifice in isolation. It is likely an effect induced by the interaction of the shear layer with the edges of the orifice. When a coupling between the HR and the TBL is achieved, this effect gets amplified. Furthermore, the reduction in spectral energy at higher wavelengths is already present in the superresonance case, and also appears to get amplified in the cases of nominal reference and subresonance.

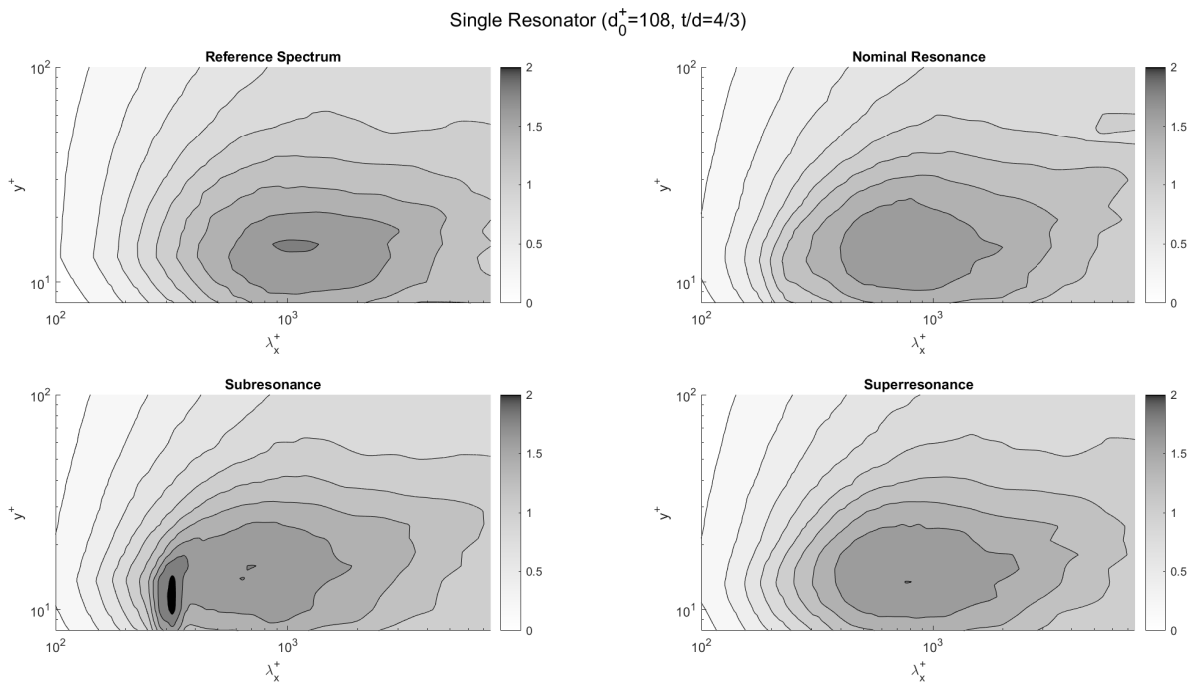


**Figure 8.2:** Energy spectra of streamwise velocity fluctuations from hot-wire measurements for the HRs with  $d_0^+ = 108$

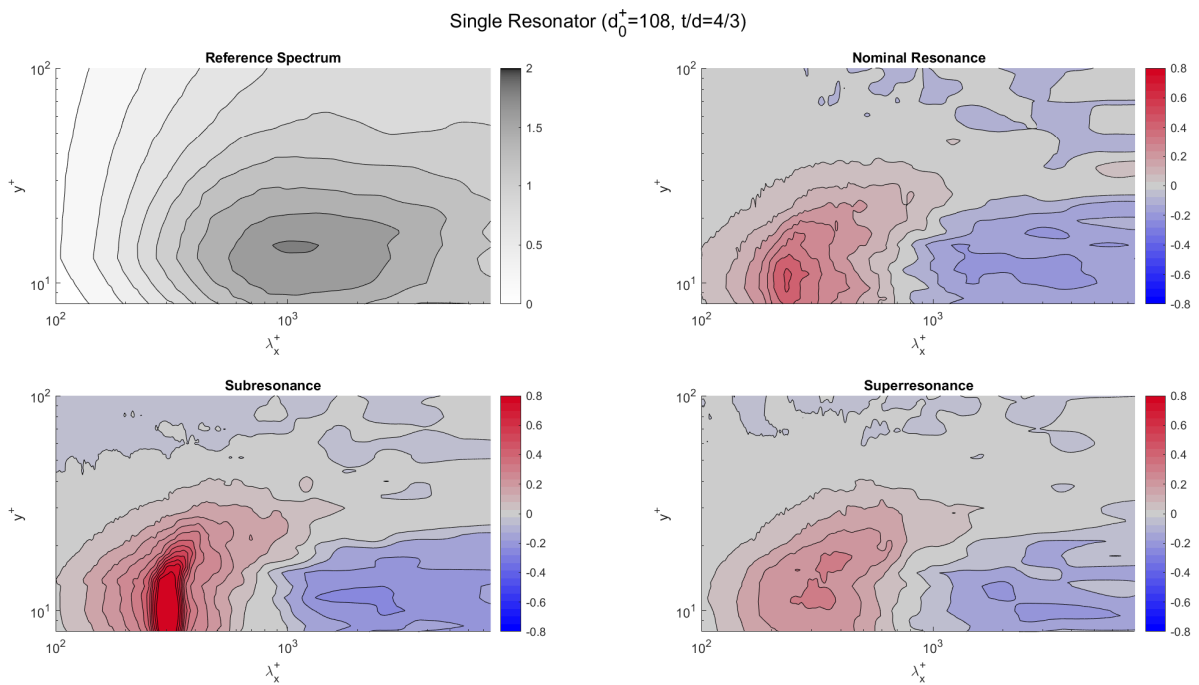


**Figure 8.3:** Energy spectra of streamwise velocity fluctuations shown as difference with respect to the reference energy spectrum for HRs with  $d_0^+ = 108$

The spectral differences for the HRs with orifice diameter of  $d_0^+ = 72$  are shown in Figure 8.4. While the general trends are similar to the HRs with  $d_0^+ = 108$ , the magnitude of the changes is considerably lower. Partially, this can be explained by the weaker resonance of these HRs, but is probably also influenced by the smaller orifice diameter. Comparing the superresonance cases between the different orifice diameters – neither showing coherence between the HR and the TBL flow – it can be seen that the effects are weaker and shifted to lower wavelengths with the smaller orifice diameter. This is an indication that there is less shear layer separation and reduced interaction of the shear layer with the edges of the orifice. Such an observation would be consistent with the findings of Silvestri et al. (2017a) who indicated reduced effectiveness of the used array beyond  $y^+ > 105$  due to the increase in shear layer separation.

Contrary to what was observed with the HRs with  $d_0^+ = 108$ , for the HRs with  $d_0^+ = 72$  there is less of a reduction in spectral energy at higher wavelengths when there is pressure-velocity coupling between the HR and the TBL flow. For the subresonance case, this region of reduced spectral energy has almost vanished.

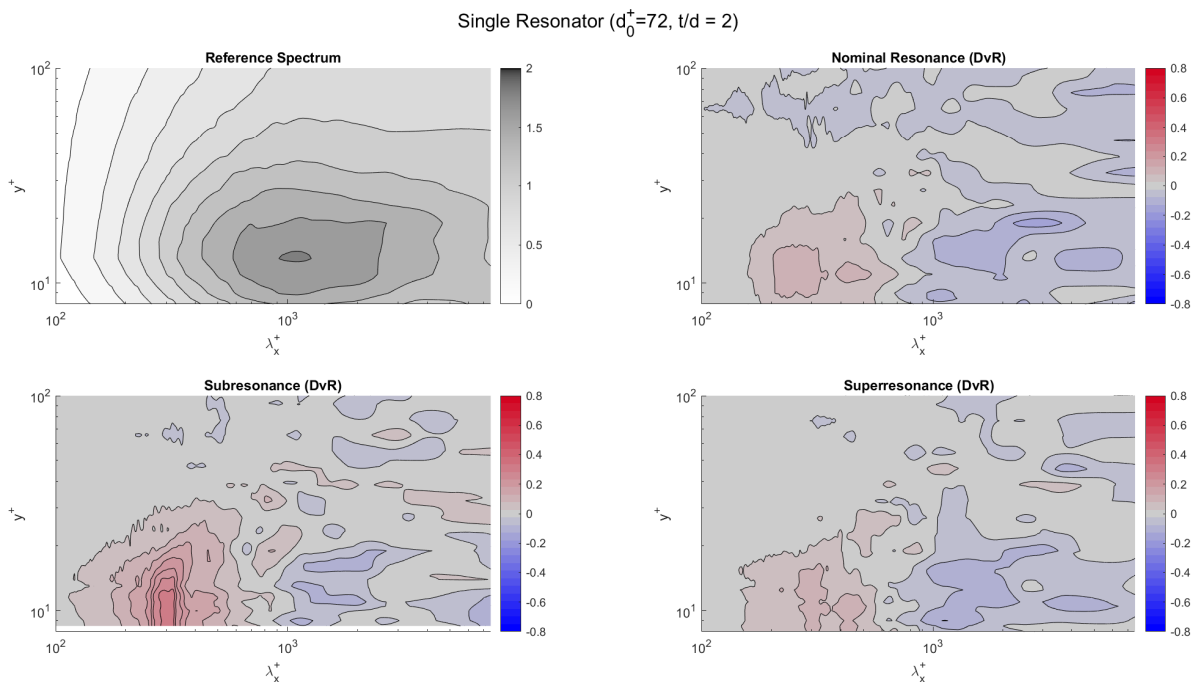


**Figure 8.4:** Energy spectra of streamwise velocity fluctuations from hot-wire measurements shown as difference with respect to the reference energy spectrum for HRs with  $d_0^+ = 72$

### 8.3. Phase-Averaged Measurements

This section presents the phase averaged flow measurements. First, the phase averaged hot-wire measurements are shown in §8.3.1. Subsequently, the phase-averaged PIV measurements are presented in §8.3.2.

#### 8.3.1. Phase-Averaged Hot-Wire Measurements

The phase-averaged streamwise velocity fluctuations from the hot-wire measurements are shown in Figure 8.5. Clear phase interlocking between the HR and TBL layer is observed for the subresonance and nominal resonance cases, most evident below  $y^+ = 25$ . In this region, the relative phase between the HR and TBL flow effects reduces gradually. This is indicative that there is an inflow/outflow effect from the HR that is propagating upwards into a region of mean shear, which then subsequently influences the streamwise velocity. Beyond  $y^+ = 25$ , the phase-averaged effects are significantly smaller and the relative phase stays approximately constant. This is in line with the observations from the LCS, which shows no more coherence between the HR and TBL flow beyond  $y^+ = 25$ .

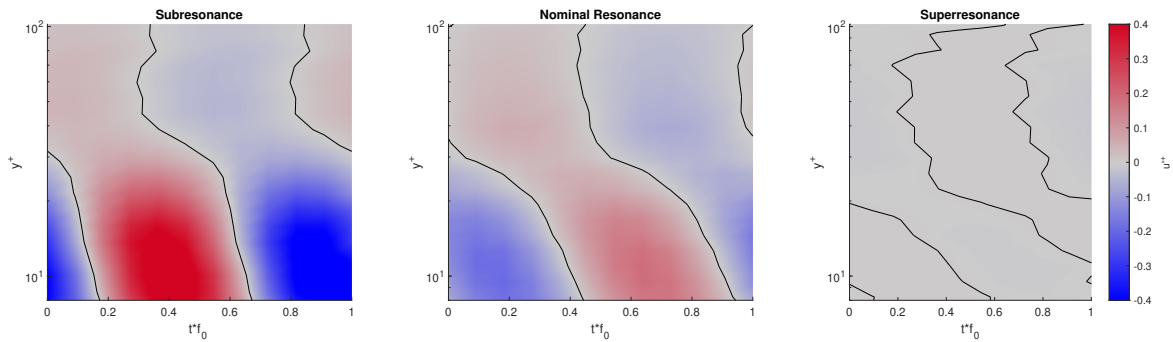


**Figure 8.5:** Phase-averaged streamwise velocity fluctuations for the HRs with  $d_0^+ = 108$ . Black contour lines indicate zero streamwise velocity fluctuations

The difference in magnitude of effects can be explained by the smaller coherence for the nominal resonance case. Some slight differences appear between the phase-averaged results for the subresonance and nominal resonance, judging from the zero-contours. The offset in phase angle close to the wall could be ascribed to the different cavity lengths of the two HRs. As the HR cavity pressure is measured at the bottom of the cavity, this could show up as an inherent phase offset in the phase averaged results. The steeper inclination of the contours of zero velocity fluctuations is purely an artefact of the different scales used for the plots, which are based on one cycle of resonance of each HR.

### 8.3.2. Phase-Averaged PIV Measurements

The phase-averaged PIV measurements give an insight into the 2D flow effects of the HR resonance. Figure 8.6 shows how the 6 bins correspond to which part of one cycle of HR resonance. Then, Figure 8.7, Figure 8.8 and Figure 8.9 show the averages over half a cycle of HR resonance for both the local  $u$ -fluctuations and  $v$ -fluctuations. A propagating pattern of regions of inflow and outflow of the resonator can be identified from the  $v$ -fluctuations. The effects of inflow and outflow appear to propagate up to larger wall-normal distances up to  $y^+ = 90$  and potentially beyond.

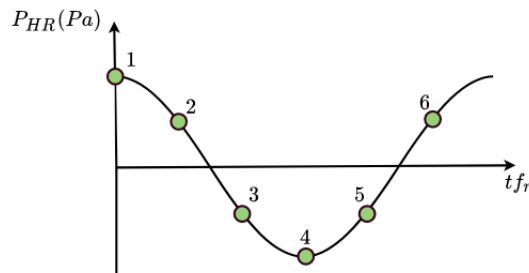


**Figure 8.6:** Placement of the phase-averaging bins over one cycle of HR resonance

The changes in  $u$ -fluctuations over the HR appear to be closely coupled to these regions of inflow and outflow observed in the  $v$ -fluctuations. Whenever there is an inflow into the HR, this is accompanied by an area of increased streamwise velocity. An outflow from the HR then seems to correspond to a reduced streamwise velocity.

The downstream propagation of the changes in  $u$ -fluctuations appears to provide a further understanding of what was observed in the phase-averaged hot-wire measurements. Focusing on Figure 8.7, the largest influenced region is up to  $y^+ = 25$ , beyond which the effects still seem apparent but convected further downstream. While the effects appear cyclic directly at the exit of the HR, only one full cycle can be identified downstream. This seems to be an indication of the streamwise extent of the effects of the analysed case.

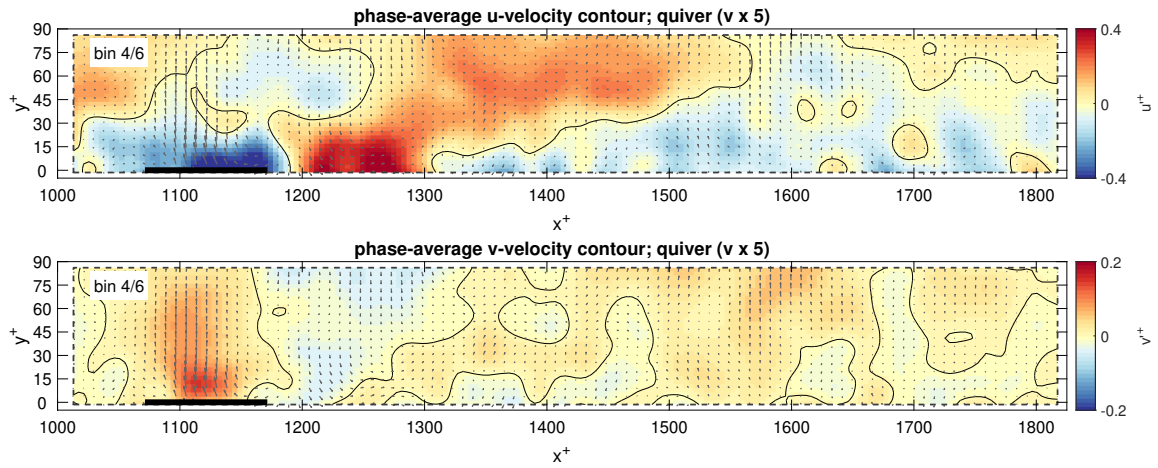


**Figure 8.7:** Bin-average contour plots of velocity fluctuations for bin 4 out of 6 for the single HR setup at  $d_0^+ = 108$ , subresonance. Black line indicates the location of the HR orifice

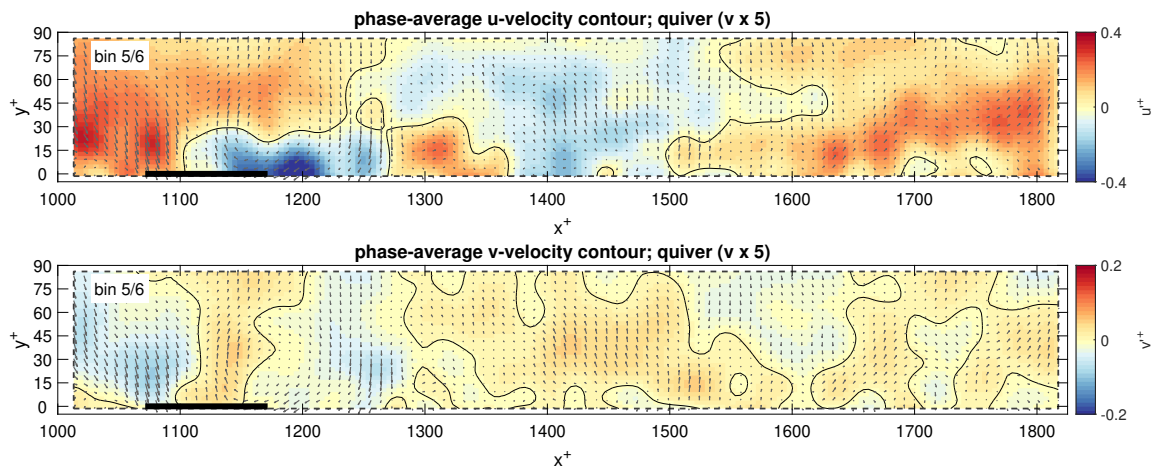


**Figure 8.8:** Bin-average contour plots of velocity fluctuations for bin 5 out of 6 for the single HR setup at  $d_0^+ = 108$ , subresonance. Black line indicates the location of the HR orifice

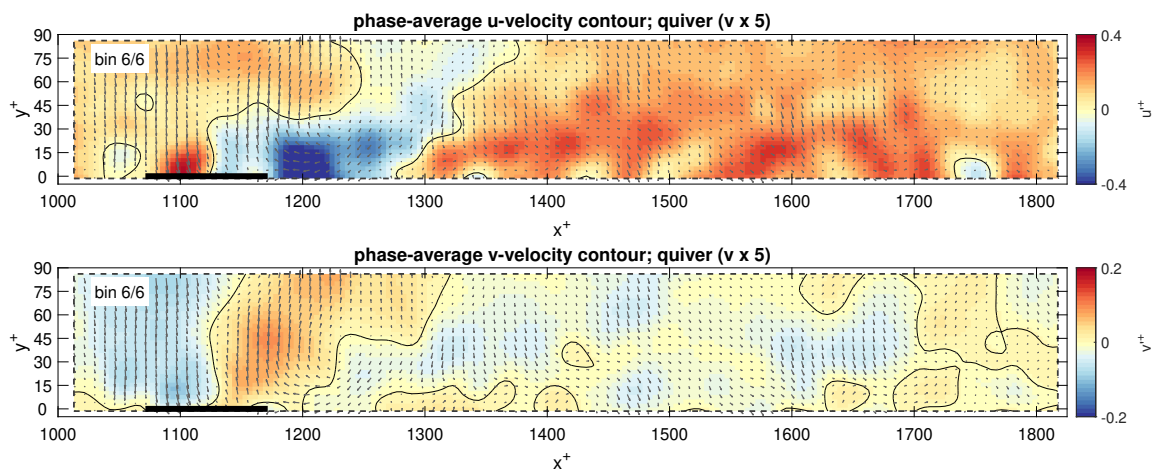


**Figure 8.9:** Bin-average contour plots of velocity fluctuations for bin 6 out of 6 for the single HR setup at  $d_0^+ = 108$ , subresonance. Black line indicates the location of the HR orifice

In Figure 8.10, Figure 8.11 and Figure 8.12, a single bin is shown for the cases of subresonance, nominal resonance and superresonance. In all three cases, cyclic effects appear to be present. However, in each case, the streamwise extent of the cycles appears different. It was identified that the streamwise extent is related to the frequency of resonance of the HR. The dotted lines in each of the figures represent the streamwise extent of half a period of resonance. With increasing HR resonance frequency, the streamwise extent of the cycles of inflow and outflow reduces.

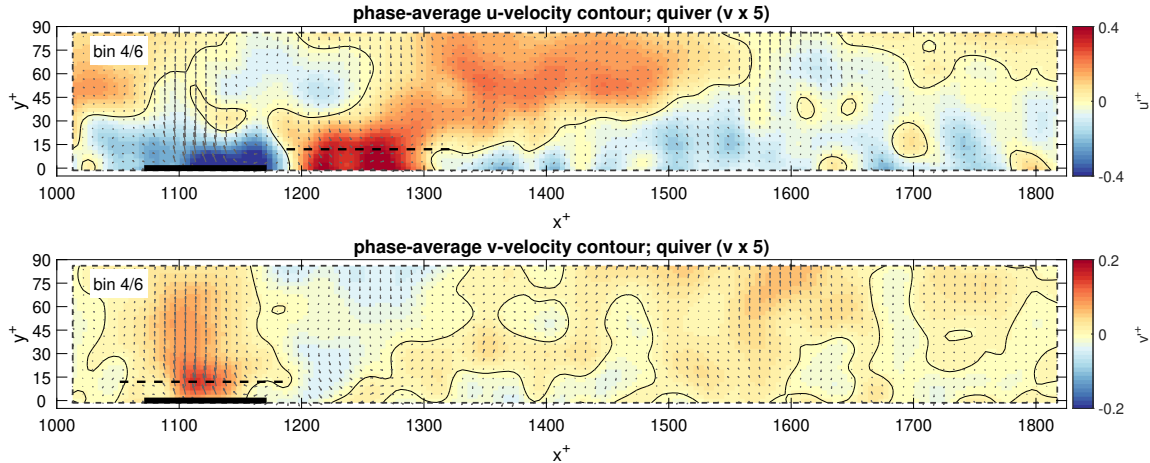


**Figure 8.10:** Bin-average contour plots of velocity fluctuations for bin 4 out of 6 for the single HR setup at  $d_0^+ = 108$ , subresonance. Black line indicates the location of the HR orifice. Dotted lines indicate streamwise length scale of resonance

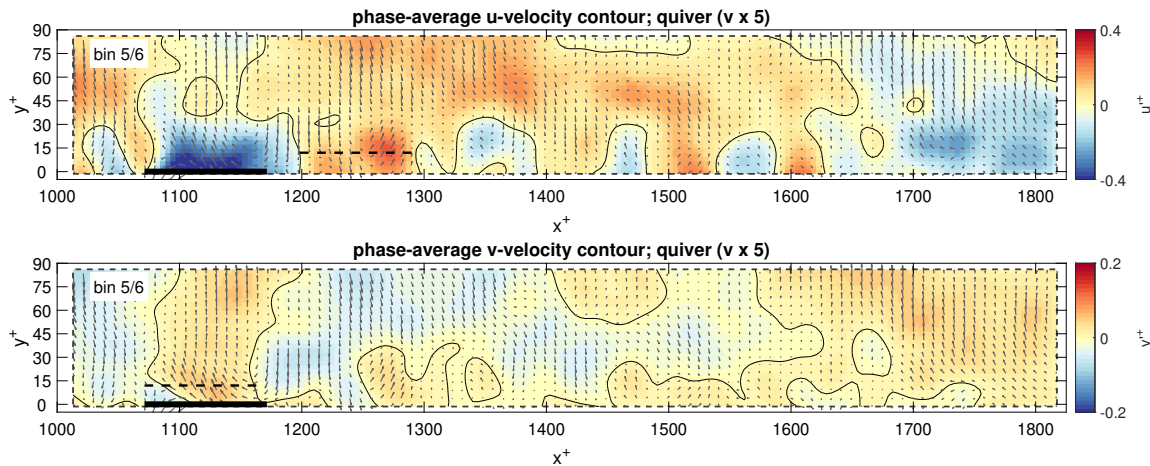


**Figure 8.11:** Bin-average contour plots of velocity fluctuations for bin 5 out of 6 for the single HR setup at  $d_0^+ = 108$ , nominal resonance. Black line indicates the location of the HR orifice. Dotted lines indicate streamwise length scale of resonance

As expected from the earlier presented results, the strongest effects on the TBL flow are present for the subresonance case. For the subresonance and nominal resonance cases, the cyclic inflow and outflow appear to be strong enough to also influence the streamwise velocity. Where for the subresonance case a full cycle of downstream effects appears to be present, the nominal resonance case does not show a full coherent cycle of effects downstream. This then indicates a reduced streamwise extent of the downstream effects for the nominal resonance case.

For the superresonance case, there are small signs of narrow bands of inflow, but the results are noisier than for the subresonance and nominal resonance cases. Furthermore, there doesn't seem to be any effect of these inflow and outflow cycles on the streamwise velocity.

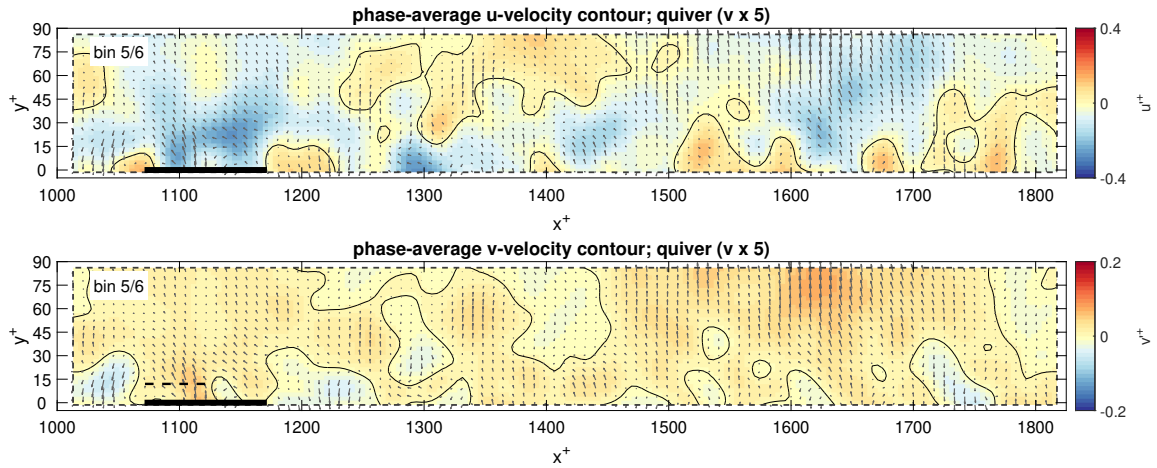


**Figure 8.12:** Bin-average contour plots of velocity fluctuations for bin 5 out of 6 for the single HR setup at  $d_0^+ = 108$ , superresonance. Black line indicates the location of the HR orifice. Dotted lines indicate streamwise length scale of resonance

### 8.4. Quadrant Analysis

For the HRs with  $d_0^+ = 108$ , the JDPF of velocity fluctuations from the quadrant analysis are presented in Figure 8.13. Due to the cyclic bands of inflow and outflow, the  $v$ -fluctuations shift towards higher values. Despite the phase-interlocking of the streamwise velocity, no significant changes in the  $u$ -fluctuations are observed.

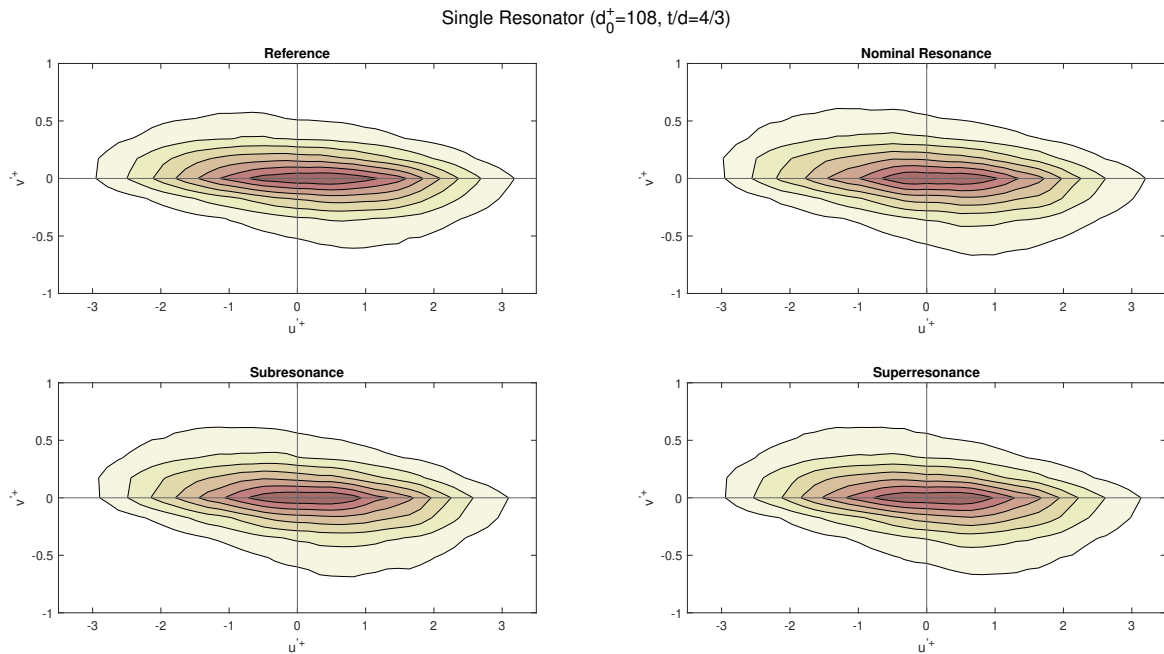


**Figure 8.13:** JPDF of velocity fluctuations from quadrant  $uv$ -decomposition between  $15 < y^+ < 35$  for the single HR setup with  $d_0^+ = 108$ .

The WJPDF of velocity fluctuations is shown in Figure 8.14, in which each entry in the JDPF is premultiplied with the magnitude of the respective velocity fluctuations  $u'^+$  and  $v'^+$ . The values in the WJPDF give an indication of the relative strength of the events in each quadrant. For all cases, an increase in the relative strength of the events in Q2 and Q4 is observed. Meanwhile, the relative strength of

the events in Q1 and Q3 seem to have reduced slightly. These observations would indicate a relative increase in the production of turbulence.

These effects are already present in the superresonance case, indicating that this is partially an effect of just the presence of the orifice. However, these effects appear to be amplified for the nominal resonance and superresonance cases. This could be mainly a result of the cyclic bands of inflow and outflow out of the HR. These shift the  $v$ -fluctuations towards higher magnitudes, resulting in an apparent increase in the strength of Q2 and Q4 events.

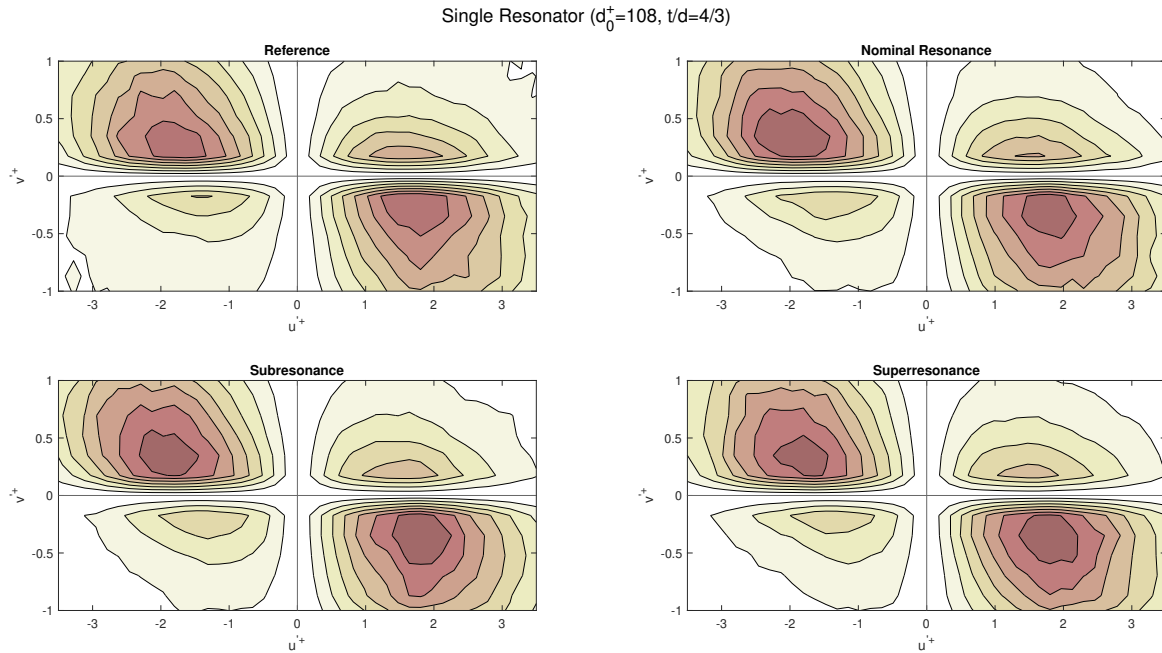


**Figure 8.14:** WJPDF of velocity fluctuations from quadrant  $uv$ -decomposition between  $15 < y^+ < 35$  for the single HR setup with  $d_0^+ = 108$

## 8.5. VITA Analysis

The results for the VITA analysis of sweep events for the single HRs with  $d_0^+ = 72$  and  $d_0^+ = 108$  are shown in Figure 8.15 and Figure 8.16 respectively, with the average events shown in Figure 8.17. For the HRs with  $d_0^+ = 72$ , no significant changes in the VITA events are observed. For the HRs with  $d_0^+ = 108$ , the main changes can be seen in the 'tails' of the VITA events. For all resonance cases, the 'tails' approach zero fluctuations sooner than the reference measurement.

Furthermore, for the HRs with  $d_0^+ = 108$ , significantly more VITA events are detected compared to those with  $d_0^+ = 72$ . This could be an indication of the shear layer separation becoming worse with larger orifice diameters – an observation that also appeared from the spectral analysis results. This shear layer separation results in coherent spanwise rollers- travelling downstream. These may then be detected by the VITA analysis as 'sweep-like' events. This then may result in a large increase in detected events, without the sweep events being fundamentally modified themselves.

Between each of the resonance cases, no significant differences are observed. This seems to indicate that the found effects are merely an effect of the orifice and that the resonance of the HRs has no significant impact on the intensity or duration of the analysed VITA events. This result is somewhat surprising, as the time scale of an individual VITA event is close to the timescale of the nominal resonance case - with the subresonance and superresonance still in the same order of magnitude.

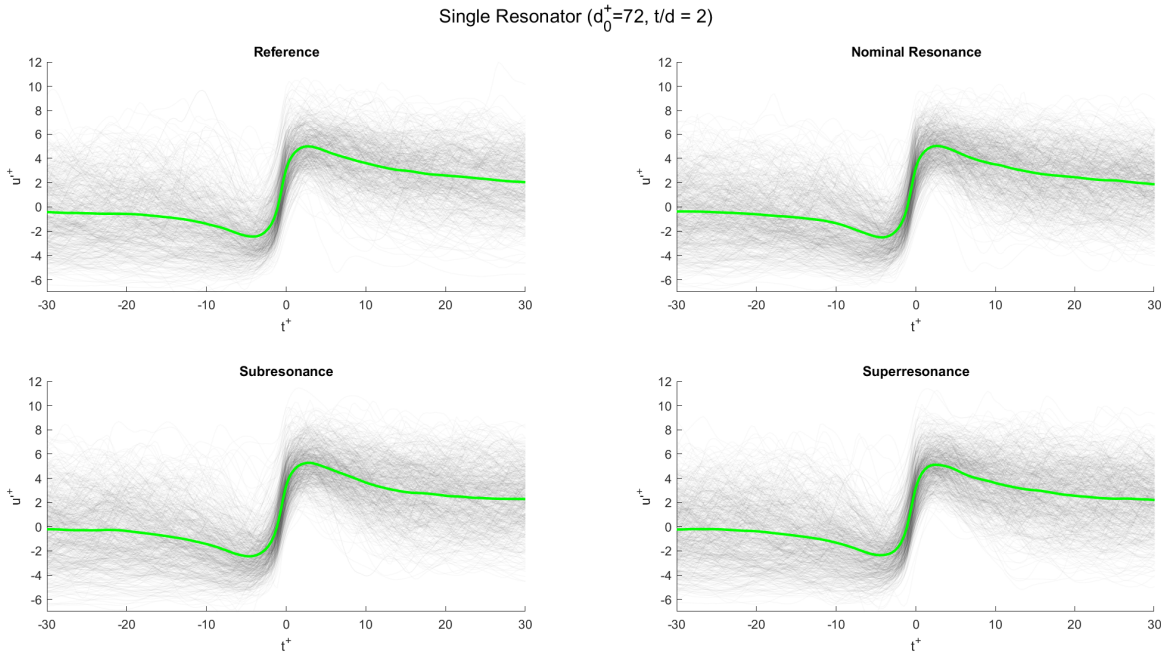


Figure 8.15: VITA analysis for sweep events for the single HR setup with  $d_0^+ = 72$  at  $y^+ = 15$

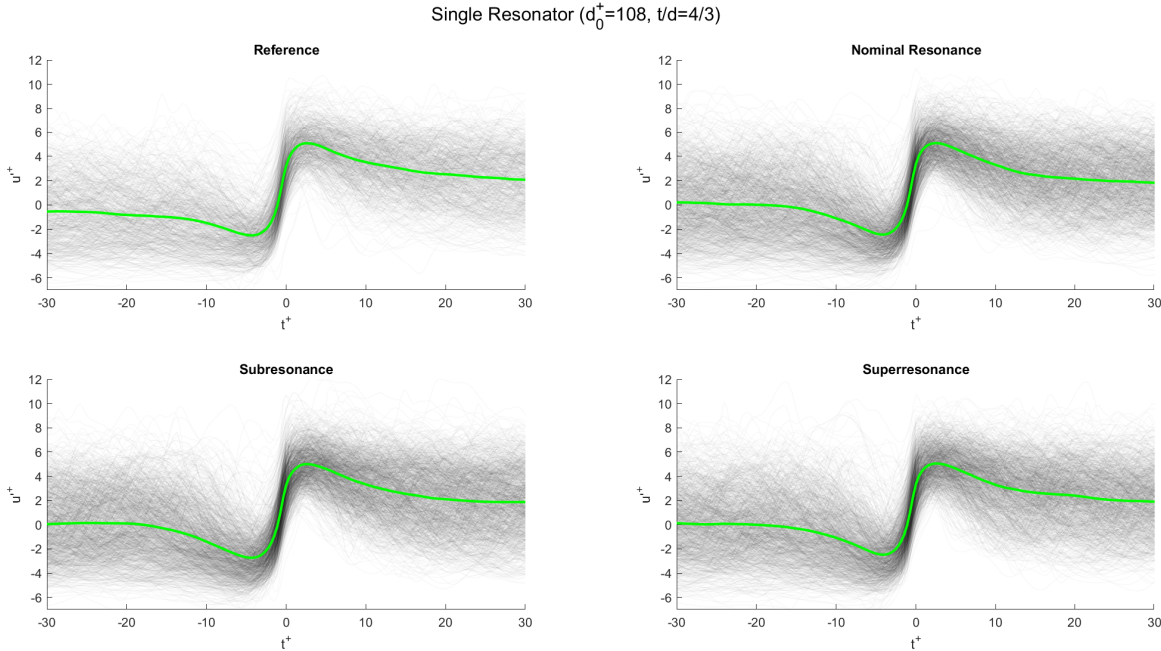


Figure 8.16: VITA analysis for sweep events for the single HR setup with  $d_0^+ = 108$  at  $y^+ = 15$

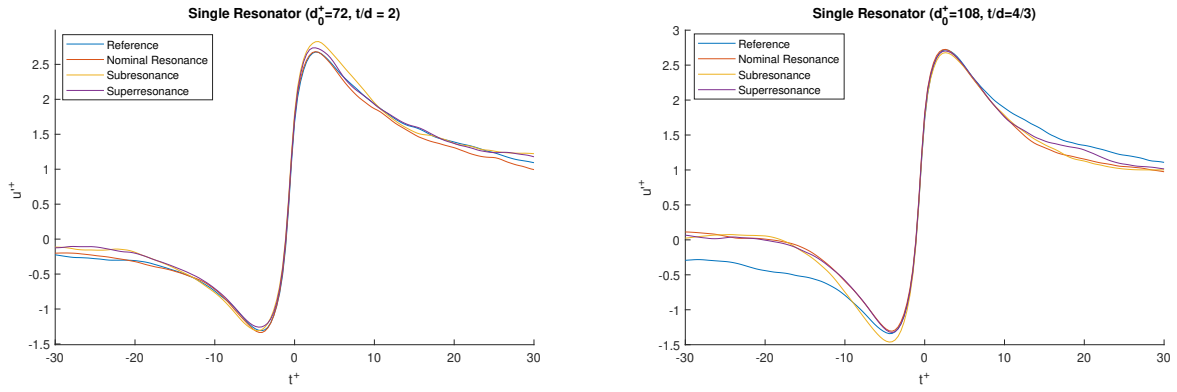


Figure 8.17: Averaged VITA events for the single HR setup with  $d_0^+ = 72$  and  $d_0^+ = 108$  at  $y^+ = 15$

It should be noted that the VITA analysis considers all local high-variance events with a high change in velocity fluctuations. This local variance is then compared to the overall signal variance. Therefore, it is not the most robust technique for analysing the effect on the near-wall cycle events. As seen, potentially, the effects of shear layer separation and the spanwise rollers are visible in the results of the VITA analysis.

### 8.6. Mean Boundary Layer Statistics

In Figure 8.18 and Figure 8.19, the mean boundary layer statistics from the hot-wire measurements are plotted for the HRs with  $d_0^+ = 72$  and  $d_0^+ = 108$  respectively. The observed effects are small in magnitude. For the mean boundary layer profile, a small velocity deficit is observed between  $y^+ = 15$  and  $y^+ = 40$ , which is most apparent for the HRs with  $d_0^+ = 108$ . However, there are no clear differences in the mean profiles for the cases with nominal resonance, subresonance and superresonance. This appears to indicate that the changes in the mean profile are mostly an effect of the orifice in isolation. The pressure-velocity coupling that is achieved with nominal resonance and subresonance does not show to significantly affect the mean profiles.

Small changes in the variance are measured. As the tested HRs appear to increase the spectral energy at low wavelengths and decrease the energy at higher wavelengths, these cancel out when calculating the overall variance. Therefore, the variance or turbulence intensity is not a useful measure for analysing the effect of HRs.

It appears that the primary effect on the mean statistics arises from the presence of the orifice in the flow. Despite significant pressure-velocity coupling between the HR and the grazing TBL flow, the mean statistics show no significant differences. This indicates that the effects of the HR on the grazing TBL flow are primarily cyclic effects coupled to the phase of the HR resonance. However, in the mean statistics, these effects even out mostly.

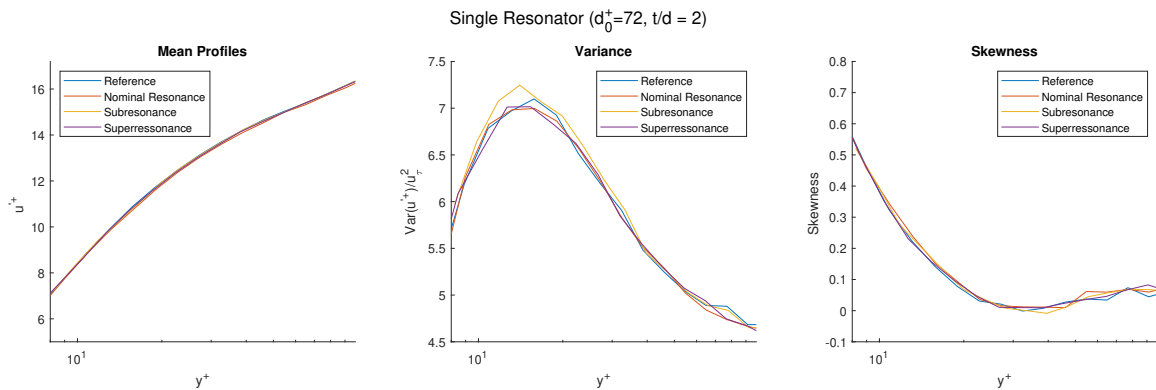


Figure 8.18: Mean boundary layer statistics from the hot-wire measurements for the HRs with  $d_0^+ = 72$

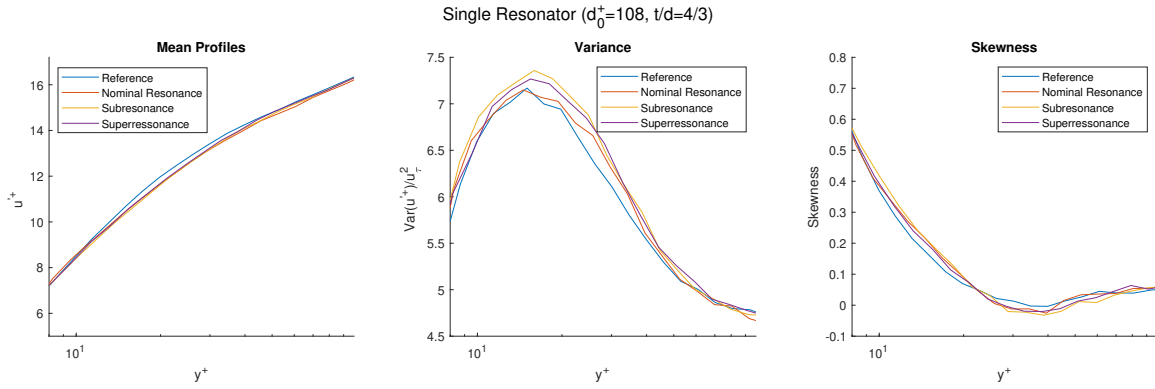


Figure 8.19: Mean boundary layer statistics from the hot-wire measurements for the HRs with  $d_0^+ = 108$

The mean profiles from the PIV measurements for the HRs with  $d_0^+ = 108$  are shown in Figure 8.20. Similarly to the hot-wire measurements, a velocity deficit is measured in the buffer layer. However, the velocity deficit is seen at lower  $y^+$ . Where the hot-wire measurements indicate a velocity deficit between  $15 < y^+ < 40$ , the PIV measurements show this velocity deficit to be between  $9 < y^+ < 25$ .

Similar to the hot-wire measurements, no significant difference between the resonance cases is identified. This further confirms the hypothesis that the mean effects observed primarily arise from the orifice in isolation, with the HR resonance not affecting the mean statistics significantly.

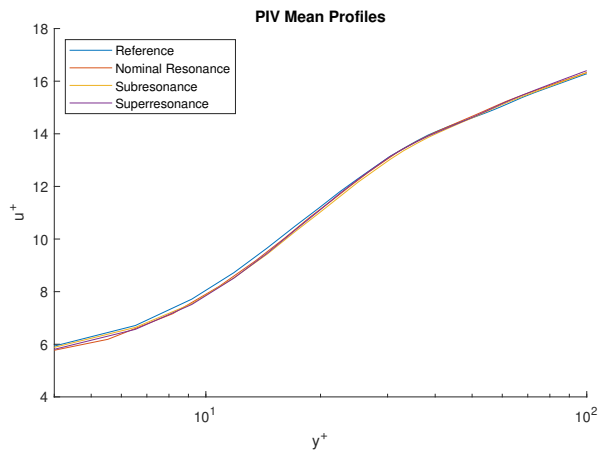


Figure 8.20: Mean boundary layer statistics from the PIV measurements for the HRs with  $d_0^+ = 108$

# Discussion

This chapter discusses the results and aims to compare them to the results of past experiments and the theoretical frameworks that the current experimental study is based upon. First, the excitation of HRs is discussed in §9.1, after which the pressure-velocity coupling between the HR and the grazing TBL flow is discussed in §9.2. Subsequently, the distinction between mean and instantaneous effects is discussed in §9.3, with remarks on the effect on the near wall-cycle made in §9.4. §9.5 elaborates on the potential uses for HRs as a TBL flow control method, before in §9.6 some final remarks are made on how well the research questions could be answered with the current experimental campaign.

## 9.1. Excitation of Helmholtz-Resonators

In §4.3, the various potential excitation methods for HRs were outlined. Excitation through shear layer resonance and incident pressure waves were identified. In the present study, it was attempted to primarily use the incident pressure waves from the grazing TBL flow as excitation method for HRs, with the orifice diameter small enough to prevent detrimental effects from shear layer separation – as according to the micro-cavity array study of Silvestri et al. (2017*a*). The aim was to then achieve destructive interference of the incoming pressure waves, akin to the working principle of noise-suppressing acoustic liners that are tuned to the blade-passing frequency of turbofan engines.

The acoustic characterisation of the tested HRs from the single HR setup in the anechoic chamber showed the response of HRs to a broadband noise signal. This confirmed the equations as used by Panton and Miller (1975*b*) for both the HR resonance frequency and the frequency of the overtones. In these equations, the end correction as proposed by Ingard (1953) was applied. The geometry and modularity of the single HR setup did not affect the acoustic response of the HRs. However, the modularity of the HR array setup did appear to have detrimental effects on the working of the HRs.

There are signs that the tested HRs were excited by a combination of both the incident pressure waves from the grazing TBL and shear layer interaction. This became apparent as larger amplification factors were found with TBL excitation. Furthermore, the presence of shear layer interaction was supported by the hot-wire measurements. From the superresonance cases – where no coherence was found – already a region of increased spectral energy was found at low wavelengths. This region was stronger with increasing orifice diameter, indicating increased shear layer separation and thus increased apparent shear layer interaction for the excitation of HRs. Also, the VITA analysis showed a similar suggestion. Downstream of all HRs an increase in high-variance, sweep-like events were detected, with the larger orifice diameters showing a larger increase in detected VITA events. As the results were very similar for all resonance cases, it is judged that this is likely to be purely an effect of the orifice geometry rather than a resonance effect. The likely explanation is then that it is a result of shear layer separation.

There are no apparent signs that destructive interference of the incoming pressure waves is achieved. While small changes in the measured downstream wall pressure were measured, the measurement location was at a downstream location beyond the streamwise extent of the effects that were found using the PIV measurements. Therefore, the measured changes are considered to not be a direct result of the HR resonance. On the contrary, there are signs of a loud tone developing, akin to the shear layer edge tone. For the strongest resonance cases, there are small signs that the HR resonance peak is also picked up by the noise microphone – which has shown to potentially skew some of the results.

Direct comparison between the tested HRs with different orifice diameters is not trivial. Due to the desire to test a large range of parameters in a modular setup, no two HRs had the same relative dimensions. For instance, changes in orifice diameter are always coupled with a change in the ratio of neck length to orifice diameter. Therefore, all indicated effects of increasing orifice diameter are only indicative, and may be the compound effect of both changes. It is considered that the reduced damping of the HRs with  $d_0 = 3 \text{ mm}$  compared to  $d_0 = 2 \text{ mm}$  is primarily a result of smaller friction losses due to the smaller ratio of neck length to orifice diameter. The increased shear layer separation is then ascribed to the increase in orifice diameter primarily, as this has been shown before in various studies. However, it needs to be confirmed whether these considerations are valid in a pure isolated parameter study.

## 9.2. Pressure-Velocity Coupling with Helmholtz-Resonators

One of the main findings of the present study is that a strong pressure-velocity coupling between the HR and the grazing TBL flow can be established, as well as how this pressure-velocity is influenced by the choice of the HR resonance frequency. Strong pressure-velocity coupling with a coherence of up to 0.5 was found when the HR resonance frequency was chosen to be lower than the frequency of the most-energetic  $v$ -fluctuations (subresonance). When the HR resonance frequency was chosen higher than the frequency of the most energetic  $v$ -fluctuations (superresonance), there were no signs of any pressure-velocity coupling. It should be noted that the coherence was only calculated for the streamwise velocity measurements from the hot wire. From the phase-averaged PIV measurements, small tentative signs of small bands of inflow and outflow were observed for the superresonance case, albeit to a much smaller extent than for the nominal resonance and subresonance cases. However, these small bands of inflow and outflow did not seem to have any influence on the streamwise velocity.

Two potential reasons for the large differences in pressure-velocity coupling were identified: 1) the induced phase switch by the HRs and 2) the relative size of the orifice with respect to the HR resonance frequency. One of the main differences between the subresonance cases and the superresonance cases is whether or not the HR induces a phase switch with respect to the frequency of the most energetic  $v$ -fluctuations. The subresonance HRs do, while the superresonance HRs do not. With an inherent phase difference present between the pressure and  $v$ -velocity in a TBL (de Koning, 2021), this might be a crucial aspect of achieving the pressure-velocity coupling in the TBL. The second potential reason is that with superresonance several cycles of inflow and outflow occur over the distance of the orifice, of which there were indications in the phase-averaged PIV images. Therefore, the cycles of inflow and outflow could cancel each other out, resulting in reduced or no pressure-velocity coupling achieved.

For the latter theory, Table 9.1 shows the length and timescales of resonance for the tested HRs. For the superresonance case of the HR with  $d_0 = 3 \text{ mm}$ , half a period of resonance corresponds to half of the orifice diameter. Therefore, both a full inflow and outflow cycle are present over the distance of the orifice. However, with  $d_0$  half a period of resonance spans almost the entire orifice. Both cases show no signs of pressure-velocity coupling between the HR and the TBL flow in the LCS. Therefore, it is unlikely that this theory is an accurate explanation for the observations.

$d_0 = 2 \text{ mm}$	$f_0 [\text{Hz}]$	$T [\text{ms}]$	$x_{T/2} [\text{mm}]$	$d_0 = 3 \text{ mm}$	$f_0 [\text{Hz}]$	$T [\text{ms}]$	$x_{T/2} [\text{mm}]$
Subreso- nance	665	1.50	3.76	Subreso- nance	623	1.54	3.85
Nominal resonance	854	1.17	2.93	Nominal resonance	837	1.18	2.95
Superreso- nance	1410	0.71	1.77	Superreso- nance	1494	0.67	1.68

**Table 9.1:** Length and time scales of resonance for the tested HRs

For the nominal and subresonance cases, half a wavelength of HR resonance either matched or was larger than the orifice diameters. It is not known whether this could have affected the established pressure-velocity coupling between the HRs and the TBL flow. Further parameter studies are required to quantify this.

### 9.3. Mean and Instantaneous Effects

Throughout the analysis of the results, a constant distinction was made between mean effects and instantaneous effects during a period cycle of resonance of the HRs. Most of the found mean effects were ascribed to be resulting from the presence of the orifice rather than the HR resonance. This was concluded based on the fact that the mean effects were present in all HR resonance cases and only showed a very slight difference between resonance cases. Furthermore, since the effects were also present in the superresonance case – without any coherence – it can be considered that these effects are not in any way related to the HR resonance. However, a reference measurement of the orifice in isolation – without any cavity – would be required to confidently make this conclusion.

No significant mean effects of HR resonance on the TBL flow were found. Therefore, also no clear conclusion can be made on the effect of the HRs on skin friction. The zoomed-out FOV for the PIV is not spatially resolved enough and the wall-positioning methods are not accurate enough to present a clear cut conclusion. Within the margins of error, the mean boundary profile can be shifted such that either a decrease or increase in skin friction is measured.

It should also be noted that, eventually, the study has been focused primarily on the effects of a single HR. In contrast, the micro-cavity array study of Silvestri et al. (2017a) has only considered a full array of cavities. Therefore, it is to be expected that the micro-cavity array shows larger effects on the mean boundary layer statistics. Potentially, when in further studies an array of HRs can be analysed properly, larger effects on the mean boundary layer statistics can be measured.

The instantaneous effects of the HR resonance on the TBL flow are evident. From the LCS, energy spectra and the phase-averaged results it can be seen that a clear phase-interlocking of the TBL flow is present in the cases where a pressure-velocity coupling is achieved. Clear bands of inflow and outflow can be seen, with a streamwise width that appears to be related to the streamwise extent of half a period of HR resonance. These inflow and outflow cycles cause an increase and decrease in streamwise velocity, respectively. These effects are clearest up to  $y^+ = 25$ , beyond which the effects are still present to a much smaller extent. The streamwise extent of the effects has shown to be a maximum of one cycle of resonance from the PIV measurements – corresponding to approximately 7 mm ( $\approx 250l^*$ ) – for the case with the strongest pressure-velocity coupling. A reduction in coherence then seems to correspond to a reduced streamwise extent of the effects.

### 9.4. Effect on Near Wall-Cycle Events

In the micro-cavity array study from Silvestri et al. (2017a), a clear reduction in sweep intensity and duration was measured found using the VITA analysis. In the present study, neither of these effects were found for the single HR setup. For all HRs tested, the only significant differences were before and after the VITA events, and these effects were attributed to the orifice in isolation.

However, from the quadrant analysis, an increase in the relative strength of both Q2 and Q4 events was identified. This typically indicates an increased contribution to the production of turbulence from an increased strength of sweep and ejection events.

Combining the observations from the VITA analysis and quadrant analysis, it appears that the sweep and ejection events are not fundamentally changed. The cyclic inflow and outflow cause an apparent increase in relative  $v$ -fluctuations without fundamentally changing the  $u$ -fluctuations. This still causes an increase in the production of turbulence.

As stated before, a direct comparison of the results from the current study on a single HR to the full micro-cavity array from Silvestri et al. (2017a) is not possible. There is a possibility that with a full array of HRs a more distinct change in the near-wall cycle events can be observed.

### 9.5. Potential Uses for Helmholtz-Resonators as Flow Control Method

None of the present results currently appears to indicate that the HRs as tested can be a suitable method of TBL flow control for reducing skin friction. However, there can be other uses for the HRs as a flow control method. The HRs have shown to lead to an increase in turbulence production from the

inflow and outflow cycles, without significant alterations could to the mean boundary layer profile.

This could make the HRs potentially an efficient method for separation control that does not induce a large increase in skin friction. This could make it an attractive alternative to typical methods of separation control – such as vortex generators — with the downside of a relatively large increase in skin friction from an increase in surface area. It should be noted that the presence of the orifices of the HRs is likely to induce a small increase in pressure drag that might lead to a non-negligible drag increase when a full array of HRs is applied.

The various HR geometries tested have shown that the HR resonance frequency and magnitude of resonance can be finely tuned. Therefore, the HRs can be adjusted in such a manner that the increase in turbulence is just enough for getting the desired improvement in separation control. Furthermore, a system is envisioned in which the cavity length is modified based on flight conditions. This could allow the HRs to work optimally across conditions rather than being optimal for just one.

### **9.6. Remarks on Research Questions**

Eventually, this study has focused on the effect of a single HR on the grazing TBL flow. While it was intended to test both the single HR setup and an HR array setup, the HR array measurements were discarded due to doubts over their validity. This was elaborated upon in §7.2.4. This means not all research questions as stated in Chapter 1 could be answered fully. The tuning of a system of HRs under a grazing TBL and the subsequent effect on the TBL flow remains subject to further research. Furthermore, due to the testing of a single HR, no large effects on the mean flow properties were observed. As mentioned before, it is considered that a full array of HRs might show a more pronounced global effect on the mean statistics of the TBL flow.

The current experimental campaign has given valuable insight into the other research questions. This contributes to the understanding of the working of HRS under a grazing TBL. It has been shown that both spatial and temporal tuning can significantly change the interaction between the HR and the TBL flow. Furthermore, the shown differences between acoustic excitation and TBL excitation of HRs are useful in the design of future experiments. The found domain-of-influence of the HRs on the TBL flow gives a good starting point for the future design of arrays of HRs

## Conclusions

Finding passive means of skin friction reduction has been an active topic of research within the aerospace industry. A reduction in skin friction will directly result in reduced fuel burn and operating costs. On airliners, the boundary layer is primarily turbulent due to the high Reynolds numbers during flight and the presence of surface irregularities such as cockpit windows and doors. Therefore, the focus of past research has been to attenuate the effect of the structures and events linked to the production of turbulence within a turbulent boundary layer.

Existing passive means of skin friction reduction can be divided into two categories: (1) those that focus on the large-scale outer layer flow and (2) those that focus on the small-scale near-wall cycle within the TBL. Large-scale boundary layer control has been achieved by e.g. breaking up the coherent structures that amplify the near-wall cycle. Small-scale boundary layer control has been attempted by suppressing the low-speed streaks which have been linked to the region of maximum turbulence production through the process of sweep, bursting and ejection.

Recent studies involving micro-cavity arrays have indicated a potential for attenuating sweep events. Through energy dissipation within the cavities, the wall-normal pressure fluctuations were damped, which reduces the turbulence intensity in the buffer and log-regions of the boundary layer. With a diameter of 60 viscous units, the most efficient attenuation of sweep events was achieved. It was hypothesised that with surface-embedded Helmholtz-Resonators this effect can be amplified. HRs are widely used within the aerospace industry as means of noise attenuation when the resonance frequency is tuned to the blade-passing frequency of a fan in a turbo-fan engine.

Research has shown that HRs can be excited by and tuned to a grazing TBL. Two mechanisms of excitation are distinguished: 1) through shear layer separation over the orifice and 2) through the wall-pressure fluctuations. Three strategies for the combined spatial and temporal tuning of HRs are proposed. The first strategy consists of spatial and temporal tuning towards the streamwise wavelength of the most energetic streamwise velocity fluctuations. The second and third strategies include spatial tuning towards the most efficient attenuation of sweep events, with an expected orifice diameter of 60 viscous units. The temporal tuning differs and is based on the streamwise wavelength of either 1) the most energetic streamwise velocity fluctuations or 2) the most energetic wall-normal velocity fluctuations and the wall-pressure fluctuations, with the latter two coinciding at the same streamwise wavelength. The proposed strategies can be considered realisable on an aircraft fuselage in cruise conditions, with dimensions in the order of a millimetre.

In the presented experimental campaign, one of the proposed design strategies has been tested, with the spatial tuning to the most efficient attenuation of sweep events and the temporal tuning towards the most energetic wall-normal velocity fluctuations. Three design frequencies were tested: one matching the frequency of the most energetic wall-normal velocity fluctuations, as well as a lower frequency (subresonance) and a higher frequency (superresonance). With subresonance, it was intended to induce a phase switch with the HR with respect to the frequency of the most energetic wall-normal velocity fluctuations. With superresonance, no such phase switch is induced. Various orifice diameters were tested as part of a parameter study.

First, the difference between pure acoustic excitation of HRs and excitation of HRs under a fully developed grazing TBL flow at  $Re_\tau \approx 2200$  was analysed through microphone measurements. It was found

that when the HRs were excited by the grazing TBL, the effective end correction is reduced, increasing the HR resonance frequency. The overtones of the HRs were found to occur at the same frequency for both pure acoustic and TBL excitation of HRs. With TBL excitation, it was found that the several excitation methods – shear layer interaction and incident pressure fluctuations – simultaneously occur. This increases the maximum gain with TBL excitation as compared to pure acoustic excitation for the same HR geometry.

Through hot-wire measurements, it was found that with nominal resonance and subresonance, a strong pressure-velocity coupling can be established that extends up to  $y^+ = 25$ . In this region, a clear phase interlocking of the TBL flow and the HR resonance was observed. Bands of inflow and outflow can be identified with a streamwise width directly coupled to the HR resonance frequency. This cycle of inflow and outflow causes a periodic increase and decrease in the streamwise velocity, respectively. These effects on the streamwise velocity are clearly visible in the energy spectra as an increase in spectral energy around the wavelength of the HR resonance frequency. The streamwise extent of the effects was found to be at most one full cycle of resonance, approximately 250 viscous units downstream of the resonator.

To date, no clear effects of the HR resonance on the mean statistics of the TBL were identified. The only effects visible in the mean statistics were attributed to the orifice in isolation. The effects of the HR resonance are primarily observed as cyclic instantaneous effects coupled to the HR resonance frequency. While quadrant analysis indicates an increase in turbulence production from an increased relative strength of Q2 and Q4 events, variable-interval time averaging indicates no significant changes in the intensity and duration of the near-wall cycle turbulence events as a result of the HR resonance. However, it should be noted that, eventually, the study has focused on the effects of a single HR on the TBL flow. Future studies with arrays of HRs could potentially show a more pronounced global effect on the mean statistics of the TBL flow.

Furthermore, to date, no drag-reduction potential could be identified from the HRs as tested. While the spatial resolution of the measurements was not enough for a direct measure of the wall-normal velocity gradient, the other applied data analysis methods show no clear indications of reduced skin friction. However, the increased turbulence production in the absence of a large skin friction increase could potentially make the HRs an efficient flow control method for separation control.

# Recommendations for Future Research

This chapter presents recommendations for further research towards Helmholtz-Resonators under a grazing Turbulent Boundary Layer. First, §11.1 and §11.2 present recommendations for the geometry and design of the tested HRs. Subsequently, §11.3 and §11.4 present improvements regarding the noise and flow measurements respectively. Finally, §11.5 presents recommendations regarding the adopted design strategy for the tested HRs.

## 11.1. More Isolated Parameter Study

With the aim to test a wide variety of HR geometries in a modular setup, some parameters were fixed for all HRs – for instance the neck length and cavity diameter. Therefore, a change in one parameter could typically not be tested in isolation. While this did not affect the validity of the used equations for the HR resonance, it is often difficult to isolate the effect of the change of a single parameter. Therefore, a more isolated parameter study is recommended. With the results of the current study, the following considerations are proposed:

1. *Constant ratio of neck length to orifice diameter.* There are indications that an increase in the ratio of neck length to orifice diameter increases the friction losses in the neck and thus increases the damping of the resonator system. Therefore, in the current study, the different orifice diameters tested all had different levels of resonance. Some of the flow measurement results have been influenced by this.
2. *Constant ratio of cavity length to cavity diameter.* To change the resonance frequency for a given orifice diameter, only the cavity length was altered. Therefore, for each resonance frequency, the ratio of cavity length to cavity diameter had to be altered. To achieve a lower resonance frequency, the cavity length was increased, increasing the ratio of cavity length to cavity diameter. There are signs that this has contributed to an increased magnitude of resonance.

Furthermore, further research towards the relation between the orifice diameter and half a wavelength of HR resonance is recommended. With the spatial and temporal tuning of HRs completely decoupled, this relation has not yet been considered. From the present study, it is not yet evident how this could have affected the results. Future studies quantifying this effect will likely further improve the understanding of HRs under a grazing TBL.

## 11.2. Helmholtz-Resonator Array Design

In the current study, none of the HR array measurements has been presented due to doubts about the validity of the setup. In the aim to make a very modular setup, in which the cavity length was controlled by stacking individual plates, the working of the HRs seems to have been negatively affected. This was caused by small surface irregularities in the cavity over the connection of the stack plates and the potential for intercommunication between the HRs.

Therefore, it is recommended to make the cavities for the HRs in an array out of one piece. This can either be for each HR separately or for instance milling all cavities for the full array out of one piece of material. This will prevent irregularities in the cavity surface and reduce the potential for intercommunication between the individual HRs. The top plates containing the HR cavities can still be made out of a separate piece of material. This method was applied in the single HR setup without any clear signs of concern.

Inevitably, this recommendation reduces the flexibility of testing multiple HR arrays with the same setup. Therefore, it is recommended to only start testing a full array of HRs after completing the further parameter study on a single HR.

### **11.3. Improvements for Noise Measurements**

In the current setup, the noise microphone was located at approximately the same streamwise location as the tested HRs. For the strongest resonance cases of the tested HRs, there were small signs that the HR resonance was actually picked up by the noise microphone. This then affected the results through the noise-correction procedure. As all sound that is picked up by the noise microphone is considered to be from external noise sources, it might have over-corrected at the HR resonance frequency for these HRs.

As the main noise source of the setup is from the wind tunnel itself, it is proposed to place the noise microphone further upstream. This will reduce the chances of the noise microphone picking up any HR resonance. It will change the measured sound level of the wind tunnel noise. However, this does not play a role in the linear stochastic estimation used for the noise correction. Therefore, the noise-correction procedure can still be applied.

With the further upstream placement of the noise microphone, the capability of the noise microphone to measure noise from sources behind the test section will be reduced. Therefore, care should be taken that all noise sources behind the test section should be eliminated as much as possible.

### **11.4. Improvements for Flow Measurements**

While the current flow measurements give clear indications for the pressure-velocity coupling of HRs and the TBL flow and the subsequent effects on the grazing TBL flow, improvements have been identified that could increase the confidence in the results.

The current measurements have given indications for the streamwise extent and wall-normal extent of the effects of the HR on the TBL. Therefore, it is recommended for further PIV images to have a much more zoomed-in field of view that focuses specifically on this area of effect. This will significantly increase the spatial resolution of the PIV measurements. With increased spatial resolution, also the accuracy of the wall-finder algorithm can be improved. This then could potentially allow for a direct measurement of the wall-normal velocity gradient – to identify any changes in skin friction.

For the hot-wire measurements, the accuracy of the wall positioning was approximately 2.5 viscous units. Even though is a very small error, it can already have significant effects on the results. In the current study, this has been corrected for using a DNS mean-profile fitting procedure. While seemingly giving accurate results, it cannot be ruled out that this affected the results. Therefore, improved confidence in the wall-positioning will improve the accuracy of the results. The telescope used for the wall-positioning was equipped with a camera. It is recommended to record an image of the hot-wire probe relative to the wall before every hot-wire profile. Then, these images can be used in post-processing to accurately determine the wall position.

Furthermore, flow measurements are recommended from which energy spectra can be calculated for both the streamwise and wall-normal velocity fluctuations. With the present study, only the energy spectra of the streamwise velocity fluctuations could be calculated. The PIV measurements are not time-resolved enough to obtain complete energy spectra. In future studies, if the measurement equipment is available, cross hot wire measurements or high-speed PIV measurements would be suitable to calculate complete energy spectra.

### **11.5. Further Research towards Other Design Strategies**

The current study has focused on a sole design strategy, which was chosen as it was envisioned to lead to the largest reduction in skin friction. However, with the results indicating that the flow control might be more useful for separation control rather than reducing skin friction, it might be a useful exercise to research the other design strategies.

Both alternatives have a temporal tuning based on the most energetic wavelength of streamwise velocity fluctuations, with varying spatial tuning. These design strategies would rely more on the shear layer resonance for the excitation of the HRs. Past research has shown potential for larger-scale HRs to be beneficial for both separation control and achieving a small reduction in skin friction. However, these studies did not yet have the temporal scaling of HRs to specific structures and events within the TBL.

Therefore, it is recommended to include both alternative design strategies in any further research. Based on the results of the present study, it is recommended that future research focuses on separation control as the primary function of the flow control method.

# Bibliography

- Azimi, M., Ommi, F. and Alashti, N. J. (2014), 'Using acoustic liner for fan noise reduction in modern turbofan engines', *International Journal of Aeronautical and Space Sciences* **15**(1), 97–101.
- Baars, W. J. (2021), 'Private communication'.
- Baars, W. J., Hutchins, N. and Marusic, I. (2016), 'Spectral stochastic estimation of high-Reynolds-number wall-bounded turbulence for a refined inner-outer interaction model', *Physical Review Fluids* **1**(5), 1–23.
- Baars, W. J. and Marusic, I. (2020), 'Data-driven decomposition of the streamwise turbulence kinetic energy in boundary layers. Part 1. Energy spectra', *Journal of Fluid Mechanics* **882**, A251–A2540.
- Bandyopadhyay, P. R., Henoach, C., Hrubec, J. D., Semenov, B. N., Amirov, A. I., Kulik, V. M., Malyuga, A. G., Choi, K. S. and Escudier, M. P. (2005), 'Experiments on the effects of aging on compliant coating drag reduction', *Physics of Fluids* **17**(8), 085104.
- Bhat, S. S., Silvestri, A., Cazzolato, B. S. and Arjomandi, M. (2021), 'Mechanism of control of the near-wall turbulence using a micro-cavity array', *Physics of Fluids* **33**(7), 075114.
- Blackwelder, R. F. and Kaplan, R. E. (1976), 'On the wall structure of the turbulent boundary layer', *Journal of Fluid Mechanics* **76**(1), 89–112.
- Bushnell, D. M. (2003), 'Aircraft drag reduction—a review', *Proceedings of the Institution of Mechanical Engineers, Part G: Journal of Aerospace Engineering* **217**(1), 1–18.
- Carpenter, P. W., Davies, C. and Lucey, A. D. (2000), 'Hydrodynamics and compliant walls: Does the dolphin have a secret?', *Current Science* **79**(6), 758–765.
- Chan, I. C., Örlü, R., Schlatter, P. and Chin, R. C. (2021), 'The skin-friction coefficient of a turbulent boundary layer modified by a large-eddy break-up device', *Physics of Fluids* **33**(3).
- Chanaud, R. C. (1994), 'Effects of geometry on the resonance frequency of Helmholtz Resonators', *Journal of Sound and Vibration* **178**(3), 337–348.
- Chang, K., Constantinescu, G. and Park, S. O. (2006), 'Analysis of the flow and mass transfer processes for the incompressible flow past an open cavity with a laminar and a fully turbulent incoming boundary layer', *Journal of Fluid Mechanics* **561**, 113–145.
- Chauhan, K. A., Monkewitz, P. A. and Nagib, H. M. (2009), 'Criteria for assessing experiments in zero pressure gradient boundary layers', *Fluid Dynamics Research* **41**(2), 021404.
- Choi, K. and Fujisawa, N. (1993), *Possibility of drag reduction using d-type roughness*, Springer, Dordrecht.
- Corino, E. R. and Brodkey, R. S. (1969), 'A visual investigation of the wall region in turbulent flow', *Journal of Fluid Mechanics* **37**(1), 1–30.
- Corke, T. C. and Thomas, F. O. (2018), 'Active and passive turbulent boundary-layer drag reduction', *AIAA Journal* **56**(10), 3835–3847.
- Dacome, G. and Baars, W. J. (2021), 'Private communication'.
- de Koning, C. (2021), Application of acoustic metamaterials in boundary layer instability control, PhD thesis, TU Delft.

- Drózdź, A. and Elsner, W. (2017), 'Amplitude modulation and its relation to streamwise convection velocity', *International Journal of Heat and Fluid Flow* **63**, 67–74.
- Elder, S. A. (1978), 'Self-excited depth-mode resonance for a wall-mounted cavity in turbulent flow', *The Journal of the Acoustical Society of America* **64**(3), 877.
- Flynn, K. P., Panton, R. L. and Bogard, D. G. (1989), The effect of a row of Helmholtz resonators on the turbulence of a boundary layer, in '2nd Shear Flow Conference', American Institute of Aeronautics and Astronautics, Reston, Virginia.
- Flynn, K. P., Panton, R. L. and Bogard, D. G. (1990), 'Effect of Helmholtz resonators on boundary-layer turbulence', *AIAA Journal* **28**(11), 1857–1858.
- Fukagata, K., Kern, S., Chatelain, P., Koumoutsakos, P. and Kasagi, N. (2008), 'Evolutionary optimization of an anisotropic compliant surface for turbulent friction drag reduction', *Journal of Turbulence* **9**(35), N35.
- Gad-el-Hak, M. (2000), *Flow control: passive, active, and reactive flow management*, Cambridge University Press.
- Garcia-Mayoral, R. and Jimenez, J. (2011), 'Drag reduction by riblets', *Philosophical Transactions of the Royal Society A: Mathematical, Physical and Engineering Sciences* **369**(1940), 1412–1427.
- Ghanadi, F. (2014), Application of a Helmholtz resonator excited by grazing flow for manipulation of a turbulent boundary layer., PhD thesis, University of Adelaide.
- Ghanadi, F., Arjomandi, M., Cazzolato, B. S. and Zander, A. C. (2015), 'Analysis of the turbulent boundary layer in the vicinity of a self-excited cylindrical Helmholtz resonator', *Journal of Turbulence* **16**(8), 705–728.
- Ghanadi, F., Arjomandi, M., Cazzolato, B. and Zander, A. (2014a), 'Interaction of a flow-excited Helmholtz resonator with a grazing turbulent boundary layer', *Experimental Thermal and Fluid Science* **58**, 80–92.
- Ghanadi, F., Arjomandi, M., Cazzolato, B. and Zander, A. (2014b), 'Understanding of the flow behaviour on a Helmholtz resonator excited by grazing flow', *International Journal of Computational Fluid Dynamics* **28**(5), 219–231.
- Gibeau, B. and Ghaemi, S. (2021), 'Low- And mid-frequency wall-pressure sources in a turbulent boundary layer', *Journal of Fluid Mechanics* **918**, 1–45.
- Hahn, S., Je, J. and Choi, H. (2002), 'Direct numerical simulation of turbulent channel flow with permeable walls', *Journal of Fluid Mechanics* **450**, 259–285.
- Helmholtz, H. (1860), 'Theorie der Luftschwingungen in Röhren mit offenen Enden.', *Journal für die reine und angewandte Mathematik (Crelles Journal)* pp. 1–72.
- Hinze, J. (1975), *Turbulence*, McGraw-Hill classic textbook reissue series, McGraw-Hill.
- Hutchins, N. and Marusic, I. (2007a), 'Evidence of very long meandering features in the logarithmic region of turbulent boundary layers', *Journal of Fluid Mechanics* **579**, 1–28.
- Hutchins, N. and Marusic, I. (2007b), 'Evidence of very long meandering features in the logarithmic region of turbulent boundary layers', *Journal of Fluid Mechanics* **579**, 1–28.
- Ingard, U. (1953), 'On the theory and design of acoustic resonators', *Journal of the Acoustical Society of America* **25**(6), 1037–1061.
- Jiménez, J. (2018), 'Coherent structures in wall-bounded turbulence', *Journal of Fluid Mechanics* **842**, P1.
- Kinsler, L., Frey, A., Coppens, A. and Sanders, J. (2000), *Fundamentals of acoustics*, Wiley.

- Klewicki, J. C. (2010), 'Reynolds number dependence, scaling, and dynamics of turbulent boundary layers', *Journal of Fluids Engineering* **132**(9).
- Kline, S. J., Reynolds, W. C., Schraub, F. A. and Runstadler, P. W. (1967), 'The structure of turbulent boundary layers', *Journal of Fluid Mechanics* **30**(4), 741–773.
- Kline, S. J. and Robinson, S. K. (1990), Turbulent boundary layer structure: progress, status, and challenges, in 'Structure of Turbulence and Drag Reduction', Springer Berlin Heidelberg, Berlin, Heidelberg, pp. 3–22.
- Lee, M. and Moser, R. D. (2015), 'Direct numerical simulation of turbulent channel flow up to  $Re_\tau \approx 5200$ ', *Journal of Fluid Mechanics* **774**, 395–415.
- Liu, C. and Gayme, D. F. (2020), 'An input-output based analysis of convective velocity in turbulent channels', *Journal of Fluid Mechanics* **888**, A321–A3232.
- Ma, R., Slaboch, P. E. and Morris, S. C. (2009), 'Fluid mechanics of the flow-excited Helmholtz resonator', *Journal of Fluid Mechanics* **623**, 1–26.
- Maa, D.-Y. (1998), 'Potential of microperforated panel absorber', *The Journal of the Acoustical Society of America* **104**(5), 2861.
- Marec, J.-P. (2001), 'Drag reduction: a major task for research', *Aerodynamic Drag Reduction Technologies* pp. 17–27.
- Martell, M. B., Perot, J. B. and Rothstein, J. P. (2009), 'Direct numerical simulations of turbulent flows over superhydrophobic surfaces', *Journal of Fluid Mechanics* **620**, 31–41.
- Mathis, R., Hutchins, N. and Marusic, I. (2009), 'Large-scale amplitude modulation of the small-scale structures in turbulent boundary layers', *Journal of Fluid Mechanics* **628**, 311–337.
- McLean, J. D., George-Falvy, D. and Sullivan, P. P. (1987), 'Flight-test of turbulent skin-friction reduction by riblets', *Turbulent drag reduction by passive means* pp. 408–424.
- Modesti, D., Endrikat, S., Hutchins, N. and Chung, D. (2021), 'Dispersive stresses in turbulent flow over riblets', *Journal of Fluid Mechanics* **917**.
- Panton, R., Flynn, K. and Bogard, D. (1987), Control of turbulence through a row of Helmholtz resonators, in '25th AIAA Aerospace Sciences Meeting', American Institute of Aeronautics and Astronautics, Reston, Virginia.
- Panton, R. L., Lee, M. and Moser, R. D. (2017), 'Correlation of pressure fluctuations in turbulent wall layers', *Physical Review Fluids* **2**(9), 1–12.
- Panton, R. L. and Miller, J. M. (1975a), 'Excitation of a Helmholtz resonator by a turbulent boundary layer', *The Journal of the Acoustical Society of America* **58**(4), 800–806.
- Panton, R. L. and Miller, J. M. (1975b), 'Resonant frequencies of cylindrical Helmholtz resonators', *The Journal of the Acoustical Society of America* **57**(6), 1533–1535.
- Perlin, M., Dowling, D. R. and Ceccio, S. L. (2016), 'Freeman scholar review: passive and active skin-friction drag reduction in turbulent boundary layers', *Journal of Fluids Engineering* **138**(9).
- Pope, S. B. (2000), *Turbulent flows*, Cambridge University Press.
- Rayleigh, J. (1896), *The theory of sound*, number v. 2 in 'The Theory of Sound', Macmillan.
- Robinson, S. K. (1991), 'Coherent motions in the turbulent boundary layer', *Annual Review of Fluid Mechanics* **23**(1), 601–639.
- Schlichting, H. and Gersten, K. (2017), *Boundary-layer theory*, Vol. 20, 9th edn, Springer Berlin Heidelberg, Berlin, Heidelberg.

- Selamet, A., Radavich, P. M., Dickey, N. S. and Novak, J. M. (1997), 'Circular concentric Helmholtz resonators', *The Journal of the Acoustical Society of America* **101**(1), 41–51.
- Severino, G. F., Silvestri, A., Cazzolato, B. S. and Arjomandi, M. (2022), 'Sensitivity analysis of orifice length of micro-cavity array for the purpose of turbulence attenuation', *Experiments in Fluids* **63**(1), 1–10.
- Seyyedi, S. M., Dogonchi, A. S., Hashemi-Tilehnoee, M. and Ganji, D. D. (2019), 'Improved velocity and temperature profiles for integral solution in the laminar boundary layer flow on a semi-infinite flat plate', *Heat Transfer—Asian Research* **48**(1), 182–215.
- Silvestri, A., Ghanadi, F., Arjomandi, M., Cazzolato, B. and Zander, A. (2017a), 'Attenuation of sweep events in a turbulent boundary layer using micro-cavities', *Experiments in Fluids* **58**(5), 1–13.
- Silvestri, A., Ghanadi, F., Arjomandi, M., Cazzolato, B., Zander, A. and Chin, R. (2018), 'Mechanism of sweep event attenuation using micro-cavities in a turbulent boundary layer', *Physics of Fluids* **30**(5), 055108.
- Silvestri, A., Ghanadi, F., Arjomandi, M., Chin, R., Cazzolato, B. and Zander, A. (2017b), 'Attenuation of turbulence by the passive control of sweep events in a turbulent boundary layer using micro-cavities', *Physics of Fluids* **29**(11), 115102.
- Skudrzyk, E. (1954), *Die Grundlagen der Akustik*, Springer Vienna.
- Smith, C. R. and Metzler, S. P. (1983), 'The characteristics of low-speed streaks in the near-wall region of a turbulent boundary layer', *Journal of Fluid Mechanics* **129**, 27–54.
- Smith, C. R., Walker, J. D. A. and Haidari, A. H. (1991), 'On the dynamics of near-wall turbulence', *Philosophical Transactions of the Royal Society of London. Series A: Physical and Engineering Sciences* **336**(1641), 131–175.
- Spalart, P. R. (1988), 'Direct simulation of a turbulent boundary layer up to  $R\theta = 1410$ ', *Journal of Fluid Mechanics* **187**, 61–98.
- Stein, L. (2018), Simulation and modeling of a Helmholtz resonator under grazing turbulent flow, PhD thesis, TU Berlin.
- Tsuji, Y., Fransson, J. H., Alfredsson, P. H. and Johansson, A. V. (2007), 'Pressure statistics and their scaling in high-Reynolds-number turbulent boundary layers', *Journal of Fluid Mechanics* **585**, 1–40.
- Urzyńcok, F. (2003), Separation control by flow-induced oscillations of a resonator, PhD thesis, TU Berlin.
- Wallace, J. M. (2016), 'Quadrant analysis in turbulence research: history and evolution', *Annual Review of Fluid Mechanics* **48**(1), 131–158.
- Walsh, M. J. (1983), 'Riblets as a viscous drag reduction technique', *AIAA Journal* **21**(4), 485–486.
- White, F. (2006), *Viscous fluid flow*, McGraw-Hill international edition, McGraw-Hill.



# Assembly Overview

In Figure A.1 and Figure A.2, an overview of the assemblies for both the single HR setup and the HR array setup are presented respectively. The overviews are to scale, but do not indicate threads and other mechanical components such as bolts and nuts.

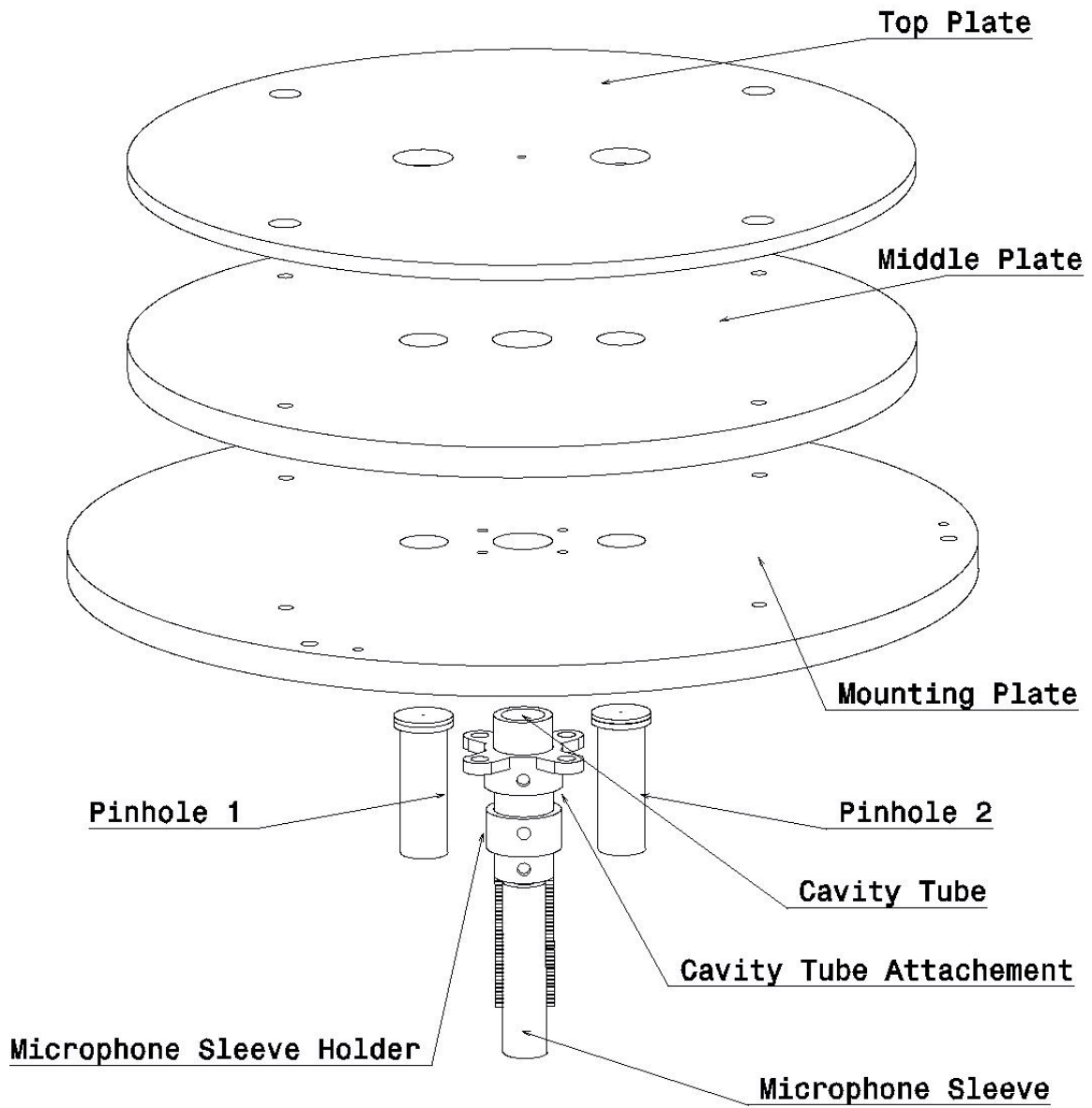


**Figure A.1:** Schematic overview of the single HR setup assembly

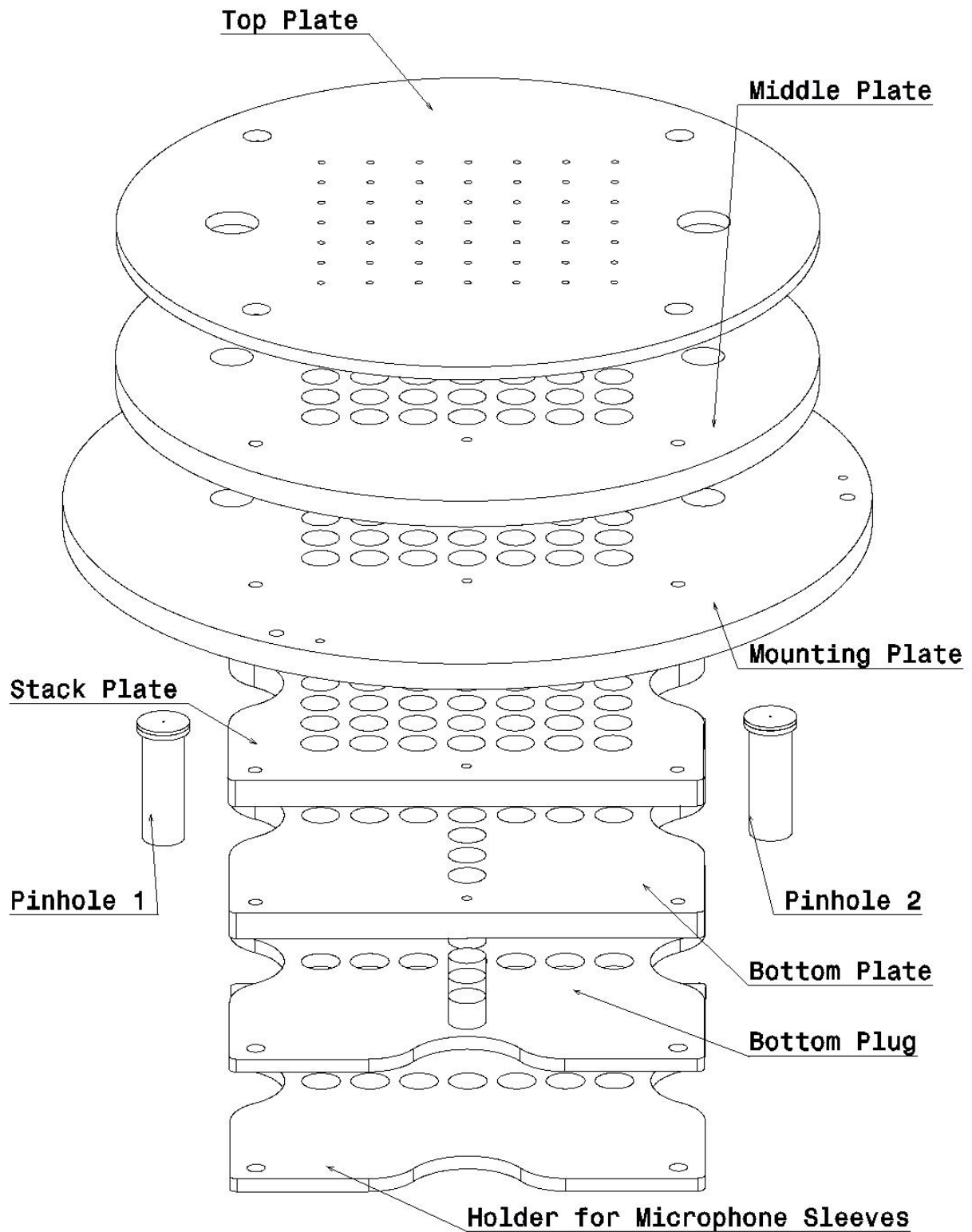


**Figure A.2:** Schematic overview of the HR array setup assembly